



## Recent advancements in the use of novel piezoelectric materials for piezocatalytic and piezo-photocatalytic applications

Hongjuan Zheng<sup>a</sup>, Yulong Wang<sup>b</sup>, Jinsong Liu<sup>c</sup>, Jing wang<sup>a</sup>, Kang Yan<sup>a</sup>, Kongjun Zhu<sup>a,\*</sup>

<sup>a</sup> State Key Laboratory of Mechanics and Control for Aerospace Structures, Nanjing University of Aeronautics and Astronautics, Nanjing 210016, China

<sup>b</sup> Department of Applied Physics, The Hong Kong Polytechnic University, Hong Kong, China

<sup>c</sup> College of Materials Science and Technology, Nanjing University of Aeronautics and Astronautics, Nanjing 210016, China



### ARTICLE INFO

#### Keywords:

Piezocatalysis  
Piezo-photocatalysis  
Transition metal dichalcogenide  
Bismuth layer  
Metal-organic framework

### ABSTRACT

Piezocatalysis has gradually attracted the interest of researchers owing to their excellent ability to improve the separation and migration of photoelectrons and holes. The alternating built-in electric field generated by the piezoelectric effect of traditional piezoelectric materials, such as BaTiO<sub>3</sub>, ZnO, provides a strong driving force for the separation and migration of carriers. In addition to traditional piezoelectric materials, certain unique materials, such as layered transition metal dichalcogenides, bismuth-layered structure materials, wurtzite-based semiconductors, graphene, g-C<sub>3</sub>N<sub>4</sub>, and metal-organic frameworks, have piezoelectric properties and are considered novel piezocatalysts. This review summarizes the recent advancements in the use of these novel piezoelectric materials for piezocatalytic and piezo-photocatalytic applications. Their discovery, the verification of piezoelectric features, the current research status, challenges, and perspectives for developing novel piezocatalysts are summarized. This review is expected to provide comprehensive guidance for the in-depth understanding and development of more novel piezocatalysts in emerging energy and environmental applications.

### 1. Introduction

Currently, the huge consumption of fossil fuels and worsening environmental pollution are two of the most serious issues encountered by researchers, prompting the development, harvesting, and utilization of various alternative clean energy resources, such as solar energy and mechanical energy. Harvesting and converting energy from the environment, such as solar light, waste heat, and mechanical vibrations, to replace fossil fuels or address environmental pollution has also aroused the interest of scholars. Since the study of TiO<sub>2</sub> photoelectrodes by Fujishima and Honda in 1972 [1], solar energy-driven photocatalysis, in which an oxide semiconductor with a suitable bandgap (E<sub>g</sub>) can efficiently absorb light and form photogenerated electron (e<sup>-</sup>)-hole (h<sup>+</sup>) pairs for water splitting, carbon dioxide reduction and wastewater treatment, has been widely investigated and attained considerable achievement [2,3]. However, the practical application of these materials in photocatalysis is currently limited due to their low quantum efficiency, complicated catalyst design, and lackluster response in the absence of solar irradiation. An important issue is the rapid recombination of photo-induced e<sup>-</sup> and h<sup>+</sup> (picoseconds or nanoseconds) in the bulk phase and on the surface of photocatalysts, which results in low

photocatalytic efficiency [4]. Accelerating the separation and transfer kinetics of photogenerated carriers appears to be a key focus of future research. Although many strategies, including E<sub>g</sub> tuning, heterojunction construction, metal or nonmetal ion doping, surface defect engineering, and nanostructured morphology maneuvering, can promote charge migration on the surfaces of photocatalysts, an efficient charge separation process in the bulk charge of photocatalysts still needs to be explored.

As a newly emerging research field, piezocatalysis (i.e., the technology of directly converting mechanical energy into chemical energy via the piezoelectric effect of piezoelectric materials to split water or degrade organic pollutants) has attracted wide research interest in the last decade [5]. The piezoelectric effect, which was first discovered in 1880 by Jacques and Pierre Curie, involves the deformation of a piezoelectric material by using an applied force along its asymmetric direction, thereafter generating positive and negative charges on two opposite surfaces and vice versa. Piezoelectrics are a class of materials that create an electric field in response to mechanical deformation. The lack of centrosymmetry in crystals gives rise to piezoelectricity, which can be classified phenomenologically into three subcategories of materials: ferroelectrics, pyroelectrics, and piezoelectrics. Then, the polarity

\* Corresponding author.

E-mail address: [kjzhu@nuaa.edu.cn](mailto:kjzhu@nuaa.edu.cn) (K. Zhu).

of the charge changes with the varying direction of the applied force. However, the latter property includes the former properties but not vice versa: all ferroelectric materials are piezoelectrics, but piezoelectric materials are not necessarily ferroelectrics [6]. Ferroelectrics are characterized by spontaneous polarization ( $P_s$ ), which can be inverted using an external electric field ( $E$ ) (Fig. 1a). The existence of  $P_s$  results in the formation of positive- and negative-bound polarization charges at the corresponding polarized surfaces, and the space charges become attracted to both crystal surfaces, subsequently screening the polarized bound charge. Pyroelectrics exhibit a change in internal polarization in response to variations in temperature. Polarization only exists at temperatures lower than the Curie temperature ( $T_c$ ). Within this range, the internal polarization changes when the pyroelectric materials undergo a temperature change. Piezoelectrics rely on the centers of positive cations and negative anions shifting reversely when external strain is applied, leading to dipole polarization. Meanwhile, piezoelectric materials lacking  $P_s$  usually need external stimuli (e.g., mechanical stress and temperature changes) to induce a change in polarization, thereafter generating an induced electric field together with the production of screening electric charges of equal magnitude with contrasting symbols on the surface.

### 1.1. Traditional piezoelectric materials

Traditional piezoelectric materials include  $\text{ABO}_3$ -type perovskites (A: rare-earth or alkaline-earth metal; B: transition metal), including barium titanate-based ( $\text{BaTiO}_3$ ) and lead zirconate titanate-based materials ( $\text{Pb}(\text{Zr}_{1-x}\text{Ti}_x)\text{O}_3$ ). Other examples include alkali metal niobate-based materials, such as potassium niobate ( $\text{KNbO}_3$ ), sodium potassium niobate ( $(\text{Na}_{1-x}\text{K}_x)\text{NbO}_3$ ), silver niobate ( $\text{AgNbO}_3$ ), bismuth ferrite-based ( $\text{BiFeO}_3$ ), nonperovskite-like wurtzite consisting of  $\text{ZnO}$  and  $\text{GaN}$ , piezoelectric polymers polyvinylidene fluoride (PVDF), and

PVDF-trifluoroethylene (TrFE).  $\text{BaTiO}_3$  is a classic example of the ferroelectric  $\text{ABO}_3$  perovskite family with a  $T_c$  of  $120^\circ\text{C}$ . In the  $\text{BaTiO}_3$  crystal structure, one Ti atom coordinates with six O atoms to form octahedral clusters ( $\text{TiO}_6$ ) [7], in which  $\text{Ba}^{2+}$  is located at the corners of the unit cell. The appearance of spontaneous polarization ( $P_s$ ) in  $\text{BaTiO}_3$  is related to a shift of the  $\text{Ti}^{4+}$  and  $\text{O}^{2-}$  ions. The  $\text{BaTiO}_3$  of the cubic phase (symmetry group:  $Pm3m$ ) entails central symmetry but lacks piezoelectricity because the  $\text{Ti}^{4+}$  ion is located at the center of  $\text{TiO}_6$ . The  $\text{Ti}^{4+}$  ion in tetragonal structures (symmetry group:  $P4mm$ ) moves away from the center of the unit cell, thus giving a net dipole moment to this unit cell and presenting a macroscopic  $P_s$  along the [001] direction (Fig. 1b) [8]. Wurtzite belongs to a hexagonal crystal system (space group:  $P6_3mc$ ) with a tetrahedral coordination AB-type composition.  $\text{ZnO}$  is a typical wurtzite-structure piezoelectric material. In the  $\text{ZnO}$  crystal structure,  $\text{Zn}^{2+}$  and  $\text{O}^{2-}$  are stacked layer by layer along the c-axis, and their centers overlap with each other, hence the nondetection of polarization in normal crystals. When an external force is applied, the positive and negative charge centers separate in reverse, leading to dipole polarization with a piezoelectric potential (Fig. 1c). Furthermore, certain flexible polymers exhibit piezoelectricity because of their asymmetrical molecular structure and orientation. PVDF, which is one of the most common piezoelectric polymers, consists of [-CH<sub>2</sub>-CF<sub>2</sub>-] monomers and exists in three dominant polymorph phases ( $\alpha$ ,  $\beta$ , and  $\gamma$ ) [9]. The piezoelectric property of PVDF can be attributed to the existence of polar crystalline phases, including the  $\beta$  and  $\gamma$  phases. The dipoles in the  $\beta$  phase are arranged in parallel, providing the highest dipole moment per unit cell and superior piezoelectric properties (Fig. 1d) [10].

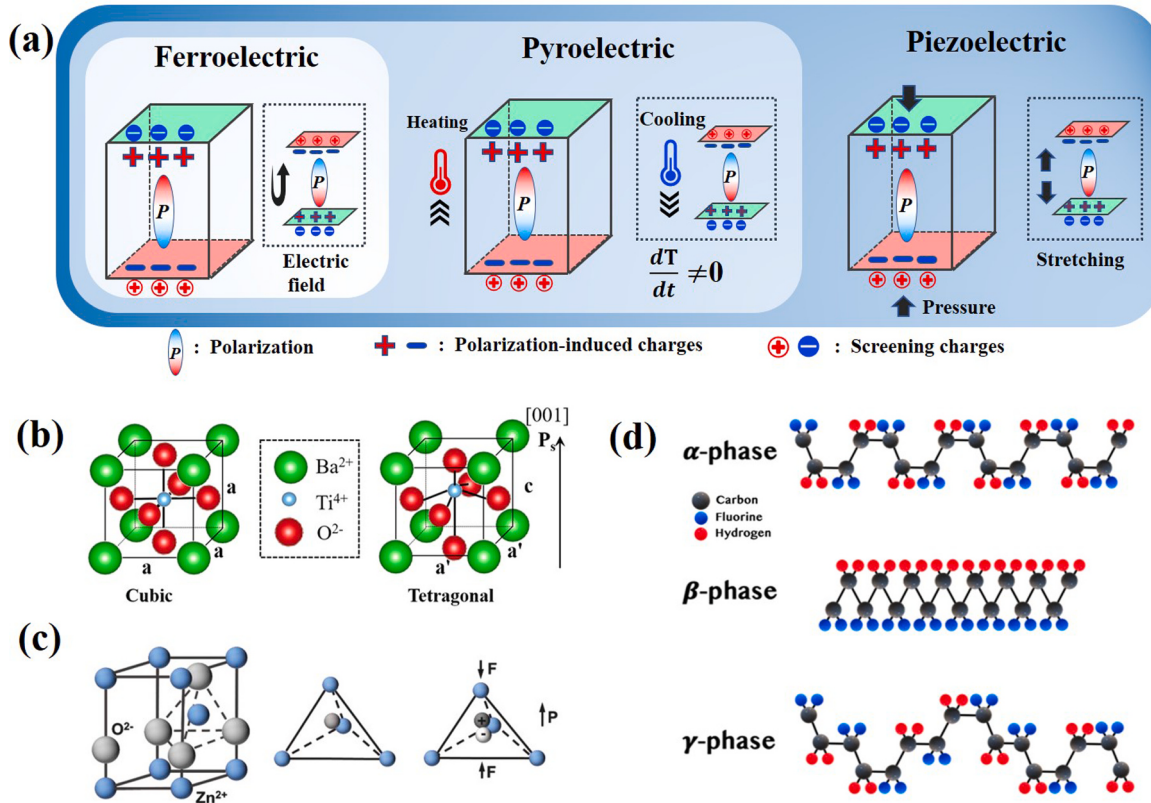


**Fig. 1.** (a) The mechanisms of ferroelectricity (inversion of polarization by applied electric field), pyroelectricity (generation of electric signal upon temperature change) and piezoelectricity (generation of electric signal by applied force). (b) Cubic structure of  $\text{BaTiO}_3$  and tetragonal structure of  $\text{BaTiO}_3$  with  $P_s$  along [001] [8]. (c) Schematic illustrations of atoms and charges distribution in the unit cell of wurtzite-structured  $\text{ZnO}$  [11]. (d) The  $\alpha$ ,  $\beta$ , and  $\gamma$  phase structures of PVDF [10].

## 1.2. Piezocatalysis and piezo-photocatalysis

### 1.2.1. Piezocatalysis

The notion of “piezocatalysis” originates from the polarization of piezoelectric materials, in which piezoelectricity caused by mechanical deformation can evoke various electrochemical redox reactions in the absence of light excitation [12], such as water splitting, degradation of organic pollutants, and inactivation of bacteria [13]. The intensity of polarization can be adjusted by vibration (e.g., ultrasonic waves, mechanical stirring, or water waves) to realize the adsorption and desorption of space charge from surfaces. Compared with photocatalysis or electrocatalysis, piezocatalysis is especially attractive because it only utilizes mechanical energy in nature, suggesting reduced dependence on light and electricity [14].

The currently employed typical piezocatalytic process can be described as follows: The piezoelectric material generates a built-in electric field under mechanical stress (stirring or ultrasonic vibration), which drives free  $e^-$  and  $h^+$  migration to the surface of the piezoelectric material. This phenomenon triggers redox reactions to form reactive oxygen species (ROS), further leading to water splitting, degradation of organic pollutants,  $CO_2$  reduction, and bacterial disinfection [13,15]. Water splitting to produce  $H_2$  driven by a piezopotential, which is generated by ZnO microfibers and BaTiO<sub>3</sub> microdendrites under ultrasonic irradiation, was first reported by Hong et al. in 2010, and a piezoelectrochemical (PZEC) effect for the direct conversion of mechanical energy to chemical energy was proposed [16]. When external mechanical energy is applied, it results in a deformation of piezoelectric fibers or dendrites, and a strain-induced electric potential is formed on the surface to drive redox reactions via free surface charge transfer (Fig. 2a). Subsequently, Hong et al. reported that the PZEC effect was also applied to the degradation of a dye of Acid Orange (AO7) in the presence of BaTiO<sub>3</sub> microdendrites under sufficient applied electric potential [17].

In 2013, Starr et al. conducted a general theoretical analysis of the piezocatalytic process using piezoelectric, semiconductor, molecular orbitals, and electrochemical frameworks, indicating that enabling high electrochemical activity requires piezoelectric materials with a high voltage coupling coefficient, low conductivity, and appropriate dielectric constant to balance piezoelectric and capacitive effects [18]. In 2015, Starr et al. reviewed the fundamental principles of the coupling effect between piezoelectric polarization and electrochemical processes, including the direct utilization of piezoelectric potential to drive electrochemical reactions (piezocatalysis) [19]. The piezocatalytic effect of single- and few-layer MoS<sub>2</sub> nanoflowers was first discovered in 2016, exhibiting an ultra-high degradation activity in the dark by introducing external mechanical strains [20]. Since 2018, many piezoelectric materials, including NaNbO<sub>3</sub> [21], Pb(Zr<sub>1-x</sub>Ti<sub>x</sub>)O<sub>3</sub> [22], BiFeO<sub>3</sub> [23], ZnSnO<sub>3</sub> [24], ZnO [25], ZnS [26], LiNbO<sub>3</sub> [27], CdS [28], have been successively investigated as piezocatalysts.

The morphologies of piezocatalysts mostly have 1D structures (e.g., nanowires, nanorods, and microfibers) and 2D structures (e.g., nanoplates and nanosheets), and the piezoelectric potential produced by 1D and 2D materials is higher than that of nanoparticles (NPs) under the same vibration intensity [29]. In addition to the morphologies of piezocatalysts, several factors affect their efficiency, including phase composition [30,31], structural symmetry, metal-ion doping, noble metal deposition [32], and oxygen vacancies [33].

### 1.2.2. Piezo-photocatalysis

Combining piezoelectric materials with visible light photocatalysts has been considered an effective method for achieving the separation and migration of photo-induced carriers. Piezoelectric materials can generate an internal electric field (IEF) under strain. This IEF provides a driving force for the transport of photo-induced charges in the bulk and on the surface of photocatalysts, consequently promoting their

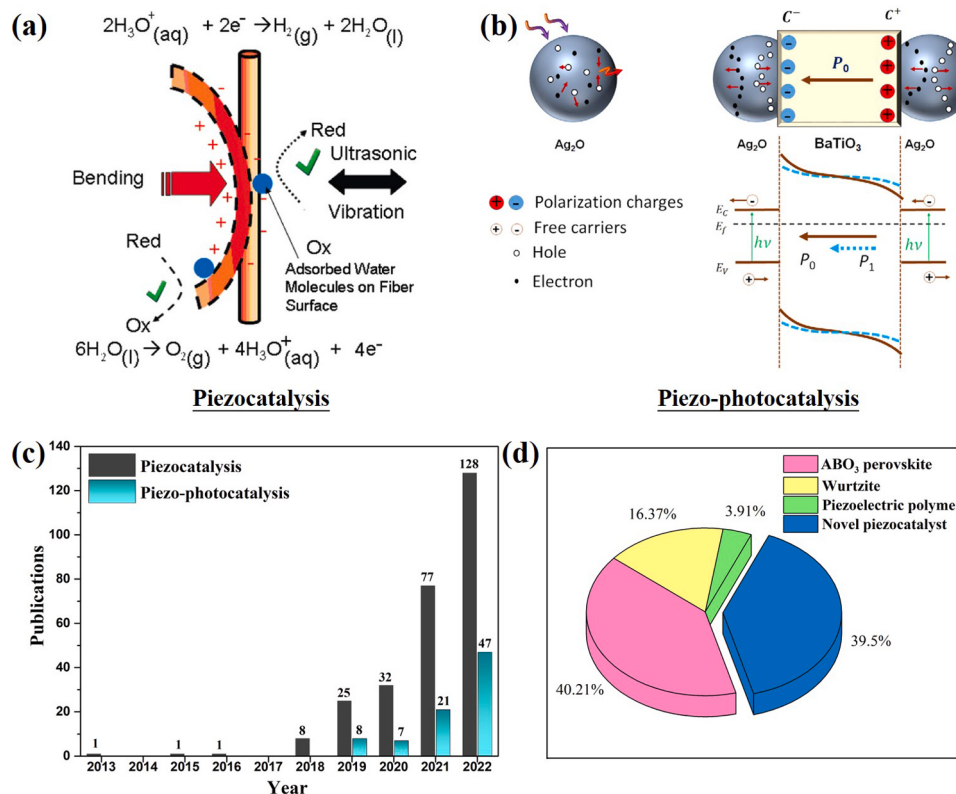


**Fig. 2.** Possible Mechanisms of piezocatalysis (a)[16] and piezo-photocatalysis (b)[34]. (c) Publications on piezocatalysis and piezo-photocatalysis from 2013 to 2022. The publication numbers were collected from the Web of Science using the key words “piezocatalysis” and “piezo-photocatalysis”. (d) The proportion in percentage of piezocatalysts type from 2013 to 2022.

separation and inhibiting their recombination. This new catalytic mechanism of simultaneously utilizing solar energy and mechanical energy is called “piezo-photocatalysis.” Li et al. developed a BaTiO<sub>3</sub>/Ag<sub>2</sub>O hybrid catalyst and tested the degradability of the organic dye rhodamine B (RhB) via simultaneous ultrasonic excitation and UV exposure [34]. The spontaneous polarization potential of BaTiO<sub>3</sub> nanocrystals generated under periodic ultrasonic excitation can act as an alternating built-in electric field to separate photo-induced carriers from Ag<sub>2</sub>O on the two opposite sides of BaTiO<sub>3</sub> nanocubes, thus inhibiting the recombination of carriers. This phenomenon can significantly enhance the photocatalytic activity and cyclic performance of the hybrid BaTiO<sub>3</sub>/Ag<sub>2</sub>O (Fig. 2b).

Usually, the combination of piezo-photocatalysts takes the form of piezoelectric/semiconductor composites, primarily core–shell nanostructures, in which the core is composed of piezoelectric materials (e.g., ZnO, BaTiO<sub>3</sub>, and NaNbO<sub>3</sub>), while the shell consists of visible light photocatalysts (e.g., CuS, FeS, and Ag<sub>2</sub>O). Certain piezoelectric materials with low bandgaps also possess photocatalytic properties, i.e., photocatalytic and piezoelectric properties, coexisting in a single material, which can simultaneously generate both piezopotential and photo-induced charges. Not only are photogenerated e<sup>-</sup> and h<sup>+</sup> generated under light illumination, but a strain-induced polarization electric field is also produced to facilitate charge separation for surface reduction and oxidation. A typical material is BiFeO<sub>3</sub> [35].

Research on piezocatalysis and piezo-photocatalysis is still at an early stage. Fig. 2c shows the number of publications on piezocatalysis and piezo-photocatalysis from 2013 to 2022. The number depicts a rapid uptrend, suggesting the popularization of piezocatalysis and piezo-photocatalysis in energy and environmental science under the current global energy crisis. Although the investigation time is relatively short, great progress has been achieved in this field and has gradually become a research hotspot. Fig. 2d shows the proportion (in percentage) of piezocatalyst types from 2013 to 2022, which are classified as perovskite, wurtzite, piezoelectric polymer, and other novel piezocatalysts. According to the data, the proportions of perovskite, wurtzite, and piezoelectric polymers are 40.21%, 16.37%, and 3.91%, respectively. In addition to traditional piezoelectric materials, certain novel piezoelectric materials are also emerging as efficient catalysts. The novel piezocatalyst comprises 39.5% of the total research on piezocatalysis, indicating the increasing interest of researchers to explore and develop novel piezocatalysts.

### 1.3. Novel piezocatalysts

Many novel piezoelectric materials are currently being used in piezocatalysis. For instance, layered transition metal dichalcogenides (TMDCs) that are not piezoelectric in their bulk form become piezoelectric when reduced to a single atomic layer as a result of their broken inversion symmetry. In addition to TMDCs, a variety of 2D materials, such as black phosphorus and hexagonal boron nitride, have been extensively investigated for their piezoelectric properties when thinned down to a few or even a single atomic layer. Moreover, certain 2D materials, such as graphene (Gr), are intrinsically nonpiezoelectric even-numbered in the monolayer form, but their piezoelectricity can be effectively engineered in Gr by adatom adsorption or by incorporating noncentrosymmetric in-plane defects. Therefore, through proper modification, novel materials lacking piezoelectricity can be designed to be piezoelectrics and used for piezocatalysis. Thus, although research on traditional piezoelectric materials in piezocatalysis has been on a large scale, the recent emergence of novel piezoelectric materials may open up a new development direction.

In the past few years, several reviews on piezocatalysis and piezo-photocatalysis focusing on surface chemistry, synthesis methods, properties, and applications of traditional piezoelectric materials have been published [36]. A few of them also briefly introduce novel piezocatalysts and piezo-photocatalysts covering TMDCs, bismuth-layered structure

materials, and other 2D materials. However, owing to the rapid development of this research field, a comprehensive review focusing on the types and piezoelectricity principles of various novel piezocatalysts and piezo-photocatalysts is necessary to provide readers with a better understanding of the state-of-the-art progress in this dynamic research field.

This review first introduces the piezoelectricity verification of various novel piezocatalytic or piezo-photocatalytic nanomaterials with reference to both computational predictions and experimental characterization. Second, the state-of-the-art crystal structures, physical properties, and applications, including renewable energy generation (water splitting and CO<sub>2</sub> reduction) and environmental remediation (organic pollutant degradation), of various novel piezocatalytic or piezo-photocatalytic nanomaterials are summarized. Third, the crucial role of the polarization-induced IEFs of these novel piezoelectric materials in carrier separation and transmission is explored. Finally, the current research status and challenges and the perspectives of novel piezoelectric materials for piezocatalytic or piezo-photocatalytic applications are summarized. The unique advantages of novel piezoelectric materials are expected to substantially expand their catalytic applications.

## 2. 2D layered transition-metal dichalcogenide-based piezocatalysts

### 2.1. Structure

2D layered TMDCs have emerged as a new type of van der Waals material since the successful discovery of Gr. 2D TMDCs have a chemical formula of MX<sub>2</sub> (M = transition metal, e.g., W, Mo, and X = Te, Se, S) with a layered crystal structure. Depending on the coordination environments of M, TMDCs can crystallize in a variety of polytypic structures, such as the 1 T phase (trigonal symmetry), 2 H phase (hexagonal symmetry), and 3 R phase (rhombohedral symmetry) [37], and have attracted the attention of scientists owing to their favorable electronic, optical, and mechanical properties and nontoxic nature.

The atomic structure diagram of molybdenum disulfide (MoS<sub>2</sub>) with three different crystal phases is shown as an example in Fig. 3a. The side and top views of 1 T-monolayer MoS<sub>2</sub>, 2 H-bilayer MoS<sub>2</sub>, and 3 R-bilayer MoS<sub>2</sub> are presented from left to right [38]. The most widely studied TMDCs are the 2 H phase from a transition metal of group VI, such as MoS<sub>2</sub>, with the unit cell structure shown in Fig. 3b and c [39]. Layered MoS<sub>2</sub> is formed by a hexagonal arrangement of Mo (blue sphere) and S (golden sphere) atoms stacked together to create S–Mo–S sandwiches (Fig. 3b). Each layer is bonded together by weak van der Waals forces [40]. Within the layers, S and Mo atoms are strongly bound via covalent bonds, resulting in a MoS<sub>2</sub> monolayer with a high Young's modulus that is comparable to that of stainless steel [41], good chemical stability [42], and thermal stability reaching 1100 °C [43,44]. The bandgap of MoS<sub>2</sub> is strongly dependent on the number of layers. MoS<sub>2</sub> is an indirect bandgap semiconductor in its bulk form with a bandgap of 1.2 eV, and it becomes a direct bandgap semiconductor when thinned to a monolayer with a bandgap of 1.8 eV [43,45,46]. The aforementioned properties of TMDC materials have been explored in many fields, including field-effect transistors [44], photodetectors [43,47], valleytronics [48,49], and many other flexible photonic and optoelectronic devices [37,42,50].

### 2.2. Verification of piezoelectricity

The premise that TMDC materials can be used in piezocatalysis is that they must have piezoelectric properties. A 2 H-MoS<sub>2</sub> monolayer does not have an inversion center (Fig. 3c). Therefore, 2 H-MoS<sub>2</sub> can exhibit piezoelectric properties in monolayered structures in theory due to the lack of inversion symmetry in the crystal structure. In 2012, Duerloo et al. reported for the first time that many 2 H-TMDC

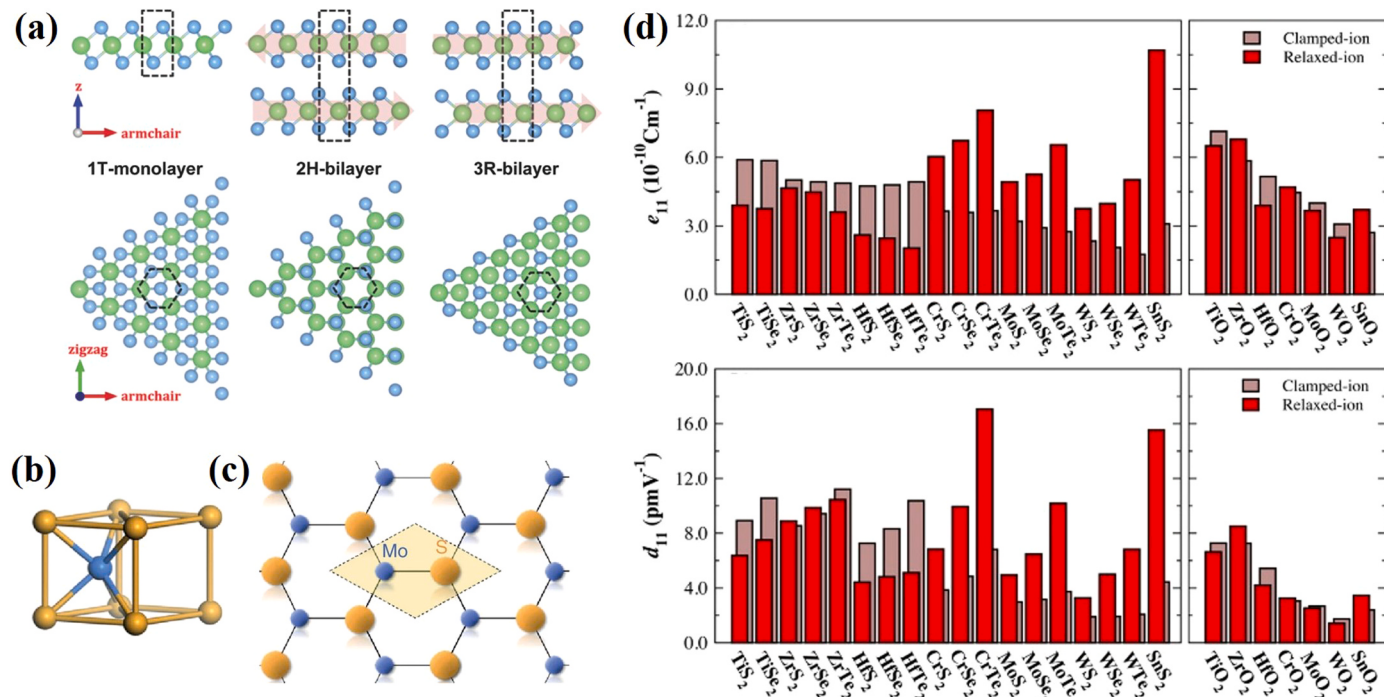


**Fig. 3.** (a) Schematic view of  $\text{MoS}_2$  with 1 T, 2 H, and 3 R phase [38]. (b) Coordination environment of Mo in the structure of  $\text{MoS}_2$  [39]. (c) A top view of the monolayer  $\text{MoS}_2$  lattice, the shaded region bounded by dashed lines corresponds to one primitive cell [39]. (d) Calculated clamped and relaxed-ion piezoelectric stress ( $e_{11}$ ) and piezoelectric strain ( $d_{11}$ ) coefficients [56].

monolayers are in fact piezoelectric; they calculated the materials' piezoelectric and elastic stiffness coefficients based on density functional theory (DFT) at the generalized gradient approximation level of theory [51]. Then, Blonsky et al. identified several 2D TMDCs that exhibit piezoelectricity and determined their piezoelectric coefficients by adopting symmetry analysis and density functional perturbation theory, which were 3.65, 4.55, and 7.39 pm/V for  $\text{MoS}_2$ ,  $\text{MoSe}_2$ , and  $\text{MoTe}_2$ , respectively [52]. Subsequently, many studies have determined the piezoelectricity and piezoelectric coefficients of TMDCs via DFT theoretical calculations [53–55]. Alyörük et al. predicted that not only the Mo- and W-based members of this family but also other materials with  $M = \text{Cr}$ ,  $\text{Ti}$ ,  $\text{Zr}$ , and  $\text{Sn}$  exhibit highly promising piezoelectric properties. The corresponding calculated value of the piezoelectric stress ( $e_{11}$ ) and piezoelectric strain ( $d_{11}$ ) coefficients by using first-principles calculations based on DFT is given in Fig. 3d [56]. However, the 1 T metallic phase of  $\text{MoS}_2$  with a tetragonal structure has no piezoelectricity [57], whereas the 3 R phase of  $\text{MoS}_2$  can evoke strong valley polarization and excite strong nonlinear optical signals regardless of the parity of layer number because of its persistent non-centrosymmetric stacking mode [58].

The piezoelectricity of 2D TMDCs has been theoretically verified but lacks experimental results. In 2014, Wang's group reported the first experimental study of the piezoelectric properties of 2D  $\text{MoS}_2$  [59]. They mechanically exfoliated  $\text{MoS}_2$  flakes and transferred them onto a polyethylene terephthalate flexible substrate to develop a flexible device with a single-layered  $\text{MoS}_2$  flake. When the flexible substrate was bent mechanically, uniaxial strain could be applied to  $\text{MoS}_2$  with a magnitude proportional to the inverse bending radius (Fig. 4a–d). The induced polarization charge was produced by applying strain to the device. Their work confirmed that cyclic stretching and release of thin  $\text{MoS}_2$  flakes with odd-numbered atomic layers could produce oscillating piezoelectric voltage and current outputs; however, no output was observed for flakes with an even number of layers (Fig. 4e). Zhang's group provided experimental evidence of piezoelectricity in a free-standing monolayer  $\text{MoS}_2$  flake via different experimental methods and a measured piezoelectric coefficient of  $e_{11} = 2.9 \times 10^{-10} \text{ C}\cdot\text{m}^{-1}$  (Fig. 4f and g) [60].

Moreover, the measured piezoelectric coupling strength followed the  $\cos 30^\circ$  dependence predicted from the crystalline threefold symmetry (Fig. 4h and i). The measurement of the intrinsic piezoelectricity in these free-standing crystals could avoid substrate effects, such as doping and parasitic charges (Fig. 4j). They also confirmed that piezoelectricity only existed in odd-numbered layers in which inversion symmetry could break, which is in sharp contrast to the  $\text{MoS}_2$  bulk form lacking piezoelectricity (Fig. 4k).

The aforementioned studies indicate that relevant piezoelectric devices, such as piezotransistors [61], sensors, and piezo-photoelectric devices [62,63], could be successfully fabricated using monolayer  $\text{MoS}_2$  flakes. These piezoelectric and piezo-photoelectric devices may play an important role in flexible electronics, flexible optoelectronic devices, wearable devices, and human-machine interfacing in the future.

### 2.3. Applications in piezocatalysis and piezo-photocatalysis

With piezoelectricity supported by theory and experiments, monolayer or few-layered TMDCs have also recently been widely used in the fields of piezocatalysis and piezo-photocatalysis. Wu et al. first discovered that  $\text{MoS}_2$  nanoflowers (NFs) could be prepared by a simple hydrothermal method, and they exhibited ultrahigh piezocatalytic activity on RhB dye in the dark after introducing external mechanical strains [20]. SEM and TEM images revealed the  $\text{MoS}_2$  NFs to be composed of nanopetals, with each nanopetal consisting of abundant amounts of single- and few-layered  $\text{MoS}_2$  (Fig. 5a). The degradation ratio of RhB dye was approximately 93% in only 60 s, corresponding to a kinetic rate constant of  $40,336 \text{ ppm}\cdot\text{L}\cdot\text{mol}^{-1}\cdot\text{s}^{-1}$ , which can be regarded as the fastest degradation rate among the reported values (Fig. 5b). Piezoresponse force microscopy (PFM) revealed a significant amount of piezoelectric potential generated on the edge sites of abundant single- and few-layered  $\text{MoS}_2$  NFs (Fig. 5c). The authors suggested that spontaneous polarization from abundant odd-numbered layers of  $\text{MoS}_2$  NFs could induce an electric field under mechanical stress. This phenomenon created a significant piezoelectric potential for the release of an electric

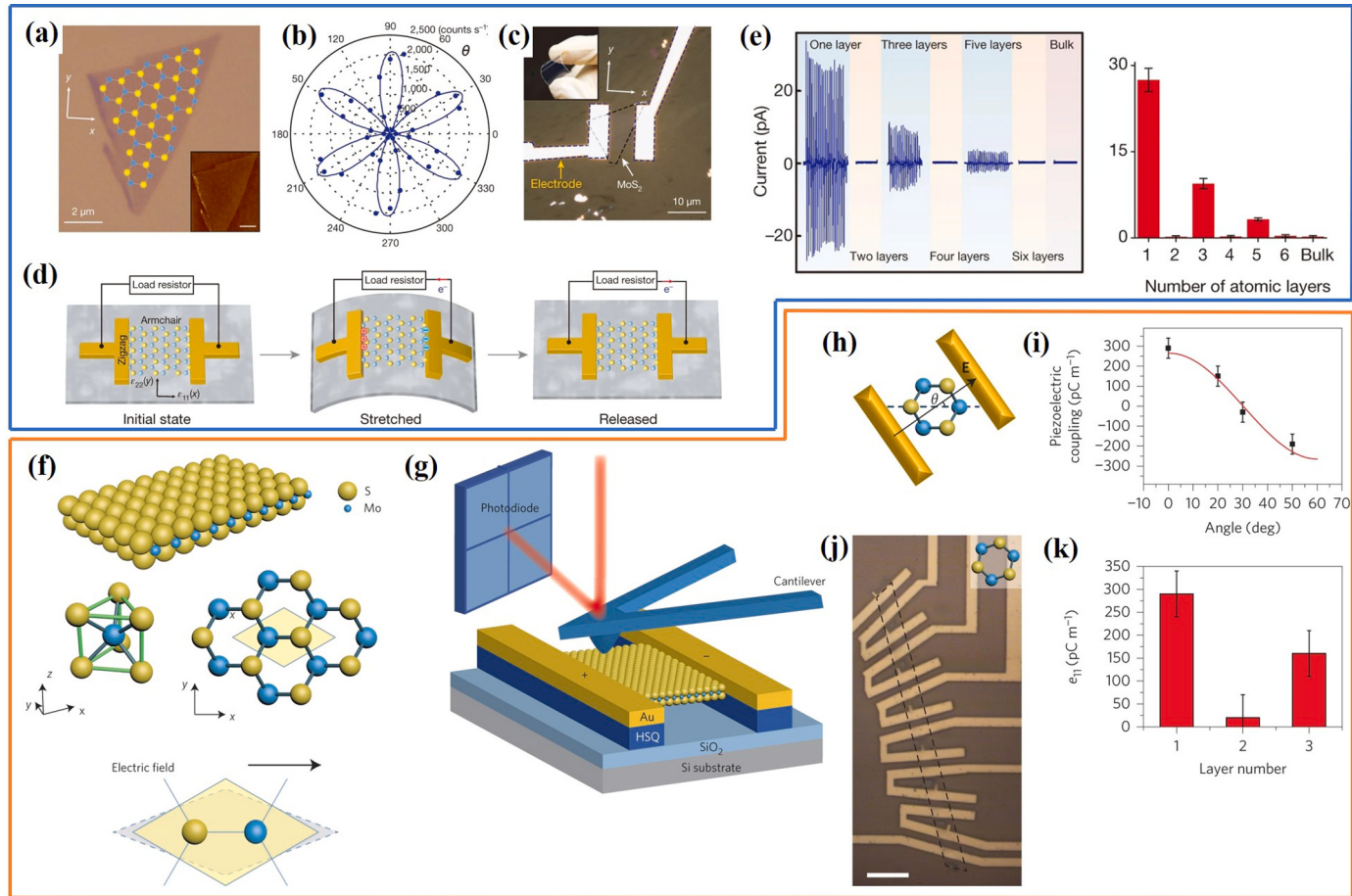


**Fig. 4.** (a) Optical image of the single-atomic layer MoS<sub>2</sub> flake (blue and yellow spheres represent Mo and S atoms, respectively). (b) Polar plot of the SH intensity from single-layer MoS<sub>2</sub> as a function of the crystal's azimuthal angle  $\theta$ . (c) A typical flexible device with single-layer MoS<sub>2</sub> flake and electrodes at its zigzag edges. (d) Operation scheme of the single-layer MoS<sub>2</sub> piezoelectric device. (e) Evolution of the piezoelectric outputs with increasing number of atomic layers (n) in MoS<sub>2</sub> flakes [59]. (f) Composition of monolayer MoS<sub>2</sub> and dipole change under external electric field. (g) Schematic diagram of device for measuring in-plane piezoelectric stress. (h) The rotation of the MoS<sub>2</sub> crystal with respect to the electric field. (i) Measured piezoelectric coupling strength (square data points) followed the  $\cos 3\theta$  dependence (the red fitting curve). (j) Optical image of multiple electrode pairs integrated on a long stripe of MoS<sub>2</sub> (dashed outline) rotated by 10° at each section. (k) Relationship between measured piezoelectric coefficient and number of MoS<sub>2</sub> layers [60].

charge to separate the carriers, which was a major cause of the high degradation activity. Then, they explored the ultrahigh efficient degradation activity of single- and few-layered MoSe<sub>2</sub> NFs in terms of the piezocatalytic effect (Fig. 5d–f) [64]. The degradation rate of MoSe<sub>2</sub> NFs reached 69,889 ppm·L·mol<sup>-1</sup>·s<sup>-1</sup>, which exceeded that of MoS<sub>2</sub> NFs.

Subsequently, to distinguish the piezoelectric catalytic and adsorption effects of MoS<sub>2</sub> NFs, Wu et al. prepared a highly active free radical (i.e., hydroxyl radical or OH<sup>·</sup>) solution, i.e., MoS<sub>2</sub> NFs (~99.9 wt%), which were removed by centrifugation after ultrasonic vibration in deionized water for 30 min; the remaining solution was a free radical solution (Fig. 5g) [65]. The pink RhB dye could instantly be decomposed by the free radical solution and transform into a transparent solution. The intensity of the OH<sup>·</sup> radical was proportional to the MoS<sub>2</sub> NF concentration in the aqueous solution, proving that the OH<sup>·</sup> radicals were created by the piezoelectricity of MoS<sub>2</sub>. The degradation of RhB dye molecules can be attributed to the piezoelectricity of MoS<sub>2</sub> rather than the adsorption effect. Moreover, a remarkable hydrogen peak was observed in the MoS<sub>2</sub> aqueous and ethanol solutions under ultrasonic vibration by gas chromatography—mass spectrometry. The intensity of hydrogen generation increased with increasing MoS<sub>2</sub> concentration, which demonstrates that hydrogen gas could be produced using the piezoelectricity of MoS<sub>2</sub> NFs. The key consideration in prolonging the lifetime of the radical is for the F-center defects to trap the free carriers and bond with the radical, allowing their charge neutrality to be

maintained (Fig. 5h).

Three kinds of few-layered TMDC samples (MoS<sub>2</sub>, WS<sub>2</sub>, and WSe<sub>2</sub>) could also produce H<sub>2</sub> from water and degrade tetracycline and RhB under ultrasonic vibration, as confirmed by Li et al. [66]. The H<sub>2</sub> production rates and degradation rate of organic molecules followed the order of MoS<sub>2</sub> > WS<sub>2</sub> > WSe<sub>2</sub>, which is in good agreement with the PFM analysis. Furthermore, the piezoelectric stress coefficient ( $\epsilon_{11}$ ) values could be calculated by first-principles-based density functional perturbation theory, suggesting a high correlation between piezoelectricity and catalytic performance.

Many improvement strategies have also been applied, such as phase regulation and various modifications, including defect engineering, doping, noble metal deposition, and heterostructure construction.

### 2.3.1. Phase regulation

As previously mentioned, 1 T-TMDCs with a tetragonal structure lack piezoelectricity. Interestingly, 1 T/2 H hybrid MoSe<sub>2</sub> nanosheets have piezoelectric hydrogen evolution reaction (HER) performance, which is superior to that of pure 2 H-phase nanosheets; this difference can be explained by the former materials' high carrier concentration, high electrical conductivity, naturally formed semiconductor-metal (M-S) heterojunction, and strain-induced flexoelectric and piezoelectric coupling effect, providing the potential application of polymorphic TMDCs in hydrogen production [67].

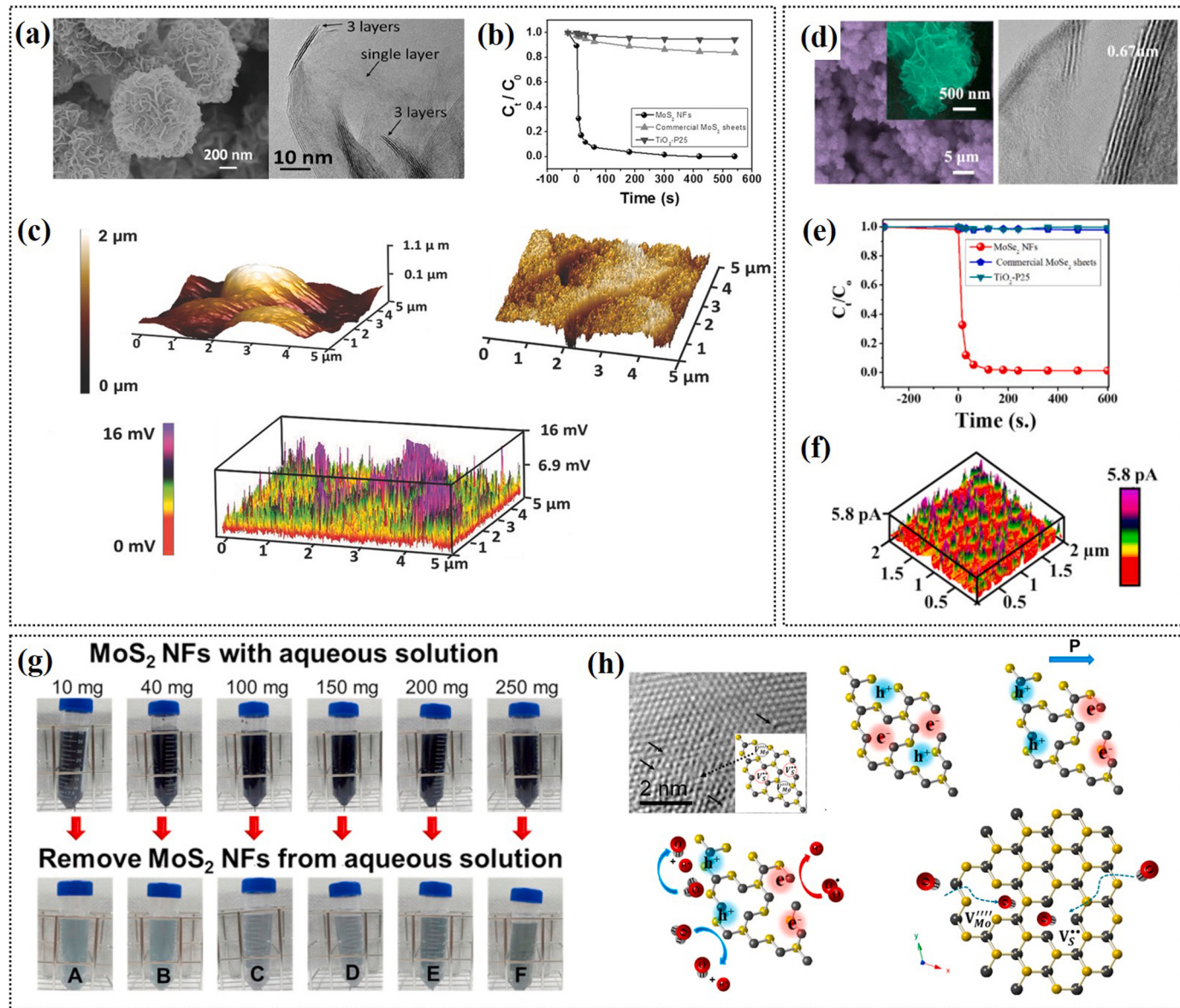


**Fig. 5.** (a) The MoS<sub>2</sub> NFs consists of a great number of nanopetals with rich single- and few-layers. (b) The degradation ratio of the RhB dye using the MoS<sub>2</sub> NFs, commercial MoS<sub>2</sub>, and TiO<sub>2</sub>-P25, under ultrasonic wave in the dark. (c) The 3D AFM images of the MoS<sub>2</sub> NFs and the output piezoelectric potential responsive image [20]. (d) The size of the MoSe<sub>2</sub> NFs and the spacing between the two layers. (e) The comparison of the degradation ratio for all catalysts. (f) The tunneling atomic force microscopy image of the current distribution in MoSe<sub>2</sub> nanoflowers [64]. (g) The digital photos of the before and after removal the MoS<sub>2</sub> nanoflowers from the aqueous solution. (h) HRTEM image of vacancies defects of the single-layer MoS<sub>2</sub>, and the diagram of the radical trapped by F-center [65].

In contrast to the 2 H-TMDCs that exhibit piezoelectric properties only in odd-numbered layered structures, all structures in both the single layer and the bulk of 3R-MoS<sub>2</sub> lead to a large piezoelectric coefficient based on molecular dynamics simulation, further indicating their great potential in piezocatalysis and other related applications [68]. 3 R bulk-MoS<sub>2</sub> materials have excellent nonlinear SHG conversion efficiency (i.e., two orders of magnitude larger than that of 2 H bulk-MoS<sub>2</sub>) owing to the breaking of their inversion symmetry [38].

Ren et al. proved the out-of-plane piezoelectricity of the 3 R phase with even-numbered layers via finite element simulation. By comparing the piezo-degradation efficiency of 1 T/2 H-MoS<sub>2</sub> with that of 1 T/3R-MoS<sub>2</sub> nanosheets, 1 T/3R-MoS<sub>2</sub> was found to have the highest degradation rate, benefitting from the combination of metal and semiconductor phases and cooperation with the in-plane and out-of-plane piezoelectricity of the arbitrary multilayer 3 R phase [69].

In addition, the piezocatalytic performance of MoS<sub>2</sub> can be adjusted by introducing defects, doping, noble metal deposition, and

heterostructure construction, which is highly similar to the processes involved in photocatalysis.

### 2.3.2. Defect engineering

When traditional piezoelectric ceramic materials contain voids or cracks during production, their piezoelectric performance generally decreases. However, catalytic materials with some structural flaws or atomic defects can benefit from creating large specific surface areas and multiple active sites [70]. Both DFT calculations and experimental verification have shown an improved piezoelectric effect at the edges of MoS<sub>2</sub> nanosheets, whereas the basal planes are catalytically inert [71, 72]. Ma et al. developed multiflawed MoS<sub>2</sub> nanosheets with abundantly exposed edges by using a hydrothermal method of controlling the molar ratio of Mo and S (Fig. 6a) [73]. An ultrahigh enhanced piezocatalytic activity for the degradation of the antibiotic ciprofloxacin was observed in MoS<sub>2</sub> nanosheets with many flaws and active edge sites. This finding can be attributed to the increased asymmetry of the multiflawed MoS<sub>2</sub>

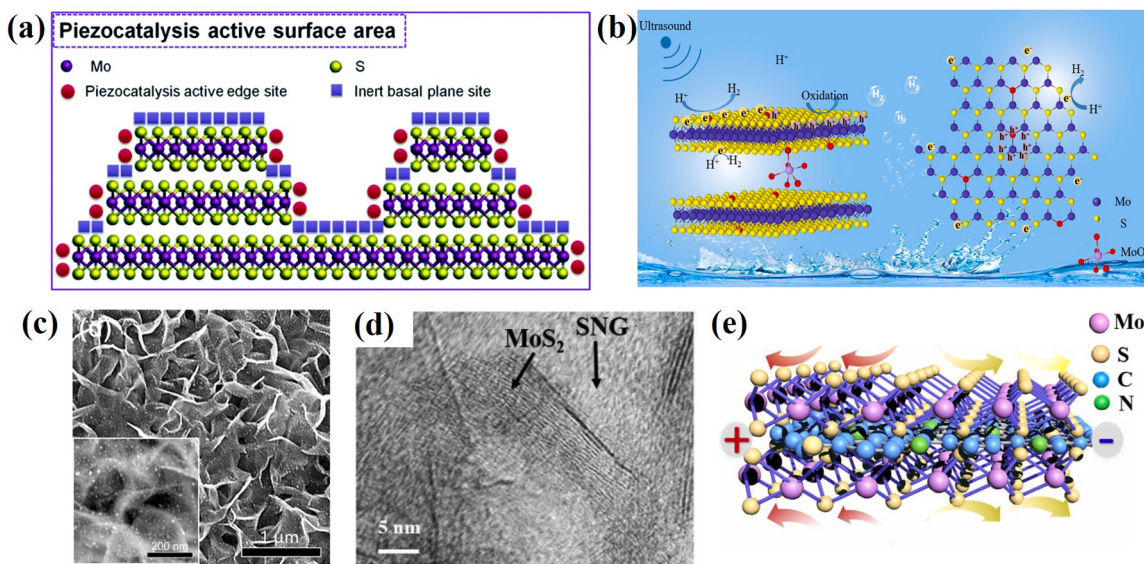


**Fig. 6.** (a) Schematic illustration of the piezocatalytic active edge sites in multi-flaw MoS<sub>2</sub> [73]. (b) The schematic diagram of piezocatalytic H<sub>2</sub> production [79]. (c) High-magnification image of Au-MoS<sub>2</sub> @CFs [81]. (d) HRTEM images of heterogeneous MoS<sub>2</sub>@SNG. (e) The piezoelectric mechanism proposed for the MoS<sub>2</sub> @SNG under ultrasonic vibration [83].

compared with the flaw-free MoS<sub>2</sub>, which leads to the efficient separation of e<sup>-</sup>-h<sup>+</sup> pairs caused by the strain-induced piezoelectric field.

### 2.3.3. Doping

Element doping has been widely used as an effective strategy to adjust the electronic structure of catalysts; the resulting increased catalytic activity is mainly used in the field of photocatalysis or electro-catalysis. Yein et al. synthesized co-doped MoS<sub>2</sub> nanosheets and applied them in the piezocatalytic degradation of methylene blue (MB) dye [74]. The introduction of Co doping into a few layers of the MoS<sub>2</sub> structure (Co-MoS<sub>2</sub>) improved the piezocatalytic degradation of MB dye within 60 s owing to the generation of a new catalytic active center, high conductivity, and accelerated charge transfer by the piezoelectric response. The piezoelectricity of MoS<sub>2</sub> existed only in the monolayer and a few odd-numbered layers resulting from the centrosymmetric structure of the even-numbered layers. In fact, odd- and even-numbered layers of MoS<sub>2</sub> obtained by existing preparation methods, including the hydrothermal method, mechanical stripping [75,76], and chemical vapor deposition (CVD) [77,78], coexist but limit the efficient utilization of MoS<sub>2</sub> during piezocatalysis. Lei et al. selected oxygen as a doping element to prepare oxygen-doped MoS<sub>2</sub> (O-MoS<sub>2</sub>) (Fig. 6b) [79]. The introduction of oxygen could break the symmetry of a single layer and two adjacent layers, leading to a larger variation in spontaneous polarization. Compared with MoS<sub>2</sub> with layer-dependent piezoelectricity, O-MoS<sub>2</sub> broke the layer-dependent piezoelectricity and induced out-of-plane polarization. Benefiting from the optimized piezoelectricity, the optimized O-MoS<sub>2</sub> exhibited a higher concentration of carriers and a higher piezocatalytic H<sub>2</sub> evolution rate (47.75 μmol·h<sup>-1</sup>·g<sup>-1</sup>), which was more than twice that of the original MoS<sub>2</sub> (20.19 μmol·h<sup>-1</sup>·g<sup>-1</sup>).

### 2.3.4. Noble metal deposition

The loading of noble metals onto piezoelectric catalysts forms a Schottky junction that can benefit the separation and transfer of active charge carriers and has recently attracted wide interest [80]. Chou et al. proved that gold (Au) NPs could be deposited on MoS<sub>2</sub> NSs to further improve their catalytic efficiency, subsequently prolonging the lifetime of e<sup>-</sup>-h<sup>+</sup> pairs and enhancing the generation of ROS [81]. Fig. 6c shows the distribution of the Au NPs on the terrace sites of MoS<sub>2</sub> NSs. Au NPs were dispersed on the terrace sites of MoS<sub>2</sub>, and a typical Schottky interface was formed between MoS<sub>2</sub> and Au. IEF was generated by MoS<sub>2</sub>

under an external mechanical force. This phenomenon resulted in the separation of e<sup>-</sup>-h<sup>+</sup> pairs and their movement to the surface between MoS<sub>2</sub> and Au to react with water and oxygen via electrochemical reactions, subsequently generating ROS.

### 2.3.5. Heterostructure construction

The rapid recombination of e<sup>-</sup>-h<sup>+</sup> pairs in catalysts remains one of the main factors limiting catalytic efficiency, whether for photocatalysis or piezocatalysis. An effective strategy to overcome these drawbacks is the construction of heterojunctions by coupling piezoelectrics and semiconductors to efficiently enhance the catalytic ability.

The MoS<sub>2</sub> @TiO<sub>2</sub> heterojunction with a high surface area and numerous active sites (i.e., few-layered MoS<sub>2</sub> nanosheets loaded onto exposed facets of anatase TiO<sub>2</sub> nanorods) has a much higher carrier concentration than pure TiO<sub>2</sub> nanorods or MoS<sub>2</sub> nanosheets because of the presence of numerous carriers separated and collected in edge sites by the piezoelectric effect of MoS<sub>2</sub> [82]. Pan et al. constructed a sandwich-like structure with MoS<sub>2</sub> grown on both sides of S- and N-co-doped Gr (MoS<sub>2</sub>@SNG) to efficiently hinder the stacking of MoS<sub>2</sub> nanosheets, control the layers of MoS<sub>2</sub> and directly improve the piezopotential (Fig. 6d) [83]. MoS<sub>2</sub>@SNG exhibited ultrahigh piezocatalytic activities for removing MB, bisphenol A, and nitrobenzene because of the reduced stacking of MoS<sub>2</sub> nanosheets and accelerated electron transfer of the heterogeneous Gr substrate (Fig. 6e).

A type II piezoelectric heterojunction of BaTiO<sub>3</sub>/MoS<sub>2</sub> (BTO/MS) can inhibit the recombination of e<sup>-</sup>-h<sup>+</sup> pairs, proving the ability of the BTO-MS combination to greatly enhance the piezoelectric effect and promote the degradation efficiency of antibiotic ornidazole pollutants [84]. The loading of few-layered MoS<sub>2</sub> nanosheets on the surface of CuS not only avoids the agglomeration of MoS<sub>2</sub> nanosheets but also efficiently separates the electrons/holes through the piezoelectric field created by the few-layered MoS<sub>2</sub> under mechanical stirring and the formation of a CuS/MoS<sub>2</sub> heterojunction, accounting for the high piezocatalytic efficiency [85]. Other piezoelectric composite catalysts with excellent piezocatalytic performance are layered TiO<sub>2</sub>/MoS<sub>2</sub> [86] and few-layered MoS<sub>2</sub>/graphdiyne [87]. So far, most of the degradation products of organic pollutants have been converted into CO<sub>2</sub> instead of value-added chemical raw materials. Ran et al. developed a piezocatalytic technology coupled with advanced oxidation processes (AOPs) to achieve the redox conversion of various organic pollutants to CO [88]. In this process, the organics are first oxidized to carbonate through

peroxymonosulfate-based AOPs, and then the carbonate is converted to CO through piezoelectric reduction using  $\text{Co}_3\text{S}_4/\text{MoS}_2$  catalyst under ultrasonic vibration.

### 2.3.6. Others

The problem of catalyst recycling can be solved by building catalytic membranes composed of catalyst particles and organic polymer membranes to omit the steps of catalyst recycling while simultaneously reducing the pollutants. Typical examples of organic polymers are polyacrylonitrile, polydimethylsiloxane (PDMS), PVDF, and polytetrafluoroethylene [89]. Masimukku et al. assembled PDMS embedded with  $\text{WS}_2$  NFs (PDMS/ $\text{WS}_2$ ) for the piezo-degradation of the organic dye RhB to avoid destroying the catalyst under mechanical force while ensuring the floating of materials in the organic solution that could cause secondary pollutants [90]. The decomposition ratio of the dye reached ~99% by PDMS/ $\text{WS}_2$  with highly repeatable piezo-degradation activity, indicating possible future industrial applications in environmental purification. When PDMS (without piezoelectricity) was replaced by PVDF (with piezoelectricity), the catalytic performance improved because of the efficient transfer and suppressed recombination rate of charge carriers by the piezopotential [91]. Ma et al. prepared flexible and recyclable  $\text{MoS}_2/\text{PVDF}$  composite membranes by electrospinning [92]. The electrospun PVDF fibers acted as both the piezocatalysts and the substrate. The incorporation of  $\text{MoS}_2$  resulted in more polar  $\beta$ -phase formation in PVDF fibers, thereby enhancing the intrinsic piezoelectric activity of PVDF and increasing the number of catalytically active sites and the density of free charge carriers. The piezo-degradation efficiency of oxytetracycline reached 93.08% within 24 min owing to the synergistic effects of the  $\text{MoS}_2$  nanosheets and the high proportion of PVDF  $\beta$ -phase PVDF fibers.

In addition, the mechanical energy in the natural environment, such as wind energy, water flow energy, and noise, usually has the characteristics of low frequency and low power. However, the piezocatalysis and piezo-photocatalysis reported in recent literature mostly use ultrasonic vibrations with very high frequencies as mechanical excitation forces that are difficult to deploy in practical applications. So far, low-frequency piezocatalysis or piezo-photocatalysis has not been widely reported. Verma et al. examined the piezocatalytic activity of electrospun PVDF/ $\text{WS}_2$  membrane under ultrasonication as well as under low-frequency vibrations. The degradation rate of MB dye by PVDF/ $\text{WS}_2$  membrane within 240 min was 65% under ultrasonic vibration and 44% under low-frequency vibration, demonstrating the feasibility of piezocatalysis under low-frequency vibration [93]. The PVDF/ $\text{WS}_2$  textile prepared by Shi et al. could degrade 97.3% RhB (10 mg/L) in merely 30 min under gentle vibration at 240 rpm by an orbital shaker, confirming that the high piezocatalytic performance can be achieved even under the action of small mechanical energy [94]. Therefore, using low-frequency vibration to study piezocatalysis is expected to open new applications of piezoelectricity in catalytic processes.

Current research on 2D layered piezoelectric TMDCs has not only been limited to the abovementioned materials. Many other piezoelectric TMDCs, such as  $\text{SnS}_2$  [95],  $\text{Bi}_2\text{S}_3$  [96,97], and  $\text{SnSe}$  [98], have also been widely used in piezocatalysis. Nonetheless, the aforementioned studies strongly confirm the promotion of the piezoelectric effect on catalytic performance by using TMDCs. Hence, more novel 2D piezoelectric TMDCs and suitable modification methods for optimizing the catalytic activities should be explored.

## 3. Bismuth-layered structure material-based piezocatalysts

Bismuth-layered structure materials with a layered structure built by alternately stacked  $[\text{Bi}_2\text{O}_2]^{2+}$  slices and anions and/or anionic groups have a unique crystal structure, rich atomic coordination, and an appealing or favorable hybrid electronic band structure. This unique structural configuration allows bismuth-layered materials to easily adapt to crystal structure design and acquire crystallographic

orientations suitable for facet control, band gap adjustment, and defect modifications; these approaches have shown huge potential in solar energy catalytic conversion. The interleaved units of bismuth-layered structure materials can be classified into Aurivillius-type, Sillén-type, and Aurivillius- or Sillén-related composite structures.

### 3.1. Aurivillius type

#### 3.1.1. Structure

Bismuth-layered materials with Aurivillius structures, also known as bismuth-layered perovskite ferroelectrics (BLSFs), which were discovered by Aurivillius in 1949, have attracted the attention of materials scientists owing to the asymmetric center featuring spontaneous polarization, unique layered crystal structures, and anisotropic physical properties of these materials. The general chemical formula of BLSFs is  $(\text{Bi}_2\text{O}_2)^{2+}(\text{A}_{m-1}\text{B}_m\text{O}_{3m+1})^{2-}$ , and its crystal structure can be regarded as the alternate arrangement of the fluorite-like layer  $(\text{Bi}_2\text{O}_2)^{2+}$  and the perovskite-like layer  $(\text{A}_{m-1}\text{B}_m\text{O}_{3m+1})^{2-}$ , where  $m$  is the number of stacked oxygen octahedra along the direction perpendicular to the layers. The structure allows for numerous chemical substitutions at the A and B sites, where A can be a mono-, di-, or trivalent ion such as  $\text{Na}^+$ ,  $\text{K}^+$ ,  $\text{Pb}^{2+}$ ,  $\text{Ba}^{2+}$ ,  $\text{Ca}^{2+}$ ,  $\text{Sr}^{2+}$ , and  $\text{Bi}^{3+}$ , with B representing a small-sized cation with tetra-, penta-, and hexavalent ions such as  $\text{Ti}^{4+}$ ,  $\text{Nb}^{5+}$ ,  $\text{Ta}^{5+}$ , and  $\text{W}^{6+}$  [99] (Fig. 7a) [100], further suggesting a wide range of physical properties. Numerous BLSFs ( $\text{Bi}_2\text{WO}_6$  and  $\text{Bi}_2\text{MoO}_6$  at  $m = 1$ ;  $\text{SrBi}_2\text{Nb}_2\text{O}_9$ ,  $\text{CaBi}_2\text{Nb}_2\text{O}_9$ ,  $\text{SrBi}_2\text{Ta}_2\text{O}_9$ , and  $\text{BaBi}_2\text{Nb}_2\text{O}_9$  at  $m = 2$ ;  $\text{Bi}_4\text{Ti}_3\text{O}_{12}$  at  $m = 3$ ;  $\text{BaBi}_2\text{Ti}_4\text{O}_{15}$ ,  $\text{SrBi}_2\text{Ti}_4\text{O}_{15}$ , and  $\text{CaBi}_2\text{Ti}_4\text{O}_{15}$  at  $m = 4$ ;  $\text{Sr}_2\text{Bi}_4\text{Ti}_5\text{O}_{18}$  and  $\text{Pb}_2\text{Bi}_4\text{Ti}_5\text{O}_{18}$  at  $m = 5$ ) have been widely studied in the fields of piezoelectric/ferroelectric ceramics and ferroelectric random access memories [101] and are considered good catalysts for water splitting and photodegradation of organic compounds [102].

BLSFs are the most widely studied materials in the field of ferroelectric/piezoelectric ceramics operated at high temperatures because of their high Curie temperatures ( $T_c$ ), unique spontaneous polarization, and excellent resistance to thermal depoling [103,104]. However, these Aurivillius-type ceramics prepared by conventional methods often have low density due to the anisotropic growth tendency of lamellar grains and poor piezoelectric properties caused by spontaneous polarization almost confined in the plane [105]. Hot pressing and spark plasma sintering have been traditionally used to produce highly dense ceramics. Fortunately, Aurivillius-type bismuth-layered structure nanopowders can be directly used for catalysis into ceramics without the need for sintering. Moreover, the hybridization of Bi 6 s and O 2p at the band edge position is a general feature of BLSFs, and most BLSFs can harvest part of visible light, indicating their possibility of use in photoelectric, photovoltaic, and photocatalytic applications. Consequently, Aurivillius-type bismuth-layered structure materials have become research hotspots in the field of piezocatalysis or piezo-photocatalysis, specifically because of their unique polarization-induced intrinsic electric field and excellent photoabsorptive activity.

The spontaneous polarization of the BLSFs is approximately confined in the plane. Taking  $\text{SrBi}_2\text{Ta}_2\text{O}_9$  as an example, its crystal structure consists of a  $\text{Bi}_2\text{O}_2$  layer interleaved with  $\text{TaO}_6$  perovskite groups (Fig. 7b). The shape of the  $\text{TaO}_6$  octahedron is imperfect; it is elongated along the  $c$ -axis, indicating the occurrence of a dipole moment. The length of the Ta-O bond along the tetragonal  $c$ -axis is slightly shorter, whereas the chemical bond pointing to the  $\text{Bi}_2\text{O}_2$  layer is longer, resulting in a net spontaneous polarization along the  $a$ -axis but a lack of polarization along the pseudotetragonal  $c$ -axis (Fig. 7c) [100]. In addition, the direction of spontaneous polarization is in the  $a-b$  plane of the perovskite-like layers for even-numbered  $m$ , whereas spontaneous polarization is found in the  $c$ -axis for odd-numbered  $m$ . For example,  $\text{Bi}_4\text{Ti}_3\text{O}_{12}$  with  $m = 3$  is polarized along both the  $a$ -axis ( $50 \mu\text{C}/\text{cm}^2$ ) and  $c$ -axis ( $4 \mu\text{C}/\text{cm}^2$ ).

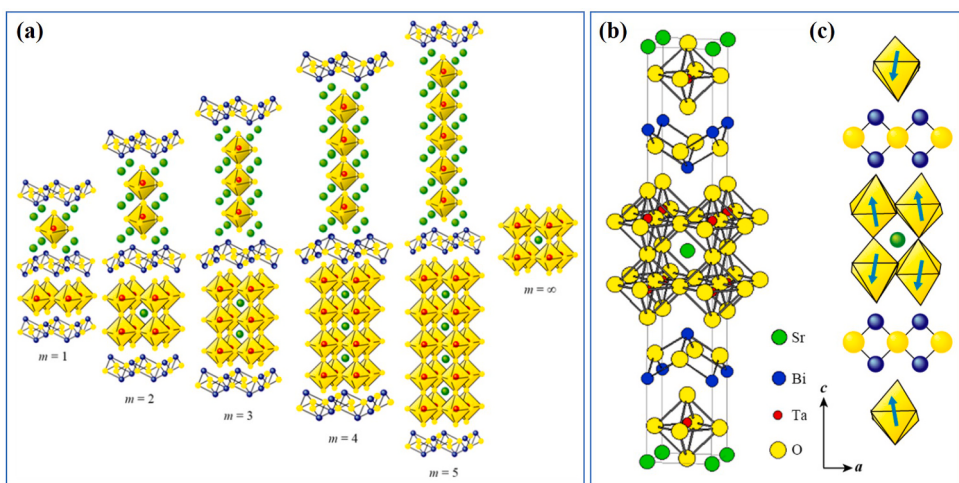


**Fig. 7.** Schematic crystal structures of Aurivillius-type bismuth layer-structured materials depending on stacking number  $m$  (a), crystal structure of  $\text{SrBi}_2\text{Ta}_2\text{O}_9$  (b), and the direction of spontaneous polarization (c) [100].

### 3.1.2. Applications in piezocatalysis and piezo-photocatalysis

A considerable number of Aurivillius-type piezocatalysts or piezo-photocatalysts perform well in organic pollutant degradation and water splitting. Accordingly, new piezocatalysts or piezo-photocatalysts with Aurivillius structures for the development of piezocatalysis and piezo-photocatalysis need to be explored. This study introduces the currently published Aurivillius-type bismuth-layered structure materials in piezocatalysis and piezo-photocatalysis in the order of small to large  $m$  values.

**3.1.2.1.  $m = 1$ .**  $\text{Bi}_2\text{WO}_6$ , the simplest member of the Aurivillius family ( $m = 1$ ), is composed of an alternate stacking of fluorite-like  $[\text{Bi}_2\text{O}_2]^{2+}$  layers along the  $c$ -axis and pseudoperovskite  $[\text{WO}_4]^{2-}$  layers [106].  $\text{Bi}_2\text{WO}_6$  adopts a noncentrosymmetric crystal structure that results in macroscopic polarization, with spontaneous polarization occurring along the  $c$ -axis mainly within the  $\text{WO}_6$  layers (parallel to the layers) due to the distortion of the oxygen octahedrons (Fig. 8a). The polarization of each constituent ion along the  $c$ -axis calculated by He et al. is given in Fig. 8b. The total polarization is approximately  $45.5 \mu\text{C}/\text{cm}^2$ . The  $\text{Bi}_2\text{O}_2$  layer with ionic conductivity and the  $\text{WO}_6$  layer with insulating nature are stacked alternately along the  $b$ -axis in the  $\text{Bi}_2\text{WO}_6$  crystal (Fig. 8c). Finally, a polarization electric field induced by spontaneous polarization of  $\text{Bi}_2\text{WO}_6$  is used as a driving force to guide electrons and holes to move oppositely (Fig. 8d) [99]. This scenario suggests that  $\text{Bi}_2\text{WO}_6$  is a promising 2D material in catalysis, including water splitting for  $\text{H}_2$  evolution,  $\text{CO}_2$  reduction, and degradation of organic pollutants.

In 1999, Kudo et al. [107] determined that  $\text{Bi}_2\text{WO}_6$  has photocatalytic activity for  $\text{O}_2$  evolution. Subsequently,  $\text{Bi}_2\text{WO}_6$  has been widely studied as a photocatalyst, especially in terms of its shape control and visible-light-driven photocatalytic activities [108–111]. However, to the best of our knowledge, no systematic research on the piezocatalysis or piezo-photocatalysis of  $\text{Bi}_2\text{WO}_6$  has been conducted. Hao et al. first investigated the piezocatalytic performance of  $\text{Bi}_2\text{WO}_6$  nanosheets as a piezocatalyst to degrade organic pollutants. The piezocatalytic efficiency of  $\text{Bi}_2\text{WO}_6$  nanosheets reached  $\sim 96\%$  after 35 min with good reusability and recyclability. The excellent piezocatalytic activity was attributed to the piezoelectric effect that induces electric charges to accelerate carrier transport during chemical redox reactions (Fig. 8e) and the inclination of the conduction and valence bands of piezocatalysts driven by high piezoelectric potential (Fig. 8f) [106]. The reaction kinetic rate constant  $k$  of  $\text{Bi}_2\text{WO}_6$  nanosheets is much higher than that of other reported piezocatalysts, which further validates its high piezocatalytic activity and broad future application prospects in the environment and energy domains (Fig. 8g).

Kang et al. reported that piezoelectric  $\text{Bi}_2\text{WO}_6$  nanosheets with in-plane spontaneous polarization have selective adsorption ability for anionic MO in neutral and acidic solutions, which allowed RhB to be selected as the target pollutant. The net contribution of piezocatalysis of the  $\text{Bi}_2\text{WO}_6$  nanosheets to RhB degradation was moderate compared with other known perovskite materials. The piezocatalytic activity was positively correlated with the specific surface area of the  $\text{Bi}_2\text{WO}_6$  nanosheets. The synergistic effect of adsorption and piezocatalysis in piezoelectric adsorbents was useful for the in situ regeneration of the piezocatalyst [112]. Kang et al. further studied the influence of the crystal symmetry and oxygen vacancies of  $\text{Bi}_2\text{WO}_6$  nanosheets on the performance of piezocatalysts by degrading RhB solution under ultrasonic vibration [113]. The  $\text{Bi}_2\text{WO}_6$  nanosheets with small grain size, large orthorhombic distortion, and low oxygen vacancy concentration modulated by annealing in an  $\text{O}_2$  atmosphere at  $400^\circ\text{C}$  exhibited better piezocatalytic performance, proving the high sensitivity of the piezocatalytic efficiency of  $\text{Bi}_2\text{WO}_6$  nanosheets to microstructures, including the phase structure, crystal size, and oxygen vacancy concentration.

Synergetic piezo-photocatalysis by coupling light irradiation and ultrasonic vibration is a promising strategy to purify organic pollutants in wastewater. Lei et al. tested the piezo-photocatalytic activity of NF-like  $\text{Bi}_2\text{WO}_6$  by coupling low-power white LED (9 W) irradiation and ultrasonic vibration (120 W) [114]. The efficiency of RhB degradation from piezo-photocatalysis was 17.5 and 2.1 times that of photocatalysis alone and piezocatalysis alone, respectively. A schematic of the piezo-photocatalysis of the NF-like  $\text{Bi}_2\text{WO}_6$  is shown in Fig. 8h. The photogenerated  $e^-$  and  $h^+$  in photocatalysis mode recombined easily, whereas the concentration of the phonon-excited free charge carriers was quite low in piezocatalysis mode. During the coupling of these two catalytic modes, the ultrasound-induced built-in piezoelectric field originating from piezoelectric polarization efficiently suppressed the recombination of photoexcited  $e^-$  and  $h^+$ , and then the degradation efficiency was greatly improved. Hu et al. synthesized ultrathin  $\text{Bi}_2\text{WO}_6$  nanosheets with a thickness of approximately 10 nm and a transverse length of 100–400 nm by a two-step hydrothermal process and investigated their piezo-photocatalytic activity by decomposing RhB [115]. The degradation ratio was approximately 98.39% within 70 min, which was 1.59 and 2.01 times higher than that of photocatalysis alone and piezocatalysis alone, respectively. Obviously, the effective combination of piezocatalysts and photocatalysts is a more promising wastewater treatment method.

The combination of piezoelectrics and traditional photocatalysts to form heterojunctions is an effective strategy to further improve catalytic performance. A Z-scheme  $\text{Bi}_2\text{WO}_6/\text{black TiO}_2$  ( $\text{B-TiO}_2$ ) heterostructure

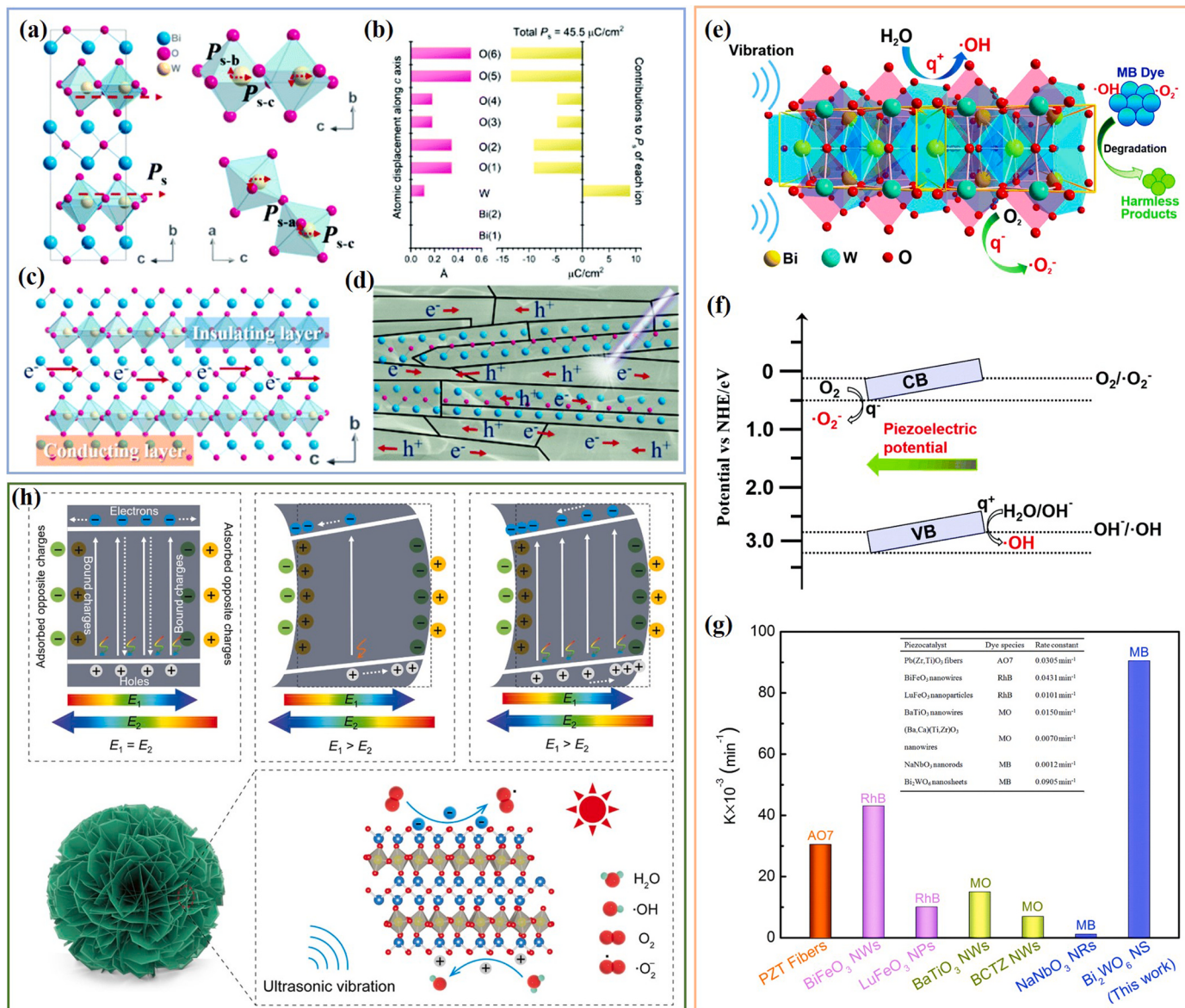


**Fig. 8.** (a) Structure of  $\text{Bi}_2\text{WO}_6$  unit cell and the spontaneous polarization direction. (b) The calculated polarizations of each constituent ion along the  $c$ -axis. (c) Schematic view of alternating stacked  $\text{Bi}_2\text{O}_2$  layers and  $\text{WO}_6$  perovskite layers. (d) Illustration of the migration of photoexcited  $e^- - h^+$  pairs [99]. (e) Schematic principle of the piezocatalytic decomposition of MB dye. (f) A diagram of energy band tilt driven by piezoelectric potential. (g) A comparison of the piezocatalytic reaction kinetics rate constants for representative piezocatalyst systems [106]. (h) Band diagrams of  $\text{Bi}_2\text{WO}_6$  at photocatalysis, piezcocatalysis and piezo-photocatalysis, and schematic illustration for piezo-photocatalysis of the nanoflower-like  $\text{Bi}_2\text{WO}_6$  [114].

designed by Shen et al. for the first time was applied as a piezo-photocatalyst for RhB degradation [116]. The RhB degradation efficiency for 0.5 wt%  $\text{Bi}_2\text{WO}_6/\text{B}-\text{TiO}_2$  reached 98.43% in 60 min under simultaneous sunlight and ultrasonic irradiation, a value much higher than that of independent photocatalysis (54.23%) and independent piezcocatalysis (26.33%). The high catalysis efficiency was attributed to the extended light absorption capacity and the high ability to separate photogenerated carriers through the polarization field inside  $\text{Bi}_2\text{WO}_6$ .

**3.1.2.2.  $m = 2$ .** Li et al. synthesized the layered perovskite photocatalyst  $\text{ABi}_2\text{Ta}_2\text{O}_9$  ( $\text{A} = \text{Ca}, \text{Sr}, \text{Ba}$ ; changed with increasing ionic radius of the  $\text{A}^{3+}$  ion) by the conventional solid-state reaction method and investigated their photocatalytic activities for water splitting under UV-light irradiation as early as 2008 [117]. The formation rate of  $\text{H}_2$  evolution for the photocatalyst  $\text{SrBi}_2\text{Ta}_2\text{O}_9$  was much higher than that of  $\text{CaBi}_2\text{Ta}_2\text{O}_9$  and  $\text{BaBi}_2\text{Ta}_2\text{O}_9$ , as the angle between the corner-linked  $\text{NbO}_6$  octahedral of  $\text{SrBi}_2\text{Nb}_2\text{O}_9$  was closer to  $180^\circ$  than that of

$\text{CaBi}_2\text{Nb}_2\text{O}_9$ , and the lattice of  $\text{SrBi}_2\text{Nb}_2\text{O}_9$  with an orthorhombic structure was more distorted than that of  $\text{BaBi}_2\text{Nb}_2\text{O}_9$  with a tetragonal structure (Fig. 9a). According to the authors, the crystalline structure and lattice distortion might have played an important role in photo-generated charge separation, eventually affecting the photocatalytic activity at that time [118]. Subsequently, single-phase orthorhombic  $\text{SrBi}_2\text{Nb}_2\text{O}_9$  and tetragonal  $\text{BaBi}_2\text{Nb}_2\text{O}_9$  photocatalysts were synthesized by Wu et al.; they found that the photocatalytic activity in the redox reaction of methyl orange (MO) of the former was better than that of the latter, which could be ascribed to a dipole moment in the  $\text{SrBi}_2\text{Nb}_2\text{O}_9$  crystal [119]. Fig. 9b shows the  $\text{BaBi}_2\text{Nb}_2\text{O}_9$  crystal structure, in which the  $\text{NbO}_6$  octahedra are tilted by less than  $3^\circ$  with respect to the  $c$  axis. The  $\text{NbO}_6$  octahedra are tilted by  $6^\circ$  in  $\text{SrBi}_2\text{Nb}_2\text{O}_9$ . Furthermore,  $\text{SrBi}_2\text{Nb}_2\text{O}_9$  permitted a dipole moment along the perovskite layers ( $c$  axis) because of the distortion of the framework of the perovskite layers, whereas  $\text{BaBi}_2\text{Nb}_2\text{O}_9$  did not. Therefore, the dipole moment in  $\text{SrBi}_2\text{Nb}_2\text{O}_9$  crystals can enhance the separation and

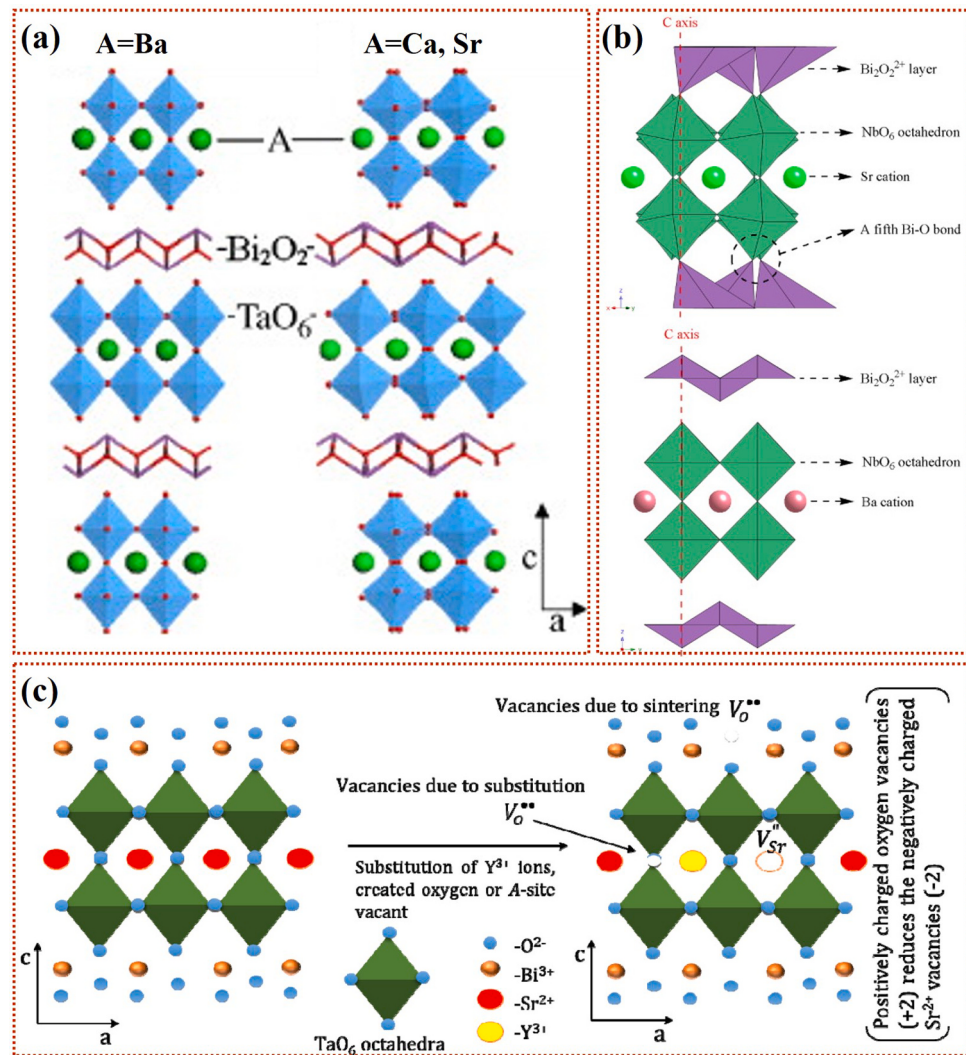


**Fig. 9.** (a) Schematic crystal structure of  $ABi_2Ta_2O_9$  ( $A=Ca, Sr, Ba$ ) [117]. (b) Schematic crystal structure of  $SrBi_2Nb_2O_9$  (top) and  $BaBi_2Nb_2O_9$  (bottom) [119]. (c) Schematic drawing illustrating the charge neutrality based on oxygen and strontium vacancies [120].

transmission of photoexcited  $e^-$  and  $h^+$  and consequently improve the photocatalytic activity.

Senthil et al. investigated the photocatalytic water splitting of  $Y^{3+}$ -modified  $SrBi_2Ta_2O_9$  ferroelectrics ( $Sr_{1-x}Y_{2x/3}Bi_2Ta_2O_9$ ) and found that the a-site vacancy could enhance the rotation of the octahedron, resulting in an improvement in the ferroelectric property (Fig. 9c) [120]. The formation of lattice distortion and the existence of a dipole moment enhanced the water splitting photocatalytic activity by spontaneously separating the charge carriers. Thus, ferroelectrics as photocatalysts can separate the charge carriers through local electric fields created by the dipoles in the domain with a noncentrosymmetric structure.

**3.1.2.3.  $m = 3$ .** Tu et al., the first researchers who reported the piezocatalytic performance of  $Bi_4Ti_3O_{12}$  for the degradation of MO under ultrasonic irradiation, used an ultrasonic-introduced press to induce the generation of positive and negative charges on two opposite surfaces of  $Bi_4Ti_3O_{12}$  [121]. The piezoelectricity of  $Bi_4Ti_3O_{12}$  was attributed to the lack of inversion symmetry in its crystal structure, and the positive and negative charges were distributed to the opposite side. Abundant powerful superoxide (radical  $\cdot O^{2-}$ ) and hydroxyl (radical  $\cdot OH$ ) radicals were produced in the piezoelectric-catalytic process, resulting in efficient degradation. However, the piezocatalytic dye degradation efficiency of  $Bi_4Ti_3O_{12}$  was somewhat low.

Wu et al. supposed that the spontaneous polarizations of randomly

oriented nanocrystals might offset each other, eventually suppressing the total piezoelectric susceptibility. They used layered titanate  $Na_2Ti_3O_7$  as a synthetic precursor and prepared a variety of nanostructured  $Bi_4Ti_3O_{12}$  materials, including rectangular nanoplates, decussated nanoplates, and slice-assembled microspheres; then, they investigated the influences of morphological factors on the piezocatalytic performance (Fig. 10a) [122]. The decussated  $Bi_4Ti_3O_{12}$  nanoplates exhibited an ultrahigh piezocatalytic activity in contrast to other morphologies after degrading the RhB dye solution under ultrasonic vibration. This finding was caused by the large piezoelectric potential difference and the short distance between polar surfaces (Fig. 10b).

Liu et al. fabricated  $Bi_4Ti_3O_{12}$  NSs with simultaneous photoexcitation and piezoelectricity by electrospinning and calcination and studied their piezo-photocatalytic performance with RhB degradation [123]. The piezo-photocatalytic performance with the RhB degradation rate of  $Bi_4Ti_3O_{12}$  NSs calcined at 600 °C was 2.5-fold and 6.7-fold for piezocatalysis alone and photocatalysis alone, respectively. For  $Bi_4Ti_3O_{12}$  NSs with high specific surface areas and small crystal sizes prepared by electrospinning, large piezoelectric polarization and rich oxygen vacancies obtained by annealing served as the key factors for improving the piezo-photocatalytic performance.

$Bi_4Ti_3O_{12}$  nanoplates synthesized by the molten-salt method exhibited better piezo-photocatalytic performance for degrading RhB compared with  $Bi_4Ti_3O_{12}$  nanomaterials synthesized by the solid-state

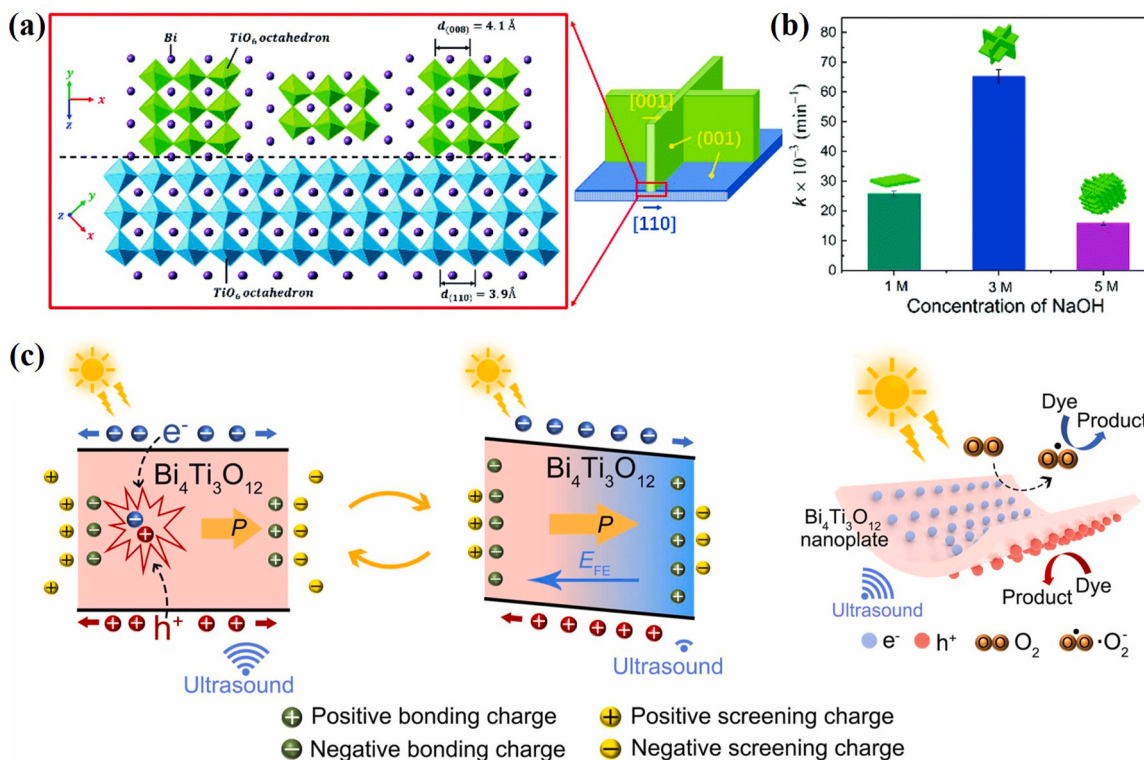


**Fig. 10.** (a) Schematic of vertical grain growth of  $\text{Bi}_4\text{Ti}_3\text{O}_{12}$  nanoplate. (b) The reaction rate constants of  $\text{Bi}_4\text{Ti}_3\text{O}_{12}$  samples with different morphologies [122]. (c) Piezo-photocatalytic mechanisms of  $\text{Bi}_4\text{Ti}_3\text{O}_{12}$  nanoplates and their schematic diagram of piezo-photocatalytic degradation of dye [124].

reaction method and hydrothermal method; this finding could be explained by the nanoplates' good balance of size, shape, crystallinity, and specific surface area [124]. The considerably enhanced piezo-photocatalytic activity was also attributed to the effective

separation of photogenerated carriers caused by the built-in electric field. The corresponding schematic diagram of the piezo-photocatalytic degradation of the dye is shown in Fig. 10c.

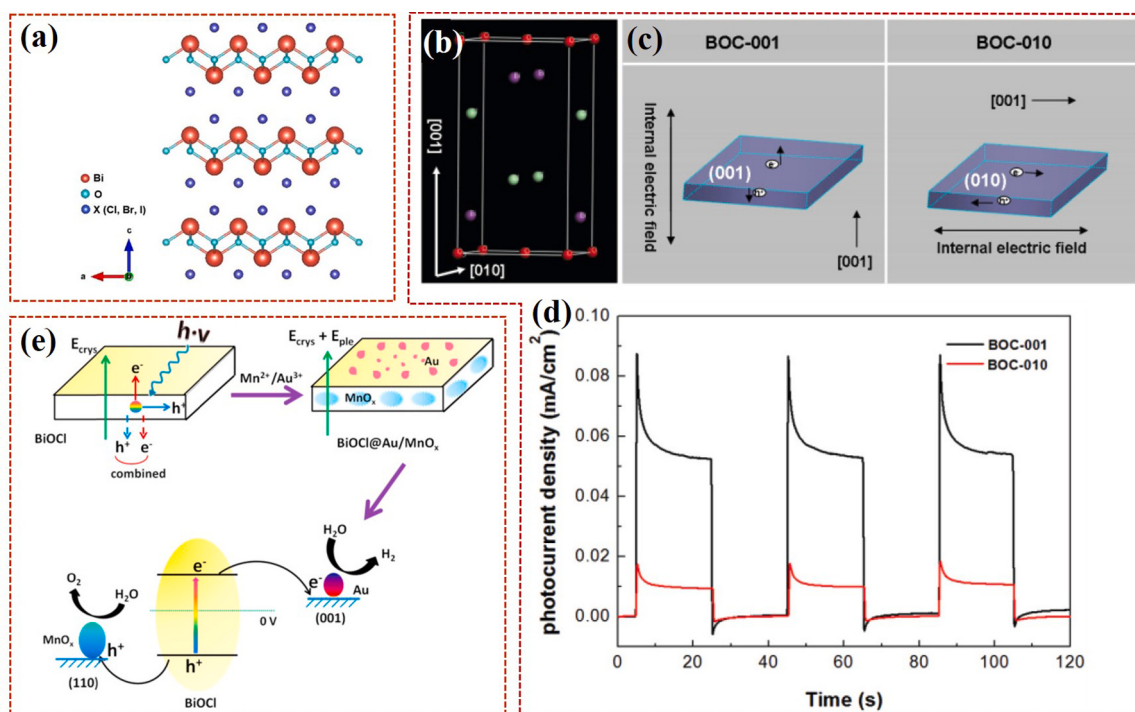


**Fig. 11.** (a) Crystal structure of  $\text{BiOX}$  ( $X = \text{Cl}, \text{Br}, \text{I}$ ) [125]. (b) Atomic model of  $\text{BiOCl}$ . (c) the direction of the internal electric field and (d) photocurrent responses of  $\text{BiOCl}$  under UV-vis irradiation [128]. (e) Schematic diagram of selective deposition of Au and  $\text{MnO}_x$ , and photocatalytic oxygen evolution of  $\text{BiOCl}@\text{Au}/\text{MnO}_x$  [129].

### 3.2. Sillén type

#### 3.2.1. $\text{BiOX}$

Sillén-structured bismuth-layered materials of bismuth oxyhalide with the formula  $\text{BiOX}$  ( $X = \text{Cl}, \text{Br}, \text{I}$ ) and Bi-rich  $\text{Bi}_x\text{O}_y\text{X}_z$  ( $X = \text{Cl}, \text{Br}, \text{I}$ ) or their related solid solutions have been widely used in photocatalysis, with more than 4000 related studies reported in the past decade [125]. As shown in the crystal structure diagram in Fig. 11a,  $\text{BiOX}$  consists of  $\text{Bi}_2\text{O}_2$  layers interlaced by two layers of halogen atoms. The layers were stacked together by nonbonding (van der Waals) interactions through the halogen atoms along the c-axis. The unique layered structure would lead to the non-uniform charge distribution between  $\text{Bi}_2\text{O}_2$  and halogen slices, which could polarize the related atoms and orbitals, generating an IEF that promoted the separation and transfer of photogenerated carriers. The strong intralayer covalent bonding and the weak interlayer van der Waals interaction of  $\text{BiOX}$  resulted in highly anisotropic structural, electrical, optical, and mechanical properties, which were also reported in other reviews [125–127]. These articles mainly focused on the synthesis, modification, photocatalytic application, and mechanisms of bismuth oxyhalide. Subsequently, an increasing number of researchers have become interested in the IEF of  $\text{BiOX}$  and investigated the photocatalytic performance by internal polarization. This present review classifies photocatalysis by using the internal polar field of bismuth oxyhalide as piezo-photocatalysis for discussion.

Jiang et al. first reported the facet-controllable synthesis of  $\text{BiOCl}$  single-crystalline nanosheets with exposed [001] and [010] facets [128] and compared their photocatalytic properties. Given the unique layered structure of  $\text{BiOCl}$  (Fig. 11b), internal static electric fields perpendicular to the  $[\text{Bi}_2\text{O}_2]$  slabs and halogen anionic slabs in  $\text{BiOCl}$  could be induced. The schematic is shown in Fig. 11c. The self-induced IEFs are perpendicular to the nanosheets of BOC-001 but parallel to those of BOC-010. The BOC-001 film electrode had a higher photocurrent than BOC-010 upon comparing the photocurrent responses under UV-vis irradiation, indicating more efficient photo-induced charge separation and transfer in BOC-001 along the [001] direction (Fig. 11d).  $\text{BiOCl}$  nanosheets with exposed [001] facets exhibited higher activity for photodegradation under UV light because of the suitable IEFs. The photochemical labeling effectively verified the orientation of holes and electrons in the [001] and [110] crystal facets of  $\text{BiOCl}$ . Au and  $\text{MnO}_x$  were selectively photodeposited on the [001] and [110] crystal facets of  $\text{BiOCl}$ , respectively; this finding provides evidence for the spatial separation of electrons and holes, further implying the effective avoidance of photogenerated  $\text{h}^+$  and  $\text{e}^-$  recombination (Fig. 11e) [129]. The natural driving force for the “selective” spatial transport of  $\text{h}^+$  and  $\text{e}^-$  to different facets was mainly attributed to the IEF along the c-axis in the  $\text{BiOCl}$  crystal.

Shao et al. [130] used ultrasonic excitation as the only driving force for piezocatalysis, performed an oxygen reduction reaction (ORR) to generate  $\text{H}_2\text{O}_2$ , and realized the piezocatalytic effect over  $\text{BiOCl}$  plates. An alternating electric field would be generated over  $\text{BiOCl}$  under ultrasonic excitation, which could drive charge carriers (electrons) to interact with  $\text{O}_2$  and  $\text{H}_2\text{O}$  and then form  $\text{H}_2\text{O}_2$ . Ismail et al. compared the degradation efficiency of RhB over  $\text{BiOCl}$  microspheres by photocatalysis (~72%), piezocatalysis (~26%), and piezo-photocatalysis (~99%) [131]. Under the high-efficiency synergy of piezocatalysis and photocatalysis, an electric field induced by the vibration of mechanical strain drove the separation of the photogenerated electron-hole pairs, yielding the enhanced decomposition performance of biocatalysis. In addition, the synergistic photocatalytic/piezocatalytic degradation of organic dyes by  $\text{BiOBr}$  was also realized for the first time [132].

The combination of two piezoelectric materials to form a heterojunction is also a good method to further improve piezo-photocatalysis, such as the  $\text{BiOCl}/\text{NaNbO}_3$  heterojunction [133] and  $\text{Bi}_2\text{MoO}_6/\text{BiOBr}$  p-n heterojunctions [134]. In addition to the use of the internal built-in piezoelectric field to effectively prevent the recombination of carriers, the formation of heterojunctions significantly improves the separation

efficiency of photogenerated carriers.

#### 3.2.2. $\text{Bi}_x\text{O}_y\text{X}_z$

Bi-rich bismuth oxyhalides include  $\text{Bi}_3\text{O}_4\text{X}$  ( $X = \text{Cl}, \text{Br}$ ),  $\text{Bi}_5\text{O}_7\text{X}$  ( $X = \text{Br}, \text{I}$ ),  $\text{Bi}_4\text{O}_5\text{X}_2$  ( $X = \text{Br}, \text{I}$ ),  $\text{Bi}_{12}\text{O}_{17}\text{X}_2$  ( $X = \text{Cl}, \text{Br}$ ),  $\text{Bi}_{12}\text{O}_{15}\text{Cl}_6$ ,  $\text{Bi}_{24}\text{O}_{31}\text{X}_{10}$  ( $X = \text{Cl}, \text{Br}$ ), and  $\text{Bi}_7\text{O}_9\text{I}_3$ . Their crystal structures are affected by the type of halide and the O/X ratio. The crystal structure model of  $\text{Bi}_3\text{O}_4\text{X}$  ( $X = \text{Cl}, \text{Br}$ ) shown in Fig. 12a is given as an example. Bi-rich bismuth oxyhalides also have a unique interlayer electric field that can improve the separation rate of photoexcited charges. The typical strategies can be summarized as follows.

For Bi-rich bismuth oxyhalide, Li et al. prepared [001] facet  $\text{Bi}_3\text{O}_4\text{Cl}$  single-crystalline nanosheets with different exposure percentages (95%, 91%, and 86%, which are called BOC-95, BOC-91, and BOC-86, respectively) via the liquid phase exfoliation and hydrothermal recrystallization method and established the correlation of the IEF magnitude with the [001] facet exposure percentage (Fig. 12b) [135]. The photocatalytic degradation rate, photoluminescence emission, electrochemical impedance spectroscopy, and transient photocurrent responses of  $\text{Bi}_3\text{O}_4\text{Cl}$  nanosheets with changing percentages of [001] confirmed that more [001] facet exposure could induce the generation of a stronger IEF and accelerate the separation and transfer of photogenerated carriers, thus enhancing the photocatalytic activity. Tuning the IEF intensity via crystal facet engineering was also provided as a novel strategy for improving photocatalytic performance. Subsequently, adding carbon into  $\text{Bi}_3\text{O}_4\text{Cl}$  could enhance its IEF by 126 times, which could be attributed to the C doping that intensified the non-uniform distribution of charge between  $[\text{Bi}_3\text{O}_4]$  and  $[\text{Cl}]$  slices to the greatest extent (Fig. 12c) [136]. Furthermore, several Bi-rich bismuth oxyhalides and their composites were used in piezoelectric catalysis in self-polarized internal fields, such as  $\text{Bi}_3\text{O}_4\text{Br}$  [137] and  $\text{CNT}/\text{Bi}_4\text{O}_5\text{I}_2$  [138].

### 3.3. Aurivillius- or Sillén-related

Aurivillius- or Sillén-related layered bismuth-based materials, such as  $\text{BiOIO}_3$ ,  $\text{Bi}_2\text{O}_2\text{CO}_3$ ,  $\text{Bi}_2\text{O}_2[\text{BO}_2(\text{OH})]$ , and  $\text{Bi}_2\text{O}_2(\text{OH})(\text{NO}_3)$ , have recently attracted special interest. The crystal structure of these materials is always composed of  $\text{Bi}_2\text{O}_2^{2+}$  fluorite-structure layers and interleaved halide ions or perovskite-like  $(\text{A}_{m-1}\text{B}_m\text{O}_{3m+1})^{2-}$  or  $\text{CO}_3^{2-}/\text{BO}_3^{3-}/\text{NO}_3^-$  anionic blocks. The orderly layered structure was believed to be prone to form an IEF and realize effective charge separation, which enables these materials to achieve enhanced photocatalytic activity, thus triggering substantial interest from researchers and several significant research achievements.

$\text{BiOIO}_3$ , a new Aurivillius-type noncentrosymmetric polar material consisting of alternating  $(\text{Bi}_2\text{O}_2)^{2+}$  cationic layers and  $(\text{IO}_3)^-$  anions, was characterized by Nguyen et al. in 2011 (Fig. 13a) [139]. The  $\text{IO}_3$  trigonal pyramidal structure in  $\text{BiOIO}_3$  makes the positive and negative charge centers asymmetric. This special structure produces a local dipole moment, and the addition of dipole moments in the  $\text{IO}_3$  polyhedral layer leads to macroscopic polarization along the c-axis direction (Fig. 13b).

In 2013, Wang et al. determined that the internal polar field of  $\text{BiOIO}_3$  nanoplates could effectively separate photogenerated  $\text{e}^--\text{h}^+$  pairs in photocatalysis, which was evaluated by photodegradation of MO under UV light irradiation [140]. Density functional calculations confirmed the occurrence of photooxidation on the surface  $\text{IO}_3$  layer, and photoreduction occurred at one edge of the nanoplate under the action of the polarization field. This enhanced photocatalytic activity of  $\text{BiOIO}_3$  nanoplates was attributed to both the heterolayered structure and the internal polar field. Su et al. prepared  $\text{BiOIO}_3$  nanoplates with different thicknesses of 25, 50, and 150 nm and evaluated the photocatalytic  $\text{H}_2$  evolution performance [141]. The  $\text{H}_2$  evolution by the  $\text{BiOIO}_3$  nanoplate increases with its thickness, which was ascribed to the increased internal polar field effect from the increased thickness of the

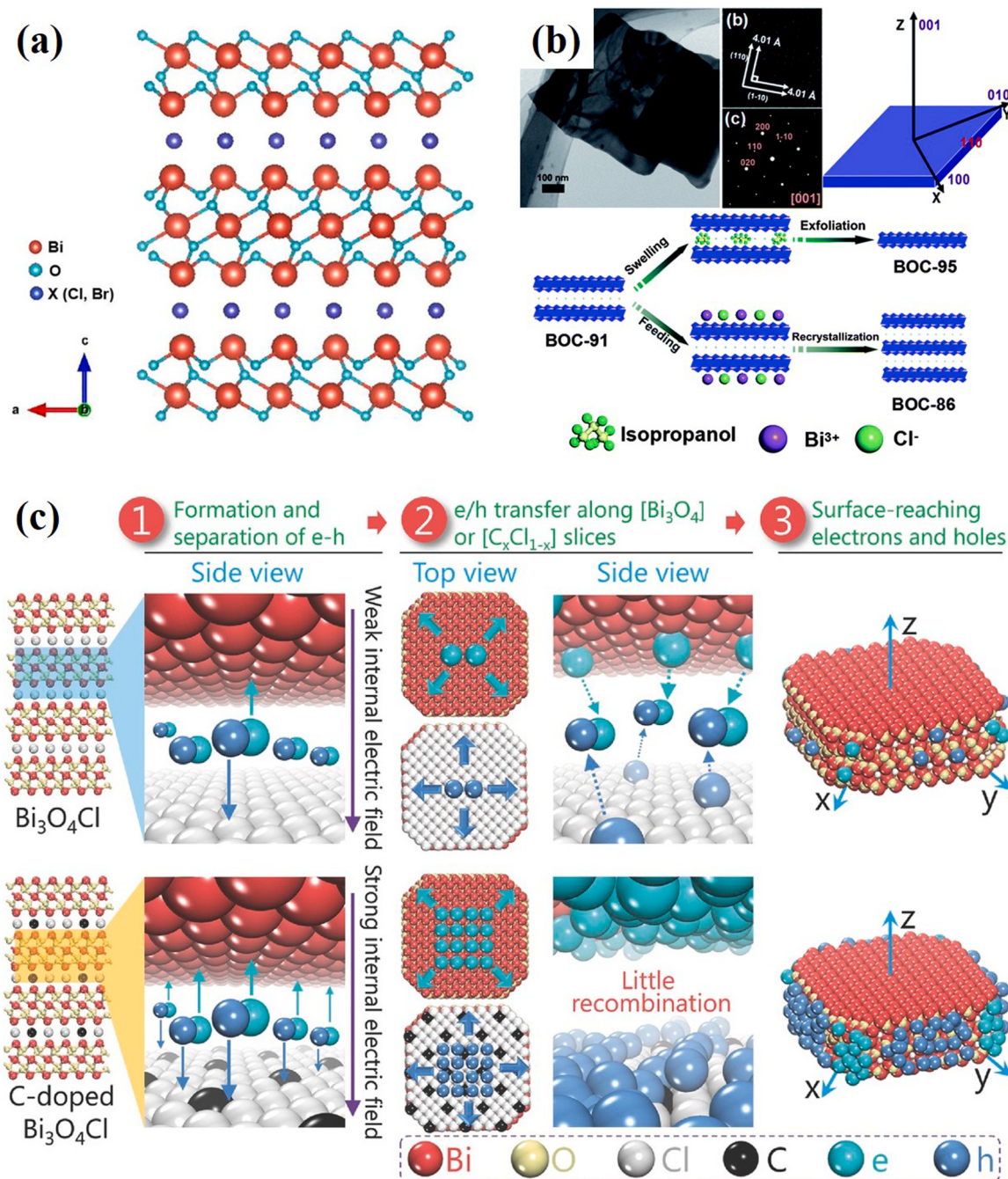


**Fig. 12.** (a) Crystal structure of  $\text{Bi}_3\text{O}_4\text{X}$  ( $\text{X} = \text{Cl}, \text{Br}$ ) [125]. (b) TEM image and schematic illustration of the liquid-exfoliation and hydrothermal-induced recrystallization process for tuning the facet percentages of  $\text{Bi}_3\text{O}_4\text{Cl}$  nanosheets [135]. (c) Schematic illustration of the separation and migration of carries in the bulk of the pure and C-doped  $\text{Bi}_3\text{O}_4\text{Cl}$  [136].

$\text{BiOIO}_3$  nanoplates. In addition, several reports have proven the positive role of the internal polar field of  $\text{BiOIO}_3$  in photocatalysis [142].

$\text{Bi}_2\text{O}_2[\text{BO}_2(\text{OH})]$  nanosheets with an internal polar field, which could be constructed by the ordered arrangement of  $\text{BO}_2(\text{OH})$  pyramids, were reported by Zhang et al. [143]. With the ordered arrangement of  $\text{BO}_2(\text{OH})$  pyramids in crystal structures, the direction of the internal polar electric field was confirmed to be along the  $ac$  plane. Under the action of the internal polar electric field, the photogenerated electrons and holes mainly move to the  $\text{Bi}_2\text{O}_2$  and  $\text{BO}_2(\text{OH})$  layers, respectively, resulting in the improvement of the photocatalytic efficiency of  $\text{Bi}_2\text{O}_2[\text{BO}_2(\text{OH})]$  under UV light irradiation.

Sillén/Aurivillius-structured  $\text{Bi}_4\text{NbO}_8\text{X}$  ( $\text{X} = \text{Cl}, \text{Br}$ ) is composed of

single-layered  $\text{NbO}_6$  octahedron slices and  $(\text{Bi}_2\text{O}_2)_2\text{X}$  blocks (Fig. 13c). Given their noncentrosymmetric structure with intense light absorption in the visible region, Hu et al. prepared  $\text{Bi}_4\text{NbO}_8\text{X}$  ( $\text{X} = \text{Cl}, \text{Br}$ ) single crystalline nanoplates by a flux method and reported their excellent piezo-photocatalytic performance [144]. The piezoelectric coefficients ( $d_{33}$ ) of  $\text{Bi}_4\text{NbO}_8\text{Cl}$  and  $\text{Bi}_4\text{NbO}_8\text{Br}$  were obtained by PFM for the first time, which were approximately 128 and 214 pm/V, respectively (Fig. 13d). Under the co-irradiation of light and ultrasound,  $\text{Bi}_4\text{NbO}_8\text{Br}$  exhibits the highest ORR activity, exceeding the sum of the light and ultrasound independently (Fig. 13e). In addition to its band bending and reductive reactive site enrichment, the significantly enhanced piezo-photocatalytic activity was also attributed to the effective

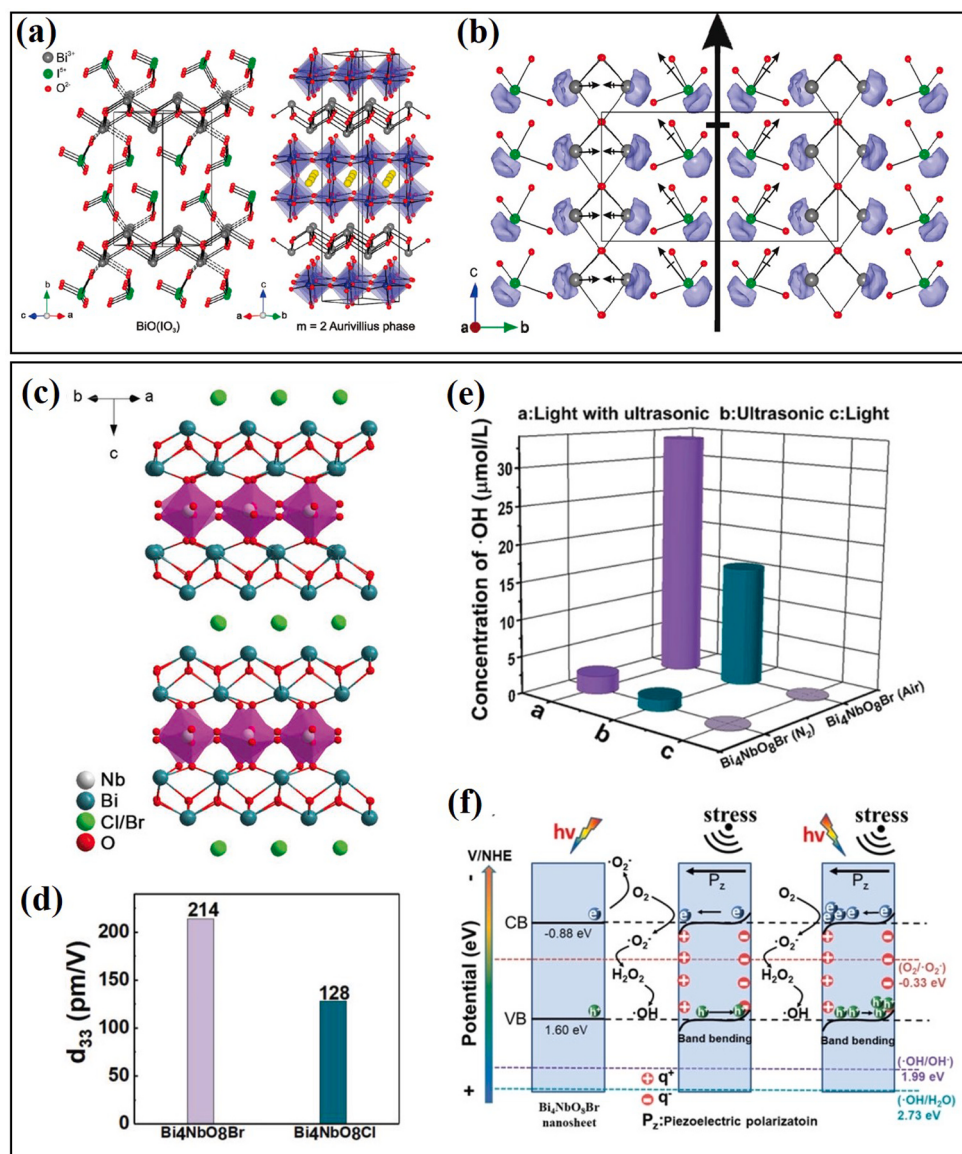


**Fig. 13.** (a) Crystal structure of  $\text{BiO}(\text{IO}_3)$ . (b) Net macroscopic polarization direction towards the  $c$ -axis (a large black arrow) [139]. (c) Crystal structure of  $\text{Bi}_4\text{NbO}_8\text{X}$  ( $\text{X} = \text{Cl}, \text{Br}$ ). (d) The piezoelectric coefficient ( $d_{33}$ ) of  $\text{Bi}_4\text{NbO}_8\text{Cl}$  and  $\text{Bi}_4\text{NbO}_8\text{Br}$  nanoplates. (e) Concentration of  $\cdot\text{OH}$  over  $\text{Bi}_4\text{NbO}_8\text{Br}$ . (f) Diagram of band bending of  $\text{Bi}_4\text{NbO}_8\text{Br}$  under different conditions [144].

separation of charges by the polarized electric field (Fig. 13f).

#### 4. Wurtzite-based piezoelectric semiconductors

##### 4.1. Structure and verification of piezoelectricity

The traditional piezoelectric effect mainly exists in perovskite materials such as  $\text{BaTiO}_3$  and  $\text{Pb}(\text{Zr}_{1-x}\text{Ti}_x)\text{O}_3$ . However, these materials do not have semiconductor properties, which limits their application in optoelectronic devices. Most semiconductors with wurtzite structures, such as  $\text{ZnO}$ ,  $\text{GaN}$ ,  $\text{InN}$ ,  $\text{CdS}$ ,  $\text{CdSe}$ , lack symmetry in certain specific directions and therefore exhibit piezoelectric effects [145]. By utilizing wurtzite-based semiconductor materials with both piezoelectric and semiconductor properties, coupled with optoelectronic excitation processes, many unprecedented properties may be derived in piezocatalysis and piezo-photocatalysis. Currently,  $\text{ZnO}$  is the most widely studied wurtzite-type piezocatalytic semiconductor. In the past decade, dozens of published papers have been reported, involving structure, preparation, piezocatalytic and piezo-photocatalytic applications, and

improvement strategies [36,146–148]. However,  $\text{CdS}$ ,  $\text{ZnS}$ , etc., are relatively few reported in the field of piezocatalysis and piezo-photocatalysis compared to  $\text{ZnO}$ . Therefore, we will focus on other wurtzite-based piezoelectric semiconductors that have applications in the field of piezocatalysis and piezo-photocatalysis except  $\text{ZnO}$ .

Sensitive piezoelectricity was observed in  $\text{ZnS}$  with wurtzite structure.  $\text{Zn}^{2+}$  cations and  $\text{S}^{2-}$  anions are tetrahedrally coordinated and the centers of the positive and negative charges of each tetrahedron coincide, as shown in Fig. 14a. When stress is applied, the centers of cations and anions undergo relative displacement, resulting in dipole moments (Fig. 14b). The superposition of all individual unit cell dipole moments forms the macroscopic polarization along the  $c$ -axis [149].  $\text{CdS}$  is one of the most promising materials in the field of visible-light-driven photocatalytic  $\text{H}_2$  evolution. In addition to excellent photocatalytic performance, wurtzite  $\text{CdS}$  with an asymmetric crystal structure also exhibits significant piezoelectric properties. As early as 2008, Zhonglin Wang team had already prepared a single  $\text{CdS}$  nanowire nanogenerator by using the triple coupling between semiconductor, piezoelectric, and optoelectronic properties [150].

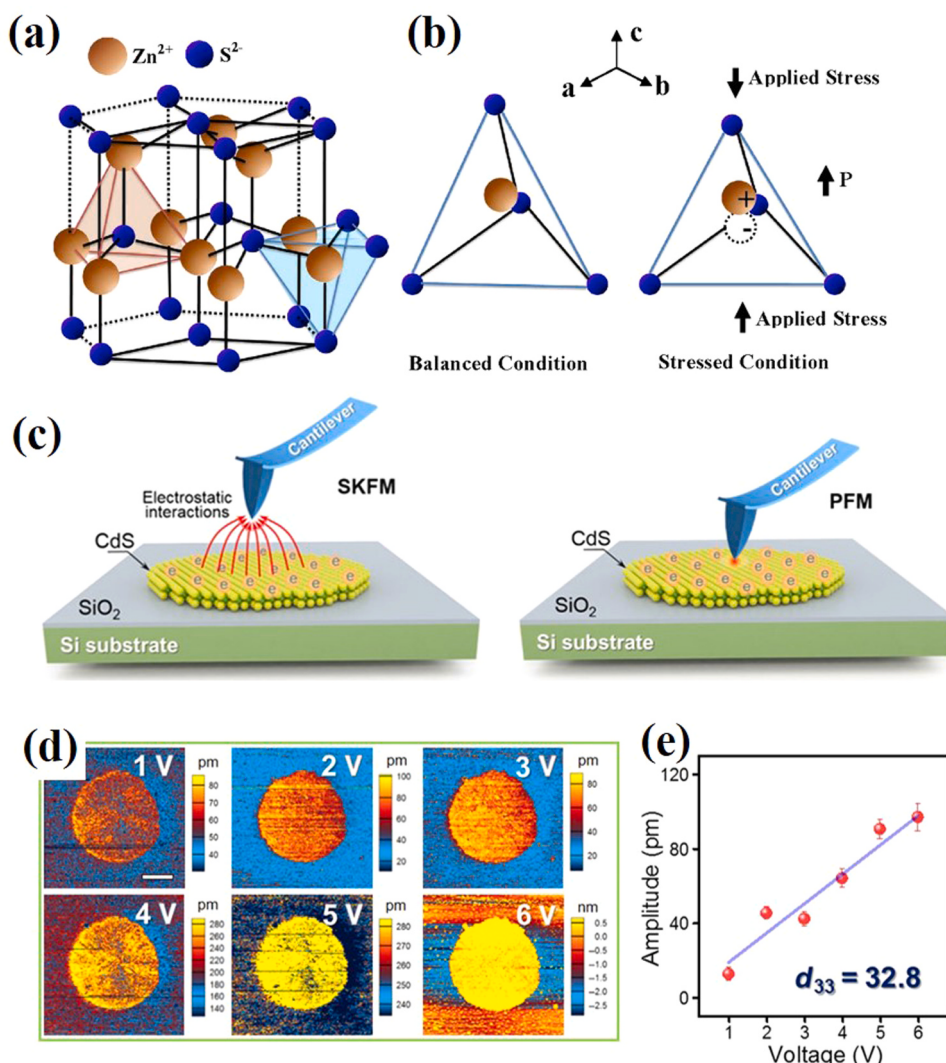


**Fig. 14.** (a) Crystallographic structure of wurtzite ZnS. (b) Schematics of the piezoelectric effect [149]. (c) Schematic illustration of SKFM and PFM measurements. (d) Amplitude images observed by contact PFM technology. (e) The measured vertical piezoelectric coefficient  $d_{33}$  is  $\sim 32.8 \text{ pm}\cdot\text{V}^{-1}$  [151].

Driven by the development of advanced testing instruments, Wang et al. demonstrated vertical piezoelectricity of CdS ultrathin films by single and dual ac resonance tracking piezoelectric force microscopy (DART-PFM) and scanning Kelvin force microscopy (SKFM), as shown in Fig. 14c [151]. CdS thin films down to 2–3 nm were synthesized by chemical vapor deposition to avoid the potential impact of residual organic molecules on the surface of wet-chemically synthesized CdS on its piezoelectricity. The vertical piezoelectric coefficient of CdS ultrathin films is  $\sim 32.8 \text{ pm}\cdot\text{V}^{-1}$ , which is three times that of the CdS bulk, demonstrating their strong vertical piezoelectricity at the atomic scale (Fig. 14d and e).

#### 4.2. Applications in piezocatalysis and piezo-photocatalysis

Atomically thin wurtzite ZnS NSs were first synthesized in room temperature by Feng et al. and used as a piezocatalyst in piezocatalytic H<sub>2</sub> evolution for the first time [26]. Benefited from the high  $d_{33}$  (18 pC/N) and unique ultra-thin structure (2 nm), ZnS NSs exhibited excellent piezoelectric catalytic performance, with an H<sub>2</sub> evolution rate of up to  $1.08 \mu\text{mol h}^{-1} \text{mg}^{-1}$  under ultrasonic treatment at a frequency of 27 kHz. Pan et al. prepared the hollow structural H-ZnS@SNG, which was fabricated by in-situ growth of hollow ZnS on graphene, and examined by the degradation of MB [152]. Compared with the pure H-ZnS (~58.4%) and solid ZnS@SNG (~89.8%), the H-ZnS@SNG

exhibited superior piezocatalytic properties for dye degradation (~100% in 10 min), which ascribed to the strain-induced polarization and the unique hollow structure accelerating the electron transfer. In addition, the heterostructured piezo-photocatalysts coupled with bifunctional ZnS nanoparticles and 2D g-C<sub>3</sub>N<sub>4</sub> nanosheets have also been applied to reduce CO<sub>2</sub> to CH<sub>4</sub>, as shown in Fig. 15 [153]. Under concurrent vibration and visible-light irradiation, a polarization electric field created along the direction of spontaneous polarization of ZnS nanoparticles could drive the separation of photocarriers from g-C<sub>3</sub>N<sub>4</sub>, thus improving the piezo-photocatalytic CO<sub>2</sub> reduction performance.

Considering the intrinsic polarity of wurtzite CdS, Zhang et al. proposed that aggravating structure distortion may enhance the macroscopic polarization of wurtzite CdS [28]. The CdS phase junction (H/C-CdS) between hexagonal CdS (H-CdS) and cubic CdS (C-CdS) is constructed by a solvothermal method and utilized for piezo-photocatalytic H<sub>2</sub> evolution in pure water. Piezo-photocatalytic H<sub>2</sub> evolution rate of  $3.19 \text{ mmol}\cdot\text{g}^{-1}\cdot\text{h}^{-1}$  of H/C-CdS is 1.4 and 5.3 times higher than those of H-CdS ( $2.31 \text{ mmol}\cdot\text{g}^{-1}\cdot\text{h}^{-1}$ ) and C-CdS ( $0.59 \text{ mmol}\cdot\text{g}^{-1}\cdot\text{h}^{-1}$ ), respectively, signifying the enhanced macroscopic polarization in H/C-CdS induces higher charge separation efficiency. Cd<sub>0.5</sub>Zn<sub>0.5</sub>S nano-branches were synthesized and used for H<sub>2</sub>O<sub>2</sub> evolution [154]. Under ultrasonic vibration, the H<sub>2</sub>O<sub>2</sub> yield of Cd<sub>0.5</sub>Zn<sub>0.5</sub>S is all higher than that of the original ZnS and CdS under ultrasonic vibration, indicating that the dendritic structure and the high

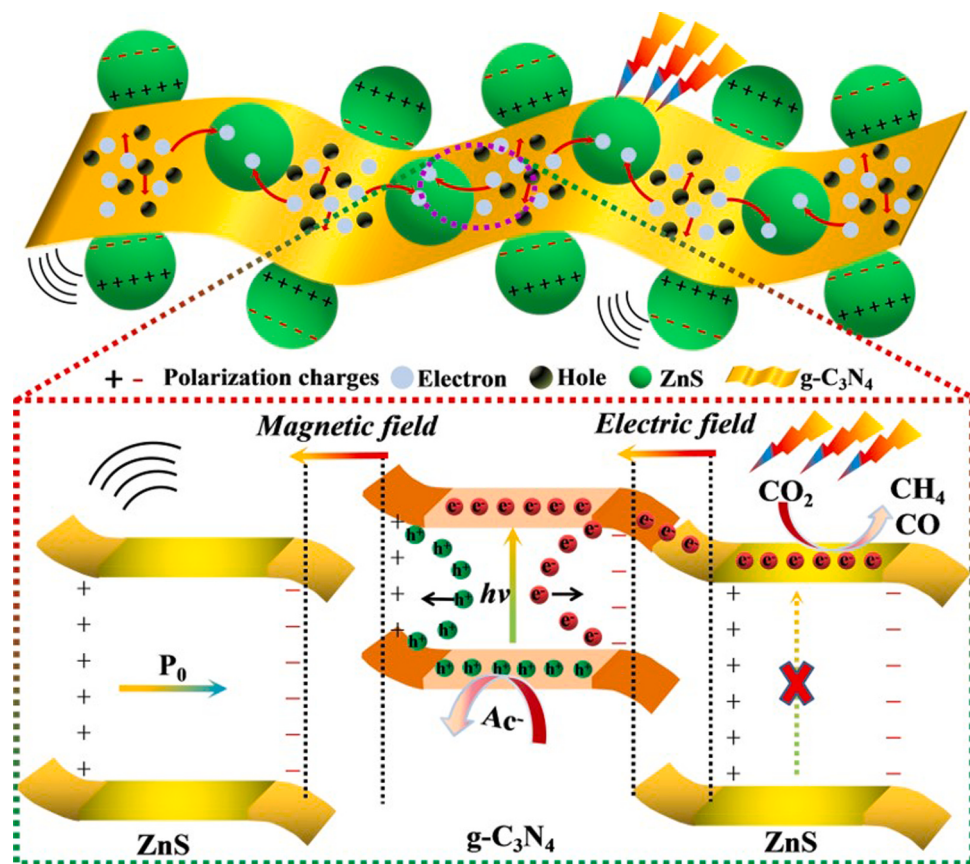


**Fig. 15.** Diagrammatic sketch of the piezo-photocatalytic mechanism of the ZnS/g-C<sub>3</sub>N<sub>4</sub> heterojunction [153].

piezoelectric coefficient are conducive to capturing and converting mechanical energy. Moreover, many heterostructure complex, such as BiFeO<sub>3</sub>@CdS [155], CdS/BiOCl [156], CdS@SnS<sub>2</sub> [157], have also been widely used in piezocatalysis and piezo-photocatalysis. So far, all wurtzite-based piezoelectric semiconductors used in applications of piezocatalysis and piezo-photocatalysis have been summarized in Table 1.

In addition, many strategies such as introducing residual stress through phase change stress engineering [158] and constructing surface S vacancies [159] can be used to improve the piezoelectric-photoelectrochemical (Piezo-PEC) performance of CdS. Up to now, except for ZnO, ZnS and CdS, other piezoelectric semiconductors

have not been reported in the application of piezocatalysis and piezo-photocatalysis. It is very worth looking forward to developing more piezoelectric semiconductors in the field of piezocatalysis and piezo-photocatalysis.

## 5. 2D carbon material-based piezocatalysts

As piezoelectric properties exist in the interior of non-centrosymmetric materials, some 2D carbon materials with centrosymmetry can be changed into an asymmetric structure with piezoelectricity by means of surface or structural modification, for instance, the introduction of adatoms and defects. Typically, Gr is

**Table 1**  
Summary of applications of wurtzite-based semiconductors in piezocatalysis and piezo-photocatalysis.

Type	Catalysts	Reaction conditions	Applications	Catalytic activity	Ref.
Piezo	ZnS nanosheets	Ultrasonic (27 kHz, 150 W)	H <sub>2</sub> evolution	1.08 μmol·h <sup>-1</sup> ·mg <sup>-1</sup>	[26]
Piezo	H-ZnS@SNG	Ultrasonic (40 kHz, 200 W)	Degradation of MB	~100% in 10 min	[152]
Piezo-photo	ZnS/g-C <sub>3</sub> N <sub>4</sub>	A 300 W Xe lamp (with a 420 nm cutoff filter) + magnetic field induced vibration	Reduction of CO <sub>2</sub> to CH <sub>4</sub>	1.099 μmol·g <sup>-1</sup> ·h <sup>-1</sup>	[153]
Piezo-photo	H/C-CdS	Ultrasonic (40 kHz, 200 W) + a LED lamp, (5 mW/cm <sup>2</sup> )	H <sub>2</sub> evolution	3.19 mmol·g <sup>-1</sup> ·h <sup>-1</sup>	[28]
Piezo-photo	CdS nanorod arrays	Ultrasonic (27 kHz, 100 W) + a 300 W Xe lamp (with a 420 nm cutoff filter)	H <sub>2</sub> evolution	20 μL·h <sup>-1</sup>	[160]
Piezo-photo	CdS nanosheets	Ultrasonic (50 kHz, 100 W) + a 300 W Xe lamp (with a 420 nm cutoff filter)	H <sub>2</sub> evolution	633 μL·h <sup>-1</sup>	[161]
Piezo-photo	CdS nanosheets	Ultrasonic (45 kHz, 100 W) + a lamp with a UV cut-off filter ( $\lambda \geq 420$ nm)	H <sub>2</sub> evolution	1293.62 μmol·g <sup>-1</sup> ·h <sup>-1</sup>	[162]
Piezo	CdS nanorods	Ultrasonic (40 kHz, 150 W)	H <sub>2</sub> evolution	157 μmol·g <sup>-1</sup> ·h <sup>-1</sup>	[163]
Piezo	Cd <sub>0.5</sub> Zn <sub>0.5</sub> S nano-branches	Ultrasonic (40 kHz, 120 W)	H <sub>2</sub> O <sub>2</sub> evolution	21.9 μmol g <sup>-1</sup> ·h <sup>-1</sup>	[154]
Piezo	BiFeO <sub>3</sub> @CdS	Ultrasonic (40 kHz, 300 W)	Degradation of BPA	99.7% in 60 min	[155]
Piezo	CdS/BiOCl	Ultrasonic (120 W)	H <sub>2</sub> evolution	1048.2 μmol g <sup>-1</sup> ·h <sup>-1</sup>	[156]
Piezo	CdS@SnS <sub>2</sub>	Ultrasonic (40 kHz, 180 W)	H <sub>2</sub> evolution	452.6 μmol ·g <sup>-1</sup> ·h <sup>-1</sup>	[157]

intrinsically nonpiezoelectric because both atoms in the planar hexagonal unit cell are identical. However, some theoretical predictions were published, which provided the expected values of piezoelectric coefficients by destroying the centrosymmetric structure of Gr, including the adsorption of foreign atoms, or incorporating noncentrosymmetric in-plane defects [164,165].

### 5.1. Graphene

Rodrigues et al. observed a strong piezoresponse of single-layered Gr deposited on a Si/SiO<sub>2</sub> calibration grating substrate (Fig. 16a) [166]. The piezoelectric effect of the entire structure (supported+suspended Gr) was measured by PFM. The signal of the negative piezoresponse on the supported Gr was four times higher than that on the suspended Gr caused by the chemical interaction of Gr's C atoms with the O atoms from the underlying SiO<sub>2</sub>, which induces a nonzero net dipole moment and polarization (Fig. 16b). Feng et al. selected N-doped Gr (NG) as an ultrathin piezoelectric material, compounded it with MoC quantum dots (QDs) to obtain MoC@NG assembled nanosheets, and applied them in piezocatalytic H<sub>2</sub> production from pure water [167]. Graphitic N, pyridinic, and pyrrolic N can be obtained according to the position of N doping (Fig. 16c). N doping (especially pyridinic N and pyrrolic N) causes a distinct charge redistribution and a high density of dipoles due to the high electronegativity of N. When mechanical vibration acts on the composite, the ultrathin NG layers can provide piezoelectric potential to trigger the HER on the MoC QDs (Fig. 16d). However, only weak piezoelectricity was observed, a phenomenon caused by the small

electronegativity difference between N and C atoms in NG. Hu et al. improved the piezocatalytic performance by increasing the asymmetry of the materials, particularly by introducing confined single-atom Zn to modulate the atomic local dipole to form 2D Gr confining Zn-N<sub>x</sub> polar centers (ZnNG) [168]. The greater the difference in electronegativity between Zn and N atoms and the longer the bond length of Zn-N would induce a greater local dipole moment, thus enhancing the piezoelectricity.

### 5.2. Carbon nitride

In addition to Gr, the graphitic form of carbon nitride (g-C<sub>3</sub>N<sub>4</sub>), as an analog of Gr, also has piezoelectric properties according to Zelisko et al. [169]. The relatively stable structure of g-C<sub>3</sub>N<sub>4</sub> is the tri-s-triazine repetition with uniformly distributed noncentrosymmetric triangular holes (Fig. 16e), which results in piezoelectricity in the tri-s-triazine plane and strong flexoelectricity—a material property that arises from the energy cost of creating internal polarizations in the presence of strain gradients. FEM simulation for the stress distribution in tri-s-triazine sheets of g-C<sub>3</sub>N<sub>4</sub> clearly showed that regardless of the sheet being a defect-free nonpiezoelectric sheet (Fig. 16f) or a sheet having circular holes (Fig. 16g), both net piezoelectric responses would be zero under uniform stretching because of their structural symmetry. The triangular nanopores generated a net piezoelectric response, which allowed a nonzero net average polarization under the action of a mechanical stretch (or compression) attributable to the flexoelectric effect (Fig. 16h) [170]. Interestingly, the piezoelectricity was still retained in the bulk

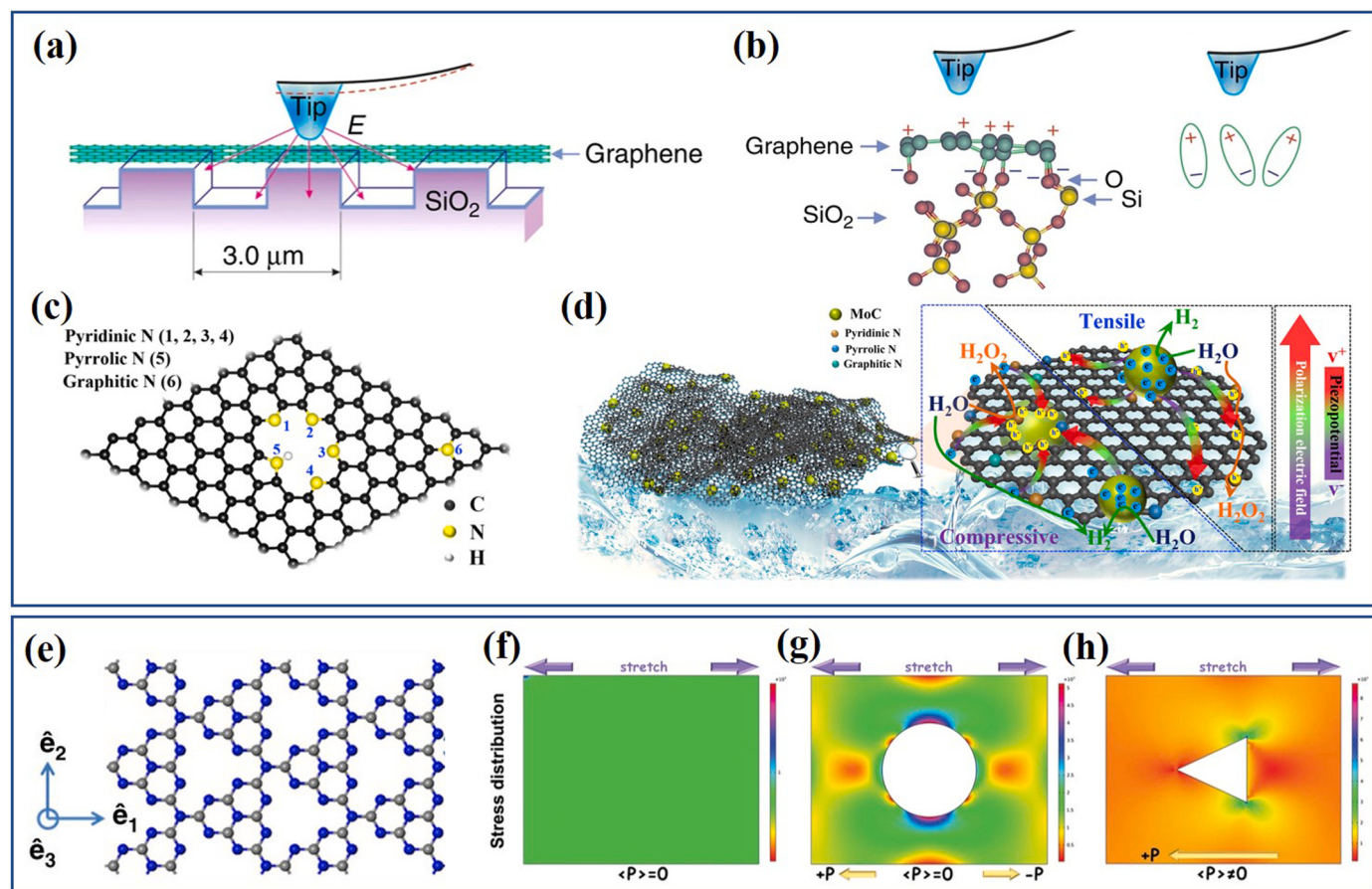


**Fig. 16.** (a) Schematic of the PFM measurements on single-layer Gr adsorbed on the SiO<sub>2</sub> substrate and their cross-section of the piezoresponse. (b) Schematic diagram of dipole surface states induced by chemical interactions between carbon and oxygen atoms [166]. (c) Schematic representations of N-doped Gr including graphitic N, pyridinic and pyrrolic N. (d) Schematic diagram of mechanism for piezocatalytic H<sub>2</sub> production over MoC@NG [167]. (e) Structural diagram of single-sheet tri-s-triazine g-C<sub>3</sub>N<sub>4</sub> [169]. FEM simulation for the stress distribution of g-C<sub>3</sub>N<sub>4</sub> sheets with the defect-free plane (f), circular pore (g), and triangular pore (h) [170].

phase of g-C<sub>3</sub>N<sub>4</sub> because of the distinctive atomic stacking structure, which was the opposite for 2D TMDCs.

g-C<sub>3</sub>N<sub>4</sub> has also been applied for piezo-photocatalytic H<sub>2</sub> production. Hu et al. prepared g-C<sub>3</sub>N<sub>4</sub> with an atomically thin sheet-like structure and reported a superb H<sub>2</sub> evolution rate of 12.16 mmol·g<sup>-1</sup>·h<sup>-1</sup> without any loaded cocatalysts owing to their preferable piezoelectricity, which was derived from the in-plane polarization induced by the additive dipole moment of polar tri-s-triazine units [170]. Furthermore, the formation of a homojunction between pyromellitic diimide with an aromatic plane and g-C<sub>3</sub>N<sub>4</sub> with triazine rings can induce  $\pi$ - $\pi$  interactions to promote electron migration and twist the g-C<sub>3</sub>N<sub>4</sub> plane into a more polar porous structure with enhanced piezoelectricity, which leads to the improvement of piezocatalytic performance and the acceleration of charge transfer [171]. The applications of Gr and g-C<sub>3</sub>N<sub>4</sub> in piezocatalysis and piezo-photocatalysis that have been published in recent years are compared and summarized in Table 2.

## 6. Metal-organic framework-based piezocatalysts

Metal-organic frameworks (MOFs) are an emerging class of porous materials constructed from metal-containing nodes and organic linkers. Given their structural and functional tunability, MOFs have emerged as compelling and functional meso-/microporous materials for diverse applications over the past few decades. The highly porous structure and structural tailorability of MOFs, coupled with their low cost and availability for mass production, have provided many opportunities for their application in various fields [177–179]. As Garcia et al. used MOF-5 as a semiconductor to degrade phenol in water under UV light irradiation for the first time in 2006, various MOFs have been studied and applied to photocatalytic systems [180]. Interestingly, the piezoelectric properties of MOF (UiO-66) have also recently been reported, eventually contributing to their increased popularity in the field of piezocatalysis. Fig. 17a shows the relevant MOF chronology of discovery and progress [181].

### 6.1. Verification of piezoelectricity

UiO-66, the prototype of zirconium-based MOFs, has long been thought to be a highly centrosymmetric structure [*Fm3<sup>-</sup>m* (225)] by powder X-ray diffraction measurement. In 2019, Sun et al. observed a lower crystalline symmetry caused by the consistency of missing ligands and clusters via dual AC resonance tracking (DART)-PFM and piezoresponse force spectroscopy, verifying the nanoscale piezo/ferroelectric active behavior in both UiO-66(Hf/Zr) MOFs [182]. The polarization behavior of UiO-66(Hf) and UiO-66(Zr) MOFs was found by comparing the total polarization changes ( $\Delta P$ ) of the four constituent atoms, including C, H, O, and metals (Hf/Zr) (Fig. 17b). Furthermore,

experimental observations and first-principles calculations both confirm the stronger piezo/ferroelectric responses of UiO-66(Hf)-type MOF nanocrystals than UiO-66(Zr)-type MOFs. These unexpected results revealed the underlying polarization mechanism of the MOF and provided theoretical support and potential applications in piezocatalysis.

### 6.2. Applications in piezocatalysis and piezo-photocatalysis

Zhang et al. investigated the piezo-photocatalysis of isostructural Zr- and Hf-based MOFs, i.e., UiO-66-NH<sub>2</sub>(Zr) and UiO-66-NH<sub>2</sub>(Hf), with similar physical and chemical properties but distinctly different piezoelectric properties [183]. Both MOFs present negligible activity differences in photocatalytic H<sub>2</sub> production, whereas UiO-66-NH<sub>2</sub>(Hf) exhibits 2.2 times higher piezo-photocatalytic activity than UiO-66-NH<sub>2</sub>(Zr) owing to the stronger piezoelectric effect of UiO-66-NH<sub>2</sub>(Hf) when additional ultrasonic irradiation was added. (Fig. 17c). The results of PFM also clarify that Hf-MOF has a much higher piezoelectric response than Zr-MOF, which can be attributed to the larger polarity of the Hf-O bond than the Zr-O bond (Fig. 17d). Ultrasonic irradiation can not only provide mechanical stress for piezocatalysts but also accelerate the mass transfer during the reaction. In the abovementioned study of the author, both MOFs show highly similar physical and chemical properties, and the mass transfer contribution to the activity should be approximate. Therefore, the higher activity of UiO-66-NH<sub>2</sub>(Hf) should be attributed to the sole factor of the larger piezoelectric effect of the Hf-MOF, which can distinguish the effect of accelerated mass transfer, and the piezoelectric effect on the enhancement of photocatalytic activity.

When the polar molecule adenine was introduced as a linking agent in the synthesis process of Zr-based UiO-66 (denoted as AD-U), the AD-U exhibited significantly enhanced piezocatalytic activity and higher charge separation efficiency than UiO-66 owing to its enhanced piezoelectric potential resulting from the increase in structural asymmetry [184]. Subsequently, piezocatalytic activity was observed in bismuth-based MOFs with two different morphologies, namely, FCAU-17 (flakes) and CAU-17 (rods) [185]. Rod-like CAU-17 shows more effective piezocatalytic activity owing to its far stronger piezoelectric response as a result of its easily deformed nature.

## 7. Others

According to some reports, hundreds of materials have lost their inversion symmetry and become piezoelectric in the single-layered form, but they are not piezoelectric in the bulk form [57]. This study is limited to summarizing some novel piezoelectric materials that have been used in piezocatalysis or piezo-photocatalysis, such as organolead

**Table 2**  
Summary of applications of graphene and carbon nitride in piezocatalysis and piezo-photocatalysis.

Type	Catalysts	Reaction conditions	Applications	Catalytic activity	Ref.
g-C <sub>3</sub> N <sub>4</sub> -based	Piezo	MoC@NG assembled nanosheet	Ultrasonic (40 kHz, 100 W)	H <sub>2</sub> evolution	1.690 $\mu\text{mol}\cdot\text{h}^{-1}$ $\text{mg}^{-1}$ [167]
	Piezo	Ultrathin graphene confining Zn-N-C dipoles	Magnetic stirring (2500 r min <sup>-1</sup> )	H <sub>2</sub> evolution	14.65 $\mu\text{mol}\cdot\text{g}^{-1}\cdot\text{h}^{-1}$ [168]
	Piezophoto	Ultrathin g-C <sub>3</sub> N <sub>4</sub>	Ultrasonic (40 kHz, 240 W), visible light ( $\lambda \geq 420$ nm)	H <sub>2</sub> evolution	12.16 mmol·g <sup>-1</sup> ·h <sup>-1</sup> [170]
	Piezophoto	g-C <sub>3</sub> N <sub>4</sub> /PDI-g-C <sub>3</sub> N <sub>4</sub> homojunction	Ultrasonic (40 kHz, 200 W) + Xe lamp (300 W, 420 nm cutoff filter)	Degradation of atrazine	94% in 60 min [171]
	Piezophoto	g-C <sub>3</sub> N <sub>4</sub> with C and N vacancies	Ultrasonic (53 kHz, 150 W)	H <sub>2</sub> O <sub>2</sub> generation	34 $\mu\text{mol}\cdot\text{h}^{-1}$ [172]
	Piezophoto	2D ultrathin g-C <sub>3</sub> N <sub>4</sub>	Ultrasonic (40 kHz, 120 W) + Xe lamp (300 W, 420 nm cutoff filter)	Degradation of 2,4-dichlorophenol	6.65 $\times 10^{-2}$ min <sup>-1</sup> [173]
	Piezophoto	g-C <sub>3</sub> N <sub>4</sub> with N vacancies	Ultrasonic + Xe lamp (300 W, 420 nm cutoff filter)	Degradation of RhB	100% in 60 min [174]
	Piezophoto	Fluorination-defluorination treatment of CNs (d-FCNs)	Ultrasonic (40 kHz) + visible-light irradiation ( $\lambda > 420$ nm)	H <sub>2</sub> evolution	13.53 mmol·g <sup>-1</sup> ·h <sup>-1</sup> [175]
Piezo	Sulfur doped graphdiyne (SGDY) nanosheets	Ultrasonic (800 W)	Degradation of RhB (10 mg/L, pH = 4.0)	60.23 min <sup>-1</sup> [176]	

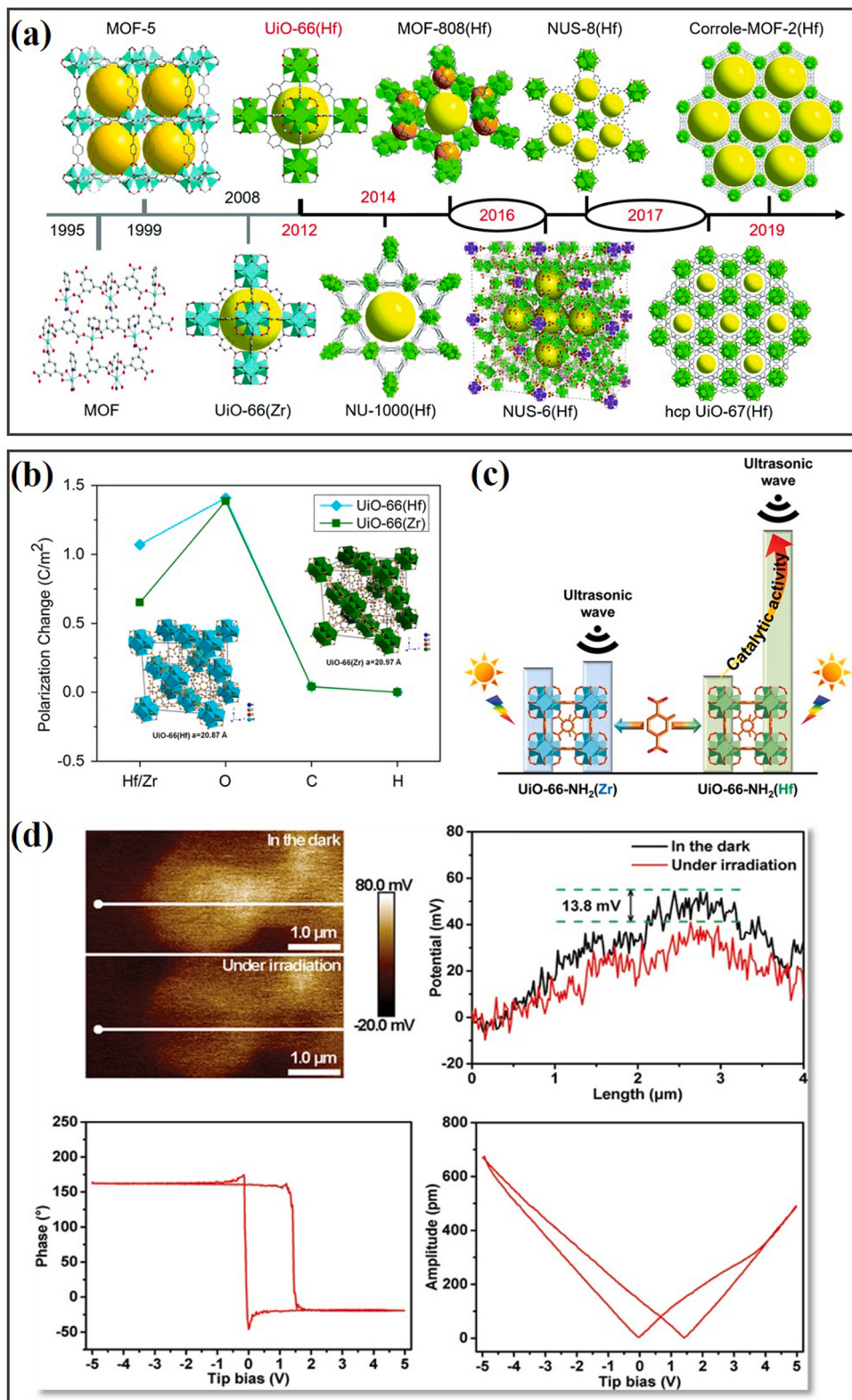


**Fig. 17.** (a) Chronology of advances in the discovery of Hf-MOFs [181]. (b) Polarization changes  $\Delta P$  of the four atoms of  $\text{UiO-66(Zr)}$  and  $\text{UiO-66(Hf)}$  [182]. (c) Schematic  $\text{H}_2$  production activities of  $\text{UiO-66-NH}_2(\text{Zr})$  and  $\text{UiO-66-NH}_2(\text{Hf})$  in photocatalysis and piezo-photocatalysis. (d) Piezoelectric performance by PFM measurements [183].

halide perovskite  $\text{CH}_3\text{NH}_3\text{PbI}_3$  ( $\text{MAPbI}_3$ ) [186], ferroelastic  $\text{BiVO}_4$  with a domain structure [187–191], antimony sulfo-iodide ( $\text{SbSI}$ ) [192], monoclinic dibismuth tetroxide ( $m\text{-Bi}_2\text{O}_4$ ) [193], and  $\text{Ca}_{10}(\text{PO}_4)_6(\text{OH})_2$  (HAP) [194]. Table 3 summarizes the applications of these piezoelectric

materials in piezocatalysis or piezo-photocatalysis.

**Table 3**

Summary of applications of other piezoelectric materials in piezocatalysis and piezo-photocatalysis.

Type	Catalysts	Reaction conditions	Applications	Catalytic activity	Ref.
Piezo-photo	CH <sub>3</sub> NH <sub>3</sub> PbI <sub>3</sub> (MAPbI <sub>3</sub> )	Ultrasonic (50–90 W) + a tungsten-halogen lamp (500 W)	H <sub>2</sub> evolution	23.30 μmol·h <sup>-1</sup>	[186]
Piezo	Au/BiVO <sub>4</sub>	Ultrasonic (40 kHz, 120 W)	Degradation of 4-CP (0.1 mM) and Cr (VI) (10 mg/L)	91% and 83% in 120 min	[188]
Piezo	Fe/BiVO <sub>4</sub>	Ultrasonic (40 kHz, 120 W)	Degradation of p-CP	86% in 120 min	[189]
Piezo	V <sub>2</sub> O <sub>5</sub> /BiVO <sub>4</sub>	Ultrasonic (40 kHz, 70 W)	Degradation of MB	80% in 240 min	[190]
Piezo-photo	BiVO <sub>4</sub>	Ultrasonic cleaner (40 kHz, 70 W) + two Havells company (15 W) bulbs.	Degradation of MB	81% in 240 min	[191]
Piezo-photo	BiVO <sub>4</sub>	Ultrasonic (40 kHz, 100 W), visible light irradiation (Xe lamp with a filter cutoff 420 nm, 300 W)	Degradation of MB (3 mg/L)	0.081 min <sup>-1</sup>	[195]
Piezo-photo	Bi <sub>2</sub> VO <sub>5.5</sub>	Ultrasonic (40 kHz, 150 W) + two Havells company (15 W) bulbs	Degradation of MB (5 mg/L)	~82% in 240 min	[196]
Piezo	SbSI nanowires	Ultrasonic (20 kHz, 750 W)	Degradation of MB (30 mg/L)	99.5% in 40 S	[192]
Piezo-photo	SbSI	Ultrasonic (40 kHz, 180 W) + a 400 W metal halide lamp	Degradation of MB (30 mg/L)	1.77 min <sup>-1</sup>	[197]
Piezo	m-Bi <sub>2</sub> O <sub>4</sub>	Ultrasonic (40 kHz, 300 W)	Degradation of SM (10 mg/L)	0.033 min <sup>-1</sup>	[193]
Piezo	Ca <sub>10</sub> (PO <sub>4</sub> ) <sub>6</sub> (OH) <sub>2</sub> (HAP)	Ultrasonic (53 kHz, 250 W)	Methane/methanol conversion	84.4 μmol·g <sup>-1</sup> ·h <sup>-1</sup>	[194]
Piezo	Pt/HAP	Ultrasonic (20 kHz, 400 W)	Oxidation HMF to FFCA	96% conversion and 70% FFCA yield in 120 min	[198]
Piezo	HAP	Ultrasonic (40 kHz, 300 W)	Degradation of RhB (5 mg/L)	92% in 30 min	[199]
Piezo	Oxygen vacancy-induced HAP	Ultrasonic (45 kHz, 600 W)	Degradation of BPA (15 ppm)	98.43% in 12 min	[200]
Piezo	K <sub>2</sub> Ti <sub>6</sub> O <sub>13</sub> /TiO <sub>2</sub>	Ultrasonic (40 kHz, 120 W)	Degradation of tetracycline (50 ppm)	60% in 120 min	[201]
Piezo-photo	CuBi <sub>2</sub> O <sub>4</sub>	Ultrasonic (40 kHz, 300 W) + Xe lamp (300 W, 420 nm cutoff filter)	Degradation of RhB (5 mg/L)	0.0478 min <sup>-1</sup>	[202]
Piezo	beta-BaTi <sub>2</sub> O <sub>5</sub> nanorods	Ultrasonic (40 kHz, 120 W)	Degradation of RhB (10 mg/L)	0.00372 min <sup>-1</sup>	[203]
Piezo-photo	La <sub>2</sub> NiO <sub>4</sub>	Ultrasonic (40 kHz, 100 W) + Xe lamp (300 W, 1000 mW cm)	H <sub>2</sub> evolution	1097 μmol·h <sup>-1</sup> ·g <sup>-1</sup>	[204]
Piezo-photo	CaCu <sub>3</sub> Ti <sub>4</sub> O <sub>12</sub> ceramics	Ultrasonic (40 kHz, 70 W) + 30 W Havells LED	Degradation of MB (3 mg/L)	76% in 240 min	[205]
Piezo	Cu <sub>3</sub> B <sub>2</sub> O <sub>6</sub>	Ball mill (600 rpm)	Degradation of RhB (10 mg/L)	99.9% in 30 min	[206]
Piezo	Bi <sub>2</sub> Fe <sub>4</sub> O <sub>9</sub>	Ultrasonic (40 kHz, 200 W)	H <sub>2</sub> evolution (in 10% methanol)	5723 μmol·g <sup>-1</sup> ·h <sup>-1</sup>	[207]
Piezo	Cellulose nanocrystal (CNC)	Ultrasonic (40 kHz, 180 W)	Degradation of RhB (5 mg/L)	96.65% in 180 min	[208]
Piezo-photo	ZnAl layered double hydroxides (ZnAl-LDHs)	Ultrasonic (40 kHz, 100 W) + Xe lamp (300 W)	Degradation of carbamazepine (5 mg/L)	0.148 min <sup>-1</sup>	[209]

## 8. Summary and outlook

This review summarizes various novel piezocatalysts, including TMDCs, Aurivillius-type and Sillén-type bismuth layered structure materials, wurtzite-based piezoelectric semiconductors, Gr, g-C<sub>3</sub>N<sub>4</sub>, and MOFs, and their discovery, verification of piezoelectricity, performance improvement strategies, applications in piezocatalysis and piezo-photocatalysis. In the past decade, the vigorous development of new piezocatalytic materials has become a research hotspot in the field of piezocatalysis, attaining extensive achievements. Although excellent works on novel piezocatalytic materials have been published, research in this field is still in its infancy and needs further development. For instance, the preparation method of the novel piezocatalysts is relatively monotonous, mainly based on the hydrothermal method. There are no uniform standards for the dosage of catalysts, concentration of pollutant solution, ultrasonic power and frequency, making it difficult to compare the piezocatalytic performance horizontally. The catalytic mechanism is controversial [210]. And the application is mainly concentrated on H<sub>2</sub> evolution and organic pollutant degradation, while the applications of CO<sub>2</sub> reduction, N<sub>2</sub> fixation, and sterilization are very limited. This gap provides a huge space and a golden opportunity to enrich piezoelectric materials in the catalytic field. Furthermore, as some fundamental problems still exist in this research field, the following improvement strategies are proposed:

- 1) Most TMDCs exhibit piezoelectric properties only in single layers or a few odd-numbered layers, and their piezoelectric properties decrease sharply with an increasing number of layers. In fact, both odd- and even-numbered layers coexist in TMDCs. Furthermore, accurately controlling the number of monolayers and producing them on a large scale via current synthesis techniques, including hydrothermal methods, exfoliation, and CVD, are difficult to achieve. Therefore,

higher requirements are proposed for the current synthesis methods, especially for improving the yield of monolayer TMDCs.

- 2) Some centrosymmetric 2D carbon materials can be changed into an asymmetric structure with piezoelectricity by means of surface or structural modification. A good example is the introduction of adatoms and defects, such as Gr. If the research scope of carbon materials can be broadened, such as by modifying single-walled carbon nanotubes or fullerenes (vacancies, adatoms, and substitutional impurities), then 1D and 0D piezocatalysts with better performance may be obtained. Hence, understanding the role of defects, formulating effective defect engineering schemes, and rationally introducing defects are of great significance for the development of more novel catalysts.
- 3) Due to the relatively large specific surface area of 2D-TMDCs, Gr, g-C<sub>3</sub>N<sub>4</sub>, etc., they exhibit significant capabilities in the physical adsorption of organic dyes. Therefore, during the degradation process of organic dyes, it is necessary to consider the impact of the adsorption of dyes on piezocatalytic performance to avoid data distortion.
- 4) Currently, the main methods to confirm the piezoelectric properties of materials include PFM, SHG, and theoretical simulation. Although some of the reviewed articles do not comprehensively explain piezoelectric coefficients, past experiments have established that their piezocatalytic or piezo-photocatalytic properties can be improved under mechanical vibration. However, both ultrasonic vibration and mechanical stirring can also accelerate the mass transfer during the reaction process, and sonocatalysis induced by the ultrasonic cavitation effect can accelerate the overall catalytic activity. Performing piezoelectric tests and controlling the experimental variables must be performed to clarify the contribution of the piezoelectric effect on the promotion of catalytic activity.

- 5) In general, ultrasonic vibration with high frequency and high power is the most widely used mechanical excitation in piezocatalytic experiments. However, ultrasound is a sound wave vibration driven by electrical energy, which does not fully depict the mechanical energy in natural environmental conditions featuring low-frequency and low power, such as the vortex, falling, and ripples of water. Therefore, the development of novel piezocatalysts with high piezoelectric response to low-frequency mechanical energy is crucial for achieving their high catalytic performance. In piezocatalysis and piezophotocatalysis research, improving the piezoelectric coefficient, specific surface area, reactive active sites, and reusability of novel piezocatalysts is an effective strategy to promote their practical application.
- 6) In piezo-photocatalysis, catalytic performance is mainly improved by coupling piezoelectric materials and semiconductor photocatalysts, which means that these materials should have good piezoelectric properties and photocatalytic activity, respectively. Under long-term mechanical vibration, the binding ability of these two materials is gradually weakened, resulting in a significant reduction in cyclicity and stability. If the two functions of "semiconductor photocatalysis" and "piezoelectric polarization" can be coupled onto a single material, then the problem of poor stability of the composites can be avoided. All photocatalytic reactions occur on the surface; thus, the cyclicity and stability can be greatly enhanced by performing "semiconducting modification" on the surface shell of piezoelectric monomers, subsequently improving the photocatalytic activity.
- 7) In the piezo-photocatalytic hybrid system, the reasons for the improvement of catalytic performance in some studies are only attributed to the built-in electric field promoting the separation of photogenerated carriers. The synergistic effect between piezoelectric effect and semiconductor has not been fully analyzed. Many factors have not been considered, such as changes in band structure, piezoelectric coefficient, dielectric constant, conductivity, as well as interfacial charge transfer kinetics. Therefore, there are still many experimental studies and theoretical calculations that need to be carried out in order to design and develop excellent piezo-photocatalyst systems.

Overall, owing to the tireless efforts of scientists, a rich variety of novel piezoelectric materials with high catalytic efficiency and stability have been discovered. This review may serve as a useful reference for developing more novel materials with superior piezocatalytic or piezophotocatalytic performance in the future, further providing a better understanding of their mechanisms. This review may also inspire work in other related fields, such as piezoelectric sensors and actuators, eventually advancing the development of novel piezoelectric materials for sustainable science and their potential for practical applications. Exploring novel piezoelectric materials is important for enhancing the understanding of the mechanisms of piezocatalytic and piezophotocatalytic processes. This study is expected to contribute to the future development of more novel piezoelectric materials.

#### CRediT authorship contribution statement

Hongjuan Zheng performed investigation, conceptualization, and writing - original draft. Kongjun Zhu performed conceptualization, writing - review, and supervision. Yulong Wang performed writing – review & editing, Jinsong Liu performed writing – review & editing, Jing Wang performed writing – review & editing, Kang Yan performed writing – review & editing.

#### Declaration of Competing Interest

The authors declare that they have no known competing financial interests or personal relationships that could have appeared to influence the work reported in this paper.

#### Data availability

No data was used for the research described in the article.

#### Acknowledgements

This work was supported by the National Natural Science Foundation of China (NSFC No. U1904213 and 52202137), State Key Laboratory of Mechanics and Control of Mechanical Structures (Nanjing University of Aeronautics and Astronautics) (MCMS-E-0521G02), a Project Funded by the Priority Academic Program Development of Jiangsu Higher Education Institutions (PAPD), and Jiangsu Funding Program for Excellent Postdoctoral Talent.

#### References

- [1] A. Fujishima, K. Honda, Electrochemical photolysis of water at a semiconductor electrode, *Nature* 238 (1972) 37–38.
- [2] J. Schneider, M. Matsuoka, M. Takeuchi, J. Zhang, Y. Horiuchi, M. Anpo, D. W. Bahnemann, Understanding TiO<sub>2</sub> photocatalysis: mechanisms and materials, *Chem. Rev.* 114 (2014) 9919–9986.
- [3] W. Wang, M.O. Tadé, Z. Shao, Research progress of perovskite materials in photocatalysis- and photovoltaics-related energy conversion and environmental treatment, *Chem. Soc. Rev.* 44 (2015) 5371–5408.
- [4] M. Ge, J. Cai, J. Iocozzia, C. Cao, J. Huang, X. Zhang, J. Shen, S. Wang, S. Zhang, K.-Q. Zhang, Y. Lai, Z. Lin, A review of TiO<sub>2</sub> nanostructured catalysts for sustainable H<sub>2</sub> generation, *Int. J. Hydrog. Energy* 42 (2017) 8418–8449.
- [5] S. Tu, Y. Guo, Y. Zhang, C. Hu, T. Zhang, T. Ma, H. Huang, Piezocatalysis and piezo-photocatalysis: catalysts classification and modification strategy, reaction mechanism, and practical application, *Adv. Funct. Mater.* 30 (2020), 2005158.
- [6] W. Wang, J. Li, H. Liu, S. Ge, Advancing versatile ferroelectric materials toward biomedical applications, *Adv. Sci.* 8 (2021), 2003074.
- [7] S.K. Ray, J. Cho, J. Hur, A critical review on strategies for improving efficiency of BaTiO<sub>3</sub>-based photocatalysts for wastewater treatment, *J. Environ. Manag.* 290 (2021), 112679.
- [8] W. Zhang, Q. Feng, E. Hosono, D. Asakura, J. Miyawaki, Y. Harada, Tetragonal distortion of a BaTiO<sub>3</sub>/Bi<sub>0.5</sub>Na<sub>0.5</sub>TiO<sub>3</sub> nanocomposite responsible for anomalous piezoelectric and ferroelectric behaviors, *ACS Omega* 5 (2020) 22800–22807.
- [9] L. Lu, W. Ding, J. Liu, B. Yang, Flexible PVDF based piezoelectric nanogenerators, *Nano Energy* 78 (2020), 105251.
- [10] G. Kalimuldina, N. Turdakyn, I. Abay, A. Medeubayev, A. Nurpeissova, D. Adair, Z. Bakenov, A review of piezoelectric pvdf film by electrospinning and its applications, *Sensors* (2020).
- [11] L. Pan, S. Sun, Y. Chen, P. Wang, J. Wang, X. Zhang, J.-J. Zou, Z.L. Wang, Advances in piezo-phototronic effect enhanced photocatalysis and photoelectrocatalysis, *Adv. Energy Mater.* 10 (2020), 2000214.
- [12] J. Wu, N. Qin, D. Bao, Effective enhancement of piezocatalytic activity of BaTiO<sub>3</sub> nanowires under ultrasonic vibration, *Nano Energy* 45 (2018) 44–51.
- [13] J. Feng, Y. Fu, X. Liu, S. Tian, S. Lan, Y. Xiong, Significant improvement and mechanism of ultrasonic inactivation to escherichia coli with piezoelectric effect of hydrothermally synthesized t-BaTiO<sub>3</sub>, *ACS Sustain. Chem. Eng.* 6 (2018) 6032–6041.
- [14] J. Wu, Q. Xu, E. Lin, B. Yuan, N. Qin, S.K. Thatikonda, D. Bao, Insights into the role of ferroelectric polarization in piezocatalysis of nanocrystalline BaTiO<sub>3</sub>, *ACS Appl. Mater. Interfaces* 10 (2018) 17842–17849.
- [15] S. Kumar, M. Sharma, A. Kumar, S. Powar, R. Vaish, Rapid bacterial disinfection using low frequency piezocatalysis effect, *J. Ind. Eng. Chem.* 77 (2019) 355–364.
- [16] K.-S. Hong, H. Xu, H. Konishi, X. Li, Direct water splitting through vibrating piezoelectric microfibers in water, *J. Phys. Chem. Lett.* 1 (2010) 997–1002.
- [17] K.-S. Hong, H. Xu, H. Konishi, X. Li, Piezoelectrochemical effect: a new mechanism for azo dye decolorization in aqueous solution through vibrating piezoelectric microfibers, *J. Phys. Chem. C.* 116 (2012) 13045–13051.
- [18] M.B. Starr, X. Wang, Fundamental analysis of piezocatalysis process on the surfaces of strained piezoelectric materials, *Sci. Rep.* 3 (2013) 2160.
- [19] M.B. Starr, X. Wang, Coupling of piezoelectric effect with electrochemical processes, *Nano Energy* 14 (2015) 296–311.
- [20] J.M. Wu, W.E. Chang, Y.T. Chang, C.-K. Chang, Piezo-catalytic effect on the enhancement of the ultra-high degradation activity in the dark by single- and few-layers MoS<sub>2</sub> nanoflowers, *Adv. Mater.* 28 (2016) 3718–3725.
- [21] S. Singh, N. Khare, Coupling of piezoelectric, semiconducting and photoexcitation properties in NaNbO<sub>3</sub> nanostructures for controlling electrical transport: Realizing an efficient piezo-photoanode and piezo-photocatalyst, *Nano Energy* 38 (2017) 335–341.
- [22] B. Yuan, J. Wu, N. Qin, E. Lin, Z. Kang, D. Bao, Sm-doped Pb(Mg<sub>1/3</sub>Nb<sub>2/3</sub>)O<sub>3</sub>-xPbTiO<sub>3</sub> piezocatalyst: Exploring the relationship between piezoelectric property and piezocatalytic activity, *Appl. Mater. Today* 17 (2019) 183–192.
- [23] Y.-L. Liu, J.M. Wu, Synergistically catalytic activities of BiFeO<sub>3</sub>/TiO<sub>2</sub> core-shell nanocomposites for degradation of organic dye molecule through piezophototronic effect, *Nano Energy* 56 (2019) 74–81.

- [24] A. Biswas, S. Saha, N.R. Jana, ZnSnO<sub>3</sub> nanoparticle-based piezocatalysts for ultrasound-assisted degradation of organic pollutants, *ACS Appl. Nano Mater.* 2 (2019) 1120–1128.
- [25] J. Ma, J. Ren, Y. Jia, Z. Wu, L. Chen, N.O. Haugen, H. Huang, Y. Liu, High efficiency bi-harvesting light/vibration energy using piezoelectric zinc oxide nanorods for dye decomposition, *Nano Energy* 62 (2019) 376–383.
- [26] W. Feng, J. Yuan, L. Zhang, W. Hu, Z. Wu, X. Wang, X. Huang, P. Liu, S. Zhang, Atomically thin ZnS nanosheets: Facile synthesis and superior piezocatalytic H<sub>2</sub> production from pure H<sub>2</sub>O, *Appl. Catal. B Environ.* 277 (2020), 119250.
- [27] G. Singh, M. Sharma, R. Vaish, Exploring the piezocatalytic dye degradation capability of lithium niobate, *Adv. Powder Technol.* 31 (2020) 1771–1775.
- [28] M. Zhang, S. Nie, T. Cheng, Y. Feng, C. Zhang, L. Zheng, L. Wu, W. Hao, Y. Ding, Enhancing the macroscopic polarization of CdS for piezo-photocatalytic water splitting, *Nano Energy* 90 (2021), 106635.
- [29] M. Wang, B. Wang, F. Huang, Z. Lin, Enabling PIEZOpotential in PIEZOelectric semiconductors for enhanced catalytic activities, *Angew. Chem. Int. Ed.* 58 (2019) 7526–7536.
- [30] R. Su, H.A. Hsain, M. Wu, D. Zhang, X. Hu, Z. Wang, X. Wang, F.-t Li, X. Chen, L. Zhu, Y. Yang, Y. Yang, X. Lou, S.J. Pennycook, Nano-ferroelectric for high efficiency overall water splitting under ultrasonic vibration, *Angew. Chem. Int. Ed.* 58 (2019) 15076–15081.
- [31] E. Lin, J. Wu, N. Qin, B. Yuan, Z. Kang, D. Bao, Enhanced piezocatalytic, photocatalytic and piezo-/photocatalytic performance of diphasic Ba<sub>1-x</sub>CaxTiO<sub>3</sub> nanowires near a solubility limit, *Catal. Sci. Technol.* 9 (2019) 6863–6874.
- [32] E. Lin, J. Wu, N. Qin, B. Yuan, D. Bao, Silver modified barium titanate as a highly efficient piezocatalyst, *Catal. Sci. Technol.* 8 (2018) 4788–4796.
- [33] P. Wang, X. Li, S. Fan, X. Chen, M. Qin, D. Long, M.O. Tadé, S. Liu, Impact of oxygen vacancy occupancy on piezo-catalytic activity of BaTiO<sub>3</sub> nanobelts, *Appl. Catal. B Environ.* 279 (2020), 119340.
- [34] H. Li, Y. Sang, S. Chang, X. Huang, Y. Zhang, R. Yang, H. Jiang, H. Liu, Z.L. Wang, Enhanced ferroelectric-nanocrystal-based hybrid photocatalysis by ultrasonic-wave-generated piezophototronic effect, *Nano Lett.* 15 (2015) 2372–2379.
- [35] F. Mushtaq, X.Z. Chen, M. Hoop, H. Torlakcik, E. Pellicer, J. Sort, C. Gattinoni, B. J. Nelson, S. Panie, Piezoelectrically enhanced photocatalysis with BiFeO<sub>3</sub> nanostructures for efficient water remediation, *ISCIENCE* 4 (2018) 236.
- [36] S. Li, Z. Zhao, J. Zhao, Z. Zhang, X. Li, J. Zhang, Recent advances of ferro-, piezo-, and pyroelectric nanomaterials for catalytic applications, *ACS Appl. Nano Mater.* 3 (2020) 1063–1079.
- [37] Z. Hu, Z. Wu, C. Han, J. He, Z. Ni, W. Chen, Two-dimensional transition metal dichalcogenides: interface and defect engineering, *Chem. Soc. Rev.* 47 (2018) 3100–3128.
- [38] J. Shi, P. Yu, F. Liu, P. He, R. Wang, L. Qin, J. Zhou, X. Li, J. Zhou, X. Sui, S. Zhang, Y. Zhang, Q. Zhang, T.C. Sun, X. Qiu, Z. Liu, X. Liu, 3R MoS<sub>2</sub> with broken inversion symmetry: a promising ultrathin nonlinear optical device, *Adv. Mater.* 29 (2017), 1701486.
- [39] T. Cao, G. Wang, W. Han, H. Ye, C. Zhu, J. Shi, Q. Niu, P. Tan, E. Wang, B. Liu, J. Feng, Valley-selective circular dichroism of monolayer molybdenum disulphide, *Nat. Commun.* 3 (2012) 887.
- [40] E.S. Kadantsev, P. Hawrylak, Electronic structure of a single MoS<sub>2</sub> monolayer, *Solid State Commun.* 152 (2012) 909–913.
- [41] S. Bertolazzi, J. Brivio, A. Kis, Stretching and breaking of ultrathin MoS<sub>2</sub>, *ACS Nano* 5 (2011) 9703–9709.
- [42] L. Britnell, R.M. Ribeiro, A. Eckmann, R. Jalil, B.D. Belle, A. Mishchenko, Y. Kim, R.V. Gorbatchev, T. Georgiou, S.V. Morozov, A.N. Grigorenko, A.K. Geim, C. Casiraghi, A.H.C. Neto, K.S. Novoselov, Strong light-matter interactions in heterostructures of atomically thin films, *Science* 340 (2013) 1311–1314.
- [43] O. Lopez-Sanchez, D. Lemke, M. Kayci, A. Radenovic, A. Kis, Ultrasensitive photodetectors based on monolayer MoS<sub>2</sub>, *Nat. Nanotechnol.* 8 (2013) 497–501.
- [44] B. Radisavljevic, A. Radenovic, J. Brivio, V. Giacometti, A. Kis, Single-layer MoS<sub>2</sub> transistors, *Nat. Nanotechnol.* 6 (2011) 147–150.
- [45] K.F. Mak, C. Lee, J. Hone, J. Shan, T.F. Heinz, Atomically thin \$\\{\\text{MoS}\_2\\}\$: a new direct-gap semiconductor, *Phys. Rev. Lett.* 105 (2010) 136805.
- [46] A. Pospischil, M.M. Furchi, T. Mueller, Solar-energy conversion and light emission in an atomic monolayer p–n diode, *Nat. Nanotechnol.* 9 (2014) 257–261.
- [47] C. Xie, C. Mak, X. Tao, F. Yan, Photodetectors based on two-dimensional layered materials beyond graphene, *Adv. Funct. Mater.* 27 (2017), 1603886.
- [48] H. Zeng, J. Dai, W. Yao, D. Xiao, X. Cui, Valley polarization in MoS<sub>2</sub> monolayers by optical pumping, *Nat. Nanotechnol.* 7 (2012) 490–493.
- [49] K.F. Mak, K. He, J. Shan, T.F. Heinz, Control of valley polarization in monolayer MoS<sub>2</sub> by optical helicity, *Nat. Nanotechnol.* 7 (2012) 494–498.
- [50] G.-H. Lee, Y.-J. Yu, X. Cui, N. Petrone, C.-H. Lee, M.S. Choi, D.-Y. Lee, C. Lee, W. J. Yoo, K. Watanabe, T. Taniguchi, C. Nuckolls, P. Kim, J. Hone, Flexible and transparent MoS<sub>2</sub> field-effect transistors on hexagonal boron nitride-graphene heterostructures, *ACS Nano* 7 (2013) 7931–7936.
- [51] K.-A.N. Duerloo, M.T. Ong, E.J. Reed, Intrinsic piezoelectricity in two-dimensional materials, *J. Phys. Chem. Lett.* 3 (2012) 2871–2876.
- [52] M.N. Blonsky, H.L. Zhuang, A.K. Singh, R.G. Hennig, Ab initio prediction of piezoelectricity in two-dimensional materials, *ACS Nano* 9 (2015) 9885–9891.
- [53] L. Dong, J. Lou, V.B. Shenoy, Large in-plane and vertical piezoelectricity in janus transition metal dichalcogenides, *ACS Nano* 11 (2017) 8242–8248.
- [54] M.K. Mohanta, A. De Sarkar, Interfacial hybridization of Janus MoSSe and BX (X = P, As) monolayers for ultrathin excitonic solar cells, nanopiezotronics and low-power memory devices, *Nanoscale* 12 (2020) 22645–22657.
- [55] R. Ahmed, N. Jena, A. Rawat, M.K. Mohanta, Dimple, A. De Sarkar, Ultrahigh out-of-plane piezoelectricity meets giant rashba effect in 2D janus monolayers and bilayers of group IV transition-metal trichalcogenides, *J. Phys. Chem. C* 124 (2020) 21250–21260.
- [56] M.M. Alyörük, Y. Aierken, D. Çakır, F.M. Peeters, C. Sevik, Promising piezoelectric performance of single layer transition-metal dichalcogenides and dioxides, *J. Phys. Chem. C* 119 (2015) 23231–23237.
- [57] R. Hinche, U. Khan, C. Falconi, S.-W. Kim, Piezoelectric properties in two-dimensional materials: Simulations and experiments, *Mater. Today* 21 (2018) 611–630.
- [58] D. Yang, X. Hu, M. Zhuang, Y. Ding, S. Zhou, A. Li, Y. Yu, H. Li, Z. Luo, L. Gan, T. Zhai, Inversion symmetry broken 2D 3R-MoTe<sub>2</sub>, *Adv. Funct. Mater.* 28 (2018), 1800785.
- [59] W. Wu, L. Wang, Y. Li, F. Zhang, L. Lin, S. Niu, D. Chenet, X. Zhang, Y. Hao, T. F. Heinz, J. Hone, Z.L. Wang, Piezoelectricity of single-atomic-layer MoS<sub>2</sub> for energy conversion and piezotronics, *Nature* 514 (2014) 470–474.
- [60] H. Zhu, Y. Wang, J. Xiao, M. Liu, S. Xiong, Z.J. Wong, Z. Ye, Y. Ye, X. Yin, X. Zhang, Observation of piezoelectricity in free-standing monolayer MoS<sub>2</sub>, *Nat. Nanotechnol.* 10 (2015) 151–155.
- [61] W. Liu, A. Zhang, Y. Zhang, Z.L. Wang, Density functional studies on edge-contacted single-layer MoS<sub>2</sub> piezotronic transistors, *Appl. Phys. Lett.* 107 (2015), 083105.
- [62] W. Wu, L. Wang, R. Yu, Y. Liu, S.-H. Wei, J. Hone, Z.L. Wang, Piezophototronic effect in single-atomic-layer MoS<sub>2</sub> for strain-gated flexible optoelectronics, *Adv. Mater.* 28 (2016) 8463–8468.
- [63] K. Zhang, M. Peng, W. Wu, J. Guo, G. Gao, Y. Liu, J. Kou, R. Wen, Y. Lei, A. Yu, Y. Zhang, J. Zhai, Z.L. Wang, A flexible p-CuO/n-MoS<sub>2</sub> heterojunction photodetector with enhanced photoresponse by the piezo-phototronic effect, *Mater. Horiz.* 4 (2017) 274–280.
- [64] M.-H. Wu, J.-T. Lee, Y.J. Chung, M. Srinivas, J.-M. Wu, Ultrahigh efficient degradation activity of single- and few-layered MoSe<sub>2</sub> nanoflowers in dark by piezo-catalyst effect, *Nano Energy* 40 (2017) 369–375.
- [65] J.M. Wu, Y.-G. Sun, W.-E. Chang, J.-T. Lee, Piezoelectricity induced water splitting and formation of hydroxyl radical from active edge sites of MoS<sub>2</sub> nanoflowers, *Nano Energy* 46 (2018) 372–382.
- [66] S. Li, Z. Zhao, D. Yu, J.-Z. Zhao, Y. Su, Y. Liu, Y. Lin, W. Liu, H. Xu, Z. Zhang, Few-layer transition metal dichalcogenides (MoS<sub>2</sub>, WS<sub>2</sub>, and WSe<sub>2</sub>) for water splitting and degradation of organic pollutants: Understanding the piezocatalytic effect, *Nano Energy* 66 (2019), 104083.
- [67] Y.-J. Chung, C.-S. Yang, J.-T. Lee, G.H. Wu, J.M. Wu, Coupling effect of piezo-flexocatalytic hydrogen evolution with hybrid 1T- and 2H-phase few-layered MoSe<sub>2</sub> nanosheets, *Adv. Energy Mater.* 10 (2020), 2002082.
- [68] T. Dan, M. Willatzen, Z.L. Wang, Prediction of strong piezoelectricity in 3R-MoS<sub>2</sub> multilayer structures, *Nano Energy* 56 (2019) 512–515.
- [69] T. Ren, W. Tian, Q. Shen, Z. Yuan, D. Chen, N. Li, J. Lu, Enhanced piezocatalysis of polymorphic few-layered MoS<sub>2</sub> nanosheets by phase engineering, *Nano Energy* 90 (2021), 106527.
- [70] J. Hong, C. Jin, J. Yuan, Z. Zhang, Atomic defects in two-dimensional materials: from single-atom spectroscopy to functionalities in opto-/electronics, *Nanomagnet. Catal. Adv. Mater.* 29 (2017), 1606434.
- [71] J. Kibsgaard, Z. Chen, B.N. Reinecke, T.F. Jaramillo, Engineering the surface structure of MoS<sub>2</sub> to preferentially expose active edge sites for electrocatalysis, *Nat. Mater.* 11 (2012) 963–969.
- [72] X. Song, F. Hui, K. Gilmore, B. Wang, G. Jing, Z. Fan, E. Grustan-Gutierrez, Y. Shi, L. Lombardi, S.A. Hodge, A.C. Ferrari, M. Lanza, Enhanced piezoelectric effect at the edges of stepped molybdenum disulfide nanosheets, *Nanoscale* 9 (2017) 6237–6245.
- [73] W. Ma, B. Yao, W. Zhang, Y. He, Y. Yu, J. Niu, C. Wang, A novel multi-flaw MoS<sub>2</sub> nanosheet piezocatalyst with superhigh degradation efficiency for ciprofloxacin, *Environ. Sci. Nano* 5 (2018) 2876–2887.
- [74] W.T. Yein, Q. Wang, Y. Li, X. Wu, Piezoelectric potential induced the improved micro-pollutant dye degradation of Co doped MoS<sub>2</sub> ultrathin nanosheets in dark, *Catal. Commun.* 125 (2019) 61–65.
- [75] M.R. Esmaeil-Rad, S. Salahuddin, High performance molybdenum disulfide amorphous silicon heterojunction photodetector, *Sci. Rep.* 3 (2013) 2345.
- [76] J. Wu, H. Li, Z. Yin, H. Li, J. Liu, X. Cao, Q. Zhang, H. Zhang, Layer thinning and etching of mechanically exfoliated MoS<sub>2</sub> nanosheets by thermal annealing in air, *Small* 9 (2013) 3314–3319.
- [77] S.K. Kim, R. Bhatia, T.-H. Kim, D. Seol, J.H. Kim, H. Kim, W. Seung, Y. Kim, Y. H. Lee, S.-W. Kim, Directional dependent piezoelectric effect in CVD grown monolayer MoS<sub>2</sub> for flexible piezoelectric nanogenerators, *Nano Energy* 22 (2016) 483–489.
- [78] J. Chen, X. Zhao, G. Grinblat, Z. Chen, S.J.R. Tan, W. Fu, Z. Ding, I. Abdelwahab, Y. Li, D. Geng, Y. Liu, K. Leng, B. Liu, W. Liu, W. Tang, S.A. Maier, S.J. Pennycook, K.P. Loh, Homoepitaxial growth of large-scale highly organized transition metal dichalcogenide patterns, *Adv. Mater.* 30 (2018), 1704674.
- [79] R. Lei, F. Gao, J. Yuan, C. Jiang, X. Fu, W. Feng, P. Liu, Free layer-dependent piezoelectricity of oxygen-doped MoS<sub>2</sub> for the enhanced piezocatalytic hydrogen evolution from pure water, *Appl. Surf. Sci.* 576 (2022), 151851.
- [80] S. Xu, L. Guo, Q. Sun, Z.L. Wang, Piezotronic effect enhanced plasmonic photocatalysis by AuNPs/BaTiO<sub>3</sub> heterostructures, *Adv. Funct. Mater.* 29 (2019), 1808737.
- [81] T.-M. Chou, S.-W. Chan, Y.-J. Lin, P.-K. Yang, C.-C. Liu, Y.-J. Lin, J.-M. Wu, J.-T. Lee, Z.-H. Lin, A highly efficient Au-MoS<sub>2</sub> nanocatalyst for tunable piezocatalytic and photocatalytic water disinfection, *Nano Energy* 57 (2019) 14–21.

- [82] X. Zhao, Y. Lei, P. Fang, H. Li, Q. Han, W. Hu, C. He, Piezotronic effect of single-/few-layers MoS<sub>2</sub> nanosheets composite with TiO<sub>2</sub> nanorod heterojunction, *Nano Energy* 66 (2019), 104168.
- [83] M. Pan, S. Liu, J.W. Chew, Unlocking the high redox activity of MoS<sub>2</sub> on dual-doped graphene as a superior piezocatalyst, *Nano Energy* 68 (2020), 104366.
- [84] Y. Chen, S. Lan, M. Zhu, Construction of piezoelectric BaTiO<sub>3</sub>/MoS<sub>2</sub> heterojunction for boosting piezo-activation of peroxymonosulfate, *Chin. Chem. Lett.* 32 (2021) 2052–2056.
- [85] H. Li, Y. Xiong, Y. Wang, W. Ma, J. Fang, X. Li, Q. Han, Y. Liu, C. He, P. Fang, High piezocatalytic capability in CuS/MoS<sub>2</sub> nanocomposites using mechanical energy for degrading pollutants, *J. Colloid Interface Sci.* 609 (2022) 657–666.
- [86] H.Y. Zhang, J.D. Dai, C.M. Liu, The fabrication, microstructure, photo-catalysis and piezo-catalysis of layered TiO<sub>2</sub>-MoS<sub>2</sub>, *Mater. Res. Express* 6 (2018), 025025.
- [87] B. Huo, F. Meng, J. Yang, Y. Wang, J. Qi, W. Ma, Z. Wang, J. Wang, Z. Wang, High efficiently piezocatalysis degradation of tetracycline by few-layered MoS<sub>2</sub>/GDY: Mechanism and toxicity evaluation, *Chem. Eng. J.* 436 (2022), 135173.
- [88] M. Ran, H. Xu, Y. Bao, Y. Zhang, J. Zhang, M. Xing, Selective production of CO from organic pollutants by coupling piezocatalysis and advanced oxidation processes, *Angew. Chem. Int. Ed.* 62 (2023), e202303728.
- [89] C. Yang, P. Wang, J. Li, Q. Wang, P. Xu, S. You, Q. Zheng, G. Zhang, Photocatalytic PVDF ultrafiltration membrane blended with visible-light responsive Fe(III)-TiO<sub>2</sub> catalyst: Degradation kinetics, catalytic performance and reusability, *Chem. Eng. J.* 417 (2021), 129340.
- [90] S. Masimukku, Y.-C. Hu, Z.-H. Lin, S.-W. Chan, T.-M. Chou, J.M. Wu, High efficient degradation of dye molecules by PDMS embedded abundant single-layer tungsten disulfide and their antibacterial performance, *Nano Energy* 46 (2018) 338–346.
- [91] B. Dai, H. Huang, W. Wang, Y. Chen, C. Lu, J. Kou, L. Wang, F. Wang, Z. Xu, Greatly enhanced photocatalytic activity by organic flexible piezoelectric PVDF induced spatial electric field, *Catal. Sci. Technol.* 7 (2017) 5594–5601.
- [92] W. Ma, B. Yao, W. Zhang, Y. He, Y. Yu, J. Niu, Fabrication of PVDF-based piezocatalytic active membrane with enhanced oxytetracycline degradation efficiency through embedding few-layer E-MoS<sub>2</sub> nanosheets, *Chem. Eng. J.* 415 (2021), 129000.
- [93] S. Verma, M. Sharma, R. Vaish, Photo-piezocatalysis in electrospun PVDF + WS<sub>2</sub> membrane, *Environ. Sci.: Nano* 9 (2022) 3885–3899.
- [94] J. Shi, S. Yang, Z. Zheng, J. Li, L. Wang, W. Zeng, L. Yang, Y. Xiong, Z. Jin, X. Tao, Texture-based piezocatalytic platform for organics degradation under low-frequency water flow, *J. Mater. Chem. A* 11 (2023) 7596–7604.
- [95] W. Tian, J. Qiu, N. Li, D. Chen, Q. Xu, H. Li, J. He, J. Lu, Efficient piezocatalytic removal of BPA and Cr(VI) with SnS<sub>2</sub>/CNFs membrane by harvesting vibration energy, *Nano Energy* 86 (2021), 106036.
- [96] V. Teodoro, A. Barrios Trench, L. Guerreiro da Trindade, N. Jacomaci, H. Beltran-Mir, J. Andrés, E. Cordoncillo, J. Bettini, E. Longo, Behavior of Bi<sub>2</sub>S<sub>3</sub> under ultrasound irradiation for Rhodamine B dye degradation, *Chem. Phys. Lett.* 785 (2021), 139123.
- [97] F. Gao, M. Fang, S. Zhang, M. Ni, Y. Cai, Y. Zhang, X. Tan, M. Kong, W. Xu, X. Wang, Symmetry-breaking induced piezocatalysis of Bi<sub>2</sub>S<sub>3</sub> nanorods and boosted by alternating magnetic field, *Appl. Catal. B Environ.* 316 (2022), 121664.
- [98] S. Li, Z. Zhao, J. Li, H. Liu, M. Liu, Y. Zhang, L. Su, A.I. Pérez-Jiménez, Y. Guo, F. Yang, Y. Liu, J. Zhao, J. Zhang, L.-D. Zhao, Y. Lin, Mechanically induced highly efficient hydrogen evolution from water over piezoelectric SnSe nanosheets, *Small* 18 (2022), 2202507.
- [99] X. He, C. Chen, Y. Gong, H. Zeng, Z. Yi, Bi<sub>2</sub>WO<sub>6</sub> lead-free ferroelectrics: microstructure design, polar behavior and photovoltaic performance, *J. Mater. Chem. C* 9 (2021) 7539–7544.
- [100] M. Fukunaga, M. Takesada, A. Onodera, Ferroelectricity in layered perovskites as a model of ultra-thin films, *World J. Condens. Matter Phys.* 6 (2016) 224–243.
- [101] C.A.P. de Araujo, J.D. Cuchiaro, L.D. McMillan, M.C. Scott, J.F. Scott, Fatigue-free ferroelectric capacitors with platinum electrodes, *Nature* 374 (1995) 627–629.
- [102] J. Yu, J. Xiong, B. Cheng, Y. Yu, J. Wang, Hydrothermal preparation and visible-light photocatalytic activity of Bi<sub>2</sub>WO<sub>6</sub> powders, *J. Solid State Chem.* 178 (2005) 1968–1972.
- [103] H. Djani, P. Hermet, P. Ghosez, First-principles characterization of the P21ab ferroelectric phase of aurivillius Bi<sub>2</sub>WO<sub>6</sub>, *J. Phys. Chem. C* 118 (2014) 13514–13524.
- [104] H. Takeda, J.S. Han, M. Nishida, T. Shiosaki, T. Hoshina, T. Tsurumi, Growth and piezoelectric properties of ferroelectric Bi<sub>2</sub>WO<sub>6</sub> mono-domain crystals, *Solid State Commun.* 150 (2010) 836–839.
- [105] A. Moure, A. Castro, L. Pardo, Aurivillius-type ceramics, a class of high temperature piezoelectric materials: Drawbacks, advantages and trends, *Prog. Solid State Chem.* 37 (2009) 15–39.
- [106] A. Hao, X. Ning, Y. Cao, J. Xie, D. Jia, Boosting the piezocatalytic performance of Bi<sub>2</sub>WO<sub>6</sub> nanosheets towards the degradation of organic pollutants, *Mater. Chem. Front.* 4 (2020) 2096–2102.
- [107] A. Kudo, S. Hijii, H<sub>2</sub> or O<sub>2</sub> evolution from aqueous solutions on layered oxide photocatalysts consisting of Bi<sup>3+</sup> with 6s<sup>2</sup> configuration and d<sup>0</sup> transition metal ions, *Chem. Lett.* 28 (1999) 1103–1104.
- [108] H. Fu, C. Pan, W. Yao, Y. Zhu, Visible-light-induced degradation of rhodamine B by nanosized Bi<sub>2</sub>WO<sub>6</sub>, *J. Phys. Chem. B* 109 (2005) 22432–22439.
- [109] J. Tang, Z. Zou, J. Ye, Photocatalytic decomposition of organic contaminants by Bi<sub>2</sub>WO<sub>6</sub> under visible light irradiation, *Catal. Lett.* 92 (2004) 53–56.
- [110] H. Fu, L. Zhang, W. Yao, Y. Zhu, Photocatalytic properties of nanosized Bi<sub>2</sub>WO<sub>6</sub> catalysts synthesized via a hydrothermal process, *Appl. Catal. B Environ.* 66 (2006) 100–110.
- [111] L. Zhang, W. Wang, L. Zhou, H. Xu, Bi<sub>2</sub>WO<sub>6</sub> nano- and microstructures: shape control and associated visible-light-driven photocatalytic activities, *Small* 3 (2007) 1618–1625.
- [112] Z. Kang, N. Qin, E. Lin, J. Wu, B. Yuan, D. Bao, Effect of Bi<sub>2</sub>WO<sub>6</sub> nanosheets on the ultrasonic degradation of organic dyes: Roles of adsorption and piezocatalysis, *J. Clean. Prod.* 261 (2020), 121125.
- [113] Z. Kang, E. Lin, N. Qin, J. Wu, B. Yuan, D. Bao, Effect of oxygen vacancies and crystal symmetry on piezocatalytic properties of Bi<sub>2</sub>WO<sub>6</sub> ferroelectric nanosheets for wastewater decontamination, *Environ. Sci.: Nano* 8 (2021) 1376–1388.
- [114] H. Lei, M. Wu, Y. Liu, F. Mo, J. Chen, S. Ji, Y. Zou, X. Dong, Built-in piezoelectric field improved photocatalytic performance of nanoflower-like Bi<sub>2</sub>WO<sub>6</sub> using lower-power white LEDs, *Chin. Chem. Lett.* 32 (2021) 2317–2321.
- [115] K. Hu, R. Wang, M. Maimaititursun, H. Sun, X. Liu, Y. Zhang, Synergetic piezophotocatalytic effect in ultrathin Bi<sub>2</sub>WO<sub>6</sub> nanosheets for decomposing organic dye, *J. Mater. Sci. Mater. Electron.* 33 (2022) 9845–9857.
- [116] W. Shen, N. Li, S. Zuo, M. Wu, G. Sun, Q. Li, M. Shi, J. Ma, Remarkably enhanced piezo-photocatalytic performance of Z-scheme Bi<sub>2</sub>WO<sub>6</sub>/Black TiO<sub>2</sub> heterojunction via piezoelectric effect, *Ceram. Int.* 48 (2022) 15899–15907.
- [117] Y. Li, G. Chen, H. Zhang, Z. Li, J. Sun, Electronic structure and photocatalytic properties of Abi<sub>2</sub>Ta<sub>2</sub>O<sub>9</sub> (A=Ca, Sr, Ba), *J. Solid State Chem.* 181 (2008) 2653–2659.
- [118] Y. Li, G. Chen, H. Zhang, Z. Lv, Band structure and photocatalytic activities for H<sub>2</sub> production of Abi<sub>2</sub>Nb<sub>2</sub>O<sub>9</sub> (A=Ca, Sr, Ba), *Int. J. Hydrog. Energy* 35 (2010) 2652–2656.
- [119] W. Wu, S. Liang, X. Wang, J. Bi, P. Liu, L. Wu, Synthesis, structures and photocatalytic activities of microcrystalline Abi<sub>2</sub>Nb<sub>2</sub>O<sub>9</sub> (A=Sr, Ba) powders, *J. Solid State Chem.* 184 (2011) 81–88.
- [120] V. Senthil, S. Panigrahi, Dielectric, ferroelectric, impedance and photocatalytic water splitting study of Y<sub>3</sub> modified SrBi<sub>2</sub>Ta<sub>2</sub>O<sub>9</sub> ferroelectrics, *Int. J. Hydrog. Energy* 44 (2019) 18058–18071.
- [121] S. Tu, H. Huang, T. Zhang, Y. Zhang, Controllable synthesis of multi-responsive ferroelectric layered perovskite-like Bi<sub>4</sub>Ti<sub>3</sub>O<sub>12</sub>: Photocatalysis and piezoelectric-catalysis and mechanism insight, *Appl. Catal. B Environ.* 219 (2017) 550–562.
- [122] J. Wu, N. Qin, E. Lin, B. Yuan, Z. Kang, D. Bao, Synthesis of Bi<sub>4</sub>Ti<sub>3</sub>O<sub>12</sub> doped nanoplates with enhanced piezocatalytic activity, *Nanoscale* 11 (2019) 21128–21136.
- [123] D. Liu, C. Jin, Y. Zhang, Y. He, F. Wang, Integrated piezo-photocatalysis of electrospun Bi<sub>4</sub>Ti<sub>3</sub>O<sub>12</sub> nanostructures by bi-harvesting visible light and ultrasonic energies, *Ceram. Int.* 47 (2021) 7692–7699.
- [124] Z. Xie, X. Tang, J. Shi, Y. Wang, G. Yuan, J.-M. Liu, Excellent piezo-photocatalytic performance of Bi<sub>4</sub>Ti<sub>3</sub>O<sub>12</sub> nanoplates synthesized by molten-salt method, *Nano Energy* 98 (2022), 107247.
- [125] N. Tian, C. Hu, J. Wang, Y. Zhang, T. Ma, H. Huang, Layered bismuth-based photocatalysts, *Coord. Chem. Rev.* 463 (2022), 214515.
- [126] J. Li, Y. Yu, L. Zhang, Bismuth oxyhalide nanomaterials: layered structures meet photocatalysis, *Nanoscale* 6 (2014) 8473–8488.
- [127] L. Ye, Y. Su, X. Jin, H. Xie, C. Zhang, Recent advances in BiOX (X = Cl, Br and I) photocatalysts: synthesis, modification, facet effects and mechanisms, *Environ. Sci. Nano* 1 (2014) 90–112.
- [128] J. Jiang, K. Zhao, X. Xiao, L. Zhang, Synthesis and facet-dependent photoreactivity of BiOCl single-crystalline nanosheets, *J. Am. Chem. Soc.* 134 (2012) 4473–4476.
- [129] L. Zhang, W. Wang, S. Sun, D. Jiang, E. Gao, Selective transport of electron and hole among {001} and {110} facets of BiOCl for pure water splitting, *Appl. Catal. B Environ.* 162 (2015) 470–474.
- [130] D. Shao, L. Zhang, S. Sun, W. Wang, Oxygen reduction reaction for generating H<sub>2</sub>O<sub>2</sub> through a piezo-catalytic process over bismuth oxychloride, *ChemSusChem* 11 (2018) 527–531.
- [131] M. Ismail, Z. Wu, L. Zhang, J. Ma, Y. Jia, Y. Hu, Y. Wang, High-efficient synergy of piezocatalysis and photocatalysis in bismuth oxychloride nanomaterial for dye decomposition, *Chemosphere* 228 (2019) 212–218.
- [132] H. Lei, H. Zhang, Y. Zou, X. Dong, Y. Jia, F. Wang, Synergetic photocatalysis/piezocatalysis of bismuth oxybromide for degradation of organic pollutants, *J. Alloy. Compd.* 809 (2019), 151840.
- [133] L. Li, W. Cao, J. Yao, W. Liu, F. Li, C. Wang, Synergistic piezo-photocatalysis of BiOCl/NaNbO<sub>3</sub> heterojunction piezoelectric composite for high-efficient organic pollutant degradation, *Nanomaterials* 12 (2022).
- [134] Z. Yao, H. Sun, S. Xiao, Y. Hu, X. Liu, Y. Zhang, Synergetic piezo-photocatalytic effect in a Bi<sub>2</sub>MoO<sub>6</sub>/BiOBr composite for decomposing organic pollutants, *Appl. Surf. Sci.* 560 (2021), 150037.
- [135] J. Li, L. Zhang, Y. Li, Y. Yu, Synthesis and internal electric field dependent photoreactivity of Bi<sub>3</sub>O<sub>4</sub>Cl single-crystalline nanosheets with high {001} facet exposure percentages, *Nanoscale* 6 (2014) 167–171.
- [136] J. Li, L. Cai, J. Shang, Y. Yu, L. Zhang, Giant enhancement of internal electric field boosting bulk charge separation for photocatalysis, *Adv. Mater.* 28 (2016) 4059–4064.
- [137] Q. Zhou, J. Jiang, Bi<sub>3</sub>O<sub>4</sub>Br nanoplates as an efficient piezo-photocatalyst for organic dye degradation, *Mod. Phys. Lett. B* 35 (2021), 2150119.
- [138] Y. Wang, D. Yu, Y. Liu, X. Liu, Y. Shi, Boosting piezo/photo-induced charge transfer of CNT/Bi4O5I2 catalyst for efficient ultrasound-assisted degradation of rhodamine B, *Materials* 14 (2021).
- [139] S.D. Nguyen, J. Yeon, S.-H. Kim, P.S. Halasayamani, BiO(IO<sub>3</sub>): a new polar iodate that exhibits an aurivillius-type (Bi<sub>2</sub>O<sub>2</sub>)<sub>2</sub>+ layer and a large SHG response, *J. Am. Chem. Soc.* 133 (2011) 12422–12425.
- [140] W. Wang, B. Huang, X. Ma, Z. Wang, X. Qin, X. Zhang, Y. Dai, M.-H. Whangbo, Efficient separation of photogenerated electron-hole pairs by the combination of a

- heterolayered structure and internal polar field in pyroelectric BiOIO<sub>3</sub> nanoplates, *Chem. A Eur. J.* 19 (2013) 14777–14780.
- [141] Y. Su, L. Zhang, W. Wang, Internal polar field enhanced H<sub>2</sub> evolution of BiOIO<sub>3</sub> nanoplates, *Int. J. Hydrog. Energy* 41 (2016) 10170–10177.
- [142] W. Wang, H. Cheng, B. Huang, X. Liu, X. Qin, X. Zhang, Y. Dai, Hydrothermal synthesis of C<sub>3</sub>N<sub>4</sub>/BiOIO<sub>3</sub> heterostructures with enhanced photocatalytic properties, *J. Colloid Interface Sci.* 442 (2015) 97–102.
- [143] R. Zhang, Y. Dai, Z. Lou, Z. Li, Z. Wang, Y. Yang, X. Qin, X. Zhang, B. Huang, Layered photocatalyst Bi<sub>2</sub>O<sub>2</sub>[BO<sub>2</sub>(OH)] nanosheets with internal polar field enhanced photocatalytic activity, *CrystEngComm* 16 (2014) 4931–4934.
- [144] C. Hu, H. Huang, F. Chen, Y. Zhang, H. Yu, T. Ma, Coupling piezocatalysis and photocatalysis in Bi<sub>4</sub>NbO<sub>8</sub>X (X = Cl, Br) polar single crystals, *Adv. Funct. Mater.* 30 (2020), 1908168.
- [145] Z.L. Wang, Progress in piezotronics and piezo-photronics, *Adv. Mater.* 24 (2012) 4632–4646.
- [146] Z. Liang, C.-F. Yan, S. Rtimi, J. Bandara, Piezoelectric materials for catalytic/photocatalytic removal of pollutants: Recent advances and outlook, *Appl. Catal. B Environ.* 241 (2019) 256–269.
- [147] X. Xue, W. Zang, P. Deng, Q. Wang, L. Xing, Y. Zhang, Z.L. Wang, Piezo-potential enhanced photocatalytic degradation of organic dye using ZnO nanowires, *Nano Energy* 13 (2015) 414–422.
- [148] W. Wu, X. Yin, B. Dai, J. Kou, Y. Ni, C. Lu, Water flow driven piezo-photocatalytic flexible films: Bi-piezoelectric integration of ZnO nanorods and PVDF, *Appl. Surf. Sci.* 517 (2020), 146119.
- [149] A. Sultana, M.M. Alam, S. Garain, T.K. Sinha, T.R. Middya, D. Mandal, An effective electrical throughput from PANI supplement ZnS nanorods and PDMS-based flexible piezoelectric nanogenerator for power up portable electronic devices: an alternative of MWCNT filler, *ACS Appl. Mater. Interfaces* 7 (2015) 19091–19097.
- [150] Y.-F. Lin, J. Song, Y. Ding, S.-Y. Lu, Z.L. Wang, Alternating the output of a CdS nanowire nanogenerator by a white-light-stimulated optoelectronic effect, *Adv. Mater.* 20 (2008) 3127–3130.
- [151] X. Wang, X. He, H. Zhu, L. Sun, W. Fu, X. Wang, L.C. Hoong, H. Wang, Q. Zeng, W. Zhao, J. Wei, Z. Jin, Z. Shen, J. Liu, T. Zhang, Z. Liu, Subatomic deformation driven by vertical piezoelectricity from CdS ultrathin films, *Science Advances*, 2 e1600209.
- [152] M. Pan, S. Liu, B. Pan, J.W. Chew, Directionally tailoring the macroscopic polarization of piezocatalysis for hollow zinc sulfide on dual-doped graphene, *Nano Energy* 88 (2021), 106312.
- [153] C. Hu, H.-Y. Sun, X.-M. Jia, H.-L. Lin, J. Cao, S.-F. Chen, Piezoelectric polarization and empty conduction band of zinc sulfide: structure modulation on graphitic carbon nitride for carbon dioxide reduction to methane, *ChemPhotoChem* 6 (2022), e202200150.
- [154] S. Lin, Q. Wang, H. Huang, Y. Zhang, Piezocatalytic and photocatalytic hydrogen peroxide evolution of sulfide solid solution nano-branches from pure water and air, *Small* 18 (2022), 2200914.
- [155] J. Long, T. Ren, J. Han, N. Li, D. Chen, Q. Xu, H. Li, J. Lu, Heterostructured BiFeO<sub>3</sub>@CdS nanofibers with enhanced piezoelectric response for efficient piezocatalytic degradation of organic pollutants, *Sep. Purif. Technol.* 290 (2022), 120861.
- [156] P. Hao, Y. Cao, X. Ning, R. Chen, J. Xie, J. Hu, Z. Lu, A. Hao, Rational design of CdS/BiOCl S-scheme heterojunction for effective boosting piezocatalytic H<sub>2</sub> evolution and pollutants degradation performances, *J. Colloid Interface Sci.* 639 (2023) 343–354.
- [157] R. Xiong, Y. Song, K. Li, Y. Xiao, B. Cheng, S. Lei, A novel 1D/2D core/shell CdS@SnS<sub>2</sub> heterostructure for efficient piezocatalytic hydrogen evolution and pollutant degradation, *J. Mater. Chem. A* 11 (2023) 18398–18408.
- [158] Q. Zhao, Y. Zou, Z. Liu, The spontaneous polarization in CdS to enhance the piezo-PEC performance via phase transition stress engineering, *J. Catal.* 416 (2022) 398–409.
- [159] Q. Zhao, Z. Liu, Z. Guo, M. Ruan, W. Yan, The collaborative mechanism of surface S-vacancies and piezoelectric polarization for boosting CdS photoelectrochemical performance, *Chem. Eng. J.* 433 (2022), 133226.
- [160] Y. Zhao, Z.-B. Fang, W. Feng, K. Wang, X. Huang, P. Liu, Hydrogen Production from pure water via piezoelectric-assisted visible-light photocatalysis of CdS nanorod arrays, *ChemCatChem* 10 (2018) 3397–3401.
- [161] Y. Zhao, X. Huang, F. Gao, L. Zhang, Q. Tian, Z.-B. Fang, P. Liu, Study on water splitting characteristics of CdS nanosheets driven by the coupling effect between photocatalysis and piezoelectricity, *Nanoscale* 11 (2019) 9085–9090.
- [162] H.A. Abbood, A. Alabadi, A.B. Al-Hawash, A.A. Abbood, K. Huang, Square CdS micro/nanosheets as efficient photo/piezobio-catalyst for hydrogen production, *Catal. Lett.* 150 (2020) 3059–3070.
- [163] J. Wang, C. Hu, Y. Zhang, H. Huang, Engineering piezoelectricity and strain sensitivity in CdS to promote piezocatalytic hydrogen evolution, *Chin. J. Catal.* 43 (2022) 1277–1285.
- [164] M.T. Ong, E.J. Reed, Engineered piezoelectricity in graphene, *ACS Nano* 6 (2012) 1387–1394.
- [165] M.T. Ong, K.-A.N. Duerloo, E.J. Reed, The effect of hydrogen and fluorine coadsorption on the piezoelectric properties of graphene, *J. Phys. Chem. C* 117 (2013) 3615–3620.
- [166] G. da Cunha Rodrigues, P. Zelenovskiy, K. Romanyuk, S. Luchkin, Y. Kopelevich, A. Kholkin, Strong piezoelectricity in single-layer graphene deposited on SiO<sub>2</sub> grating substrates, *Nat. Commun.* 6 (2015) 7572.
- [167] W. Feng, J. Yuan, F. Gao, B. Meng, W. Hu, Y. Lei, X. Huang, L. Yang, J. Shen, D. Xu, X. Zhang, P. Liu, S. Zhang, Piezopotential-driven simulated electrocatalytic nanosystem of ultrasmall MoC quantum dots encapsulated in ultrathin N-doped graphene vesicles for superhigh H<sub>2</sub> production from pure water, *Nano Energy* 75 (2020), 104990.
- [168] P. Hu, Y. Xu, Y. Lei, J. Yuan, R. Lei, R. Hu, J. Chen, D. Xu, S. Zhang, P. Liu, X. Zhang, X. Qiu, W. Feng, Piezoelectric nanofoams with the interlaced ultrathin graphene confining Zn–N–C dipoles for efficient piezocatalytic H<sub>2</sub> evolution under low-frequency vibration, *J. Energy Chem.* 69 (2022) 115–122.
- [169] M. Zelisko, Y. Hanlumyung, S. Yang, Y. Liu, C. Lei, J. Li, P.M. Ajayan, P. Sharma, Anomalous piezoelectricity in two-dimensional graphene nitride nanosheets, *Nat. Commun.* 5 (2014) 4284.
- [170] C. Hu, F. Chen, Y. Wang, N. Tian, T. Ma, Y. Zhang, H. Huang, Exceptional cocatalyst-free photo-enhanced piezocatalytic hydrogen evolution of carbon nitride nanosheets from strong in-plane polarization, *Adv. Mater.* 33 (2021), 2101751.
- [171] R. Tang, D. Gong, Y. Zhou, Y. Deng, C. Feng, S. Xiong, Y. Huang, G. Peng, L. Li, Unique g-C<sub>3</sub>N<sub>4</sub>/PDI-g-C<sub>3</sub>N<sub>4</sub> homojunction with synergistic piezo-photocatalytic effect for aquatic contaminant control and H<sub>2</sub>O<sub>2</sub> generation under visible light, *Appl. Catal. B Environ.* 303 (2022), 120929.
- [172] K. Wang, D. Shao, L. Zhang, Y. Zhou, H. Wang, W. Wang, Efficient piezo-catalytic hydrogen peroxide production from water and oxygen over graphitic carbon nitride, *J. Mater. Chem. A* 7 (2019) 20383–20389.
- [173] H. Lei, Q. He, M. Wu, Y. Xu, P. Sun, X. Dong, Piezoelectric polarization promoted spatial separation of photoexcited electrons and holes in two-dimensional g-C<sub>3</sub>N<sub>4</sub> nanosheets for efficient elimination of chlorophenols, *J. Hazard. Mater.* 421 (2022), 126696.
- [174] C. Liu, W. Ma, J. Chen, Z. Mao, D. Wang, Synergetic photocatalytic and piezocatalytic degradation of organic pollutants over graphite carbon nitride, *J. Mater. Sci. Mater. Electron.* 32 (2021) 25033–25044.
- [175] Y. Wang, Y. Guo, C. Zeng, D. Yang, Y. Zhang, L. Wu, Y. Wu, J. Hao, J. Wang, R. Yang, Realizing a strong visible-light absorption band in piezoelectric 2D carbon nitride sheets for enhanced piezocatalysis, *Nano Energy* 104 (2022), 107983.
- [176] J. Zhang, Q. Bai, X. Bi, C. Zhang, M. Shi, W.W. Yu, F. Du, L. Wang, Z. Wang, Z. Zhu, N. Sui, Piezoelectric enhanced peroxidase-like activity of metal-free sulfur doped graphdyne nanosheets for efficient water pollutant degradation and bacterial disinfection, *Nano Today* 43 (2022), 101429.
- [177] Q.-L. Zhu, Q. Xu, Metal–organic framework composites, *Chem. Soc. Rev.* 43 (2014) 5468–5512.
- [178] J. Gascon, A. Corma, F. Kapteijn, F.X. Llabrés i Xamena, Metal organic framework catalysis: Quo vadis? *ACS Catal.* 4 (2014) 361–378.
- [179] C. Wang, B. An, W. Lin, Metal–organic frameworks in solid–gas phase catalysis, *ACS Catal.* 9 (2019) 130–146.
- [180] M. Alvaro, E. Carbonell, B. Ferrer, F.X. Llabrés i Xamena, H. Garcia, Semiconductor behavior of a Metal–Organic Framework (MOF), *Chem. A Eur. J.* 13 (2007) 5106–5112.
- [181] Z. Hu, Y. Wang, D. Zhao, The chemistry and applications of hafnium and cerium (iv) metal–organic frameworks, *Chem. Soc. Rev.* 50 (2021) 4629–4683.
- [182] Y. Sun, J. Gao, Y. Cheng, Y.-W. Zhang, K. Zeng, Design of the hybrid metal–organic frameworks as potential supramolecular piezo-/ferroelectrics, *J. Phys. Chem. C* 123 (2019) 3122–3129.
- [183] C. Zhang, D. Lei, C. Xie, X. Hang, C. He, H.-L. Jiang, Piezo-photocatalysis over metal–organic frameworks: promoting photocatalytic activity by piezoelectric effect, *Adv. Mater.* 33 (2021), 2106308.
- [184] Z. Guo, N. Li, S. Zuo, C. Qiang, W. Zhan, Z. Li, J. Ma, Construction of a novel metal–organic framework adenine-Uio-66 piezocatalyst for efficient diclofenac removal, *Sep. Purif. Technol.* 289 (2022), 120743.
- [185] S. Dong, L. Wang, W. Lou, Y. Shi, Z. Cao, Y. Zhang, J. Sun, Bi-MOFs with two different morphologies promoting degradation of organic dye under simultaneous photo-irradiation and ultrasound vibration treatment, *Ultrason. Sonochem.* 91 (2022), 106223.
- [186] M. Wang, Y. Zuo, J. Wang, Y. Wang, X. Shen, B. Qiu, L. Cai, F. Zhou, S.P. Lau, Y. Chai, Remarkably enhanced hydrogen generation of organolead halide perovskites via piezocatalysis and photocatalysis, *Adv. Energy Mater.* 9 (2019), 1901801.
- [187] X. Wang, G.S. Rohrer, H. Li, Piezotronic modulations in electro- and photochemical catalysis, *MRS Bull.* 43 (2018) 946–951.
- [188] Y. Wei, Y. Zhang, W. Geng, H. Su, M. Long, Efficient bifunctional piezocatalysis of Au/BiVO<sub>4</sub> for simultaneous removal of 4-chlorophenol and Cr(VI) in water, *Appl. Catal. B Environ.* 259 (2019), 118084.
- [189] Y. Wei, Y. Zhang, J. Miao, W. Geng, M. Long, In-situ utilization of piezo-generated hydrogen peroxide for efficient p-chlorophenol degradation by Fe loading bismuth vanadate, *Appl. Surf. Sci.* 543 (2021), 148791.
- [190] G. Singh, M. Kumar, R. Vaish, Promising multicatalytic and adsorption capabilities in V2O5/BiVO<sub>4</sub> composite pellets for water-cleaning application, *Surf. Interfaces* 23 (2021), 100924.
- [191] M. Kumar, R. Vaish, S. ben Ahmed, Piezo-photocatalytic activity of mechanochemically synthesized BiVO<sub>4</sub> for dye cleaning, *J. Am. Ceram. Soc.* 105 (2022) 2309–2322.
- [192] K. Mistewicz, M. Kepińska, M. Nowak, A. Sasieła, M. Zubko, D. Stróż, Fast and efficient piezo/photocatalytic removal of methyl orange using SbSI nanowires, *Materials* (2020).
- [193] F. Liu, H. Chen, C. Xu, L. Wang, P. Qiu, S. Gao, J. Zhu, S. Zhang, Z. Guo, Monoclinic dibismuth tetraoxide (m-Bi2O4) for piezocatalysis: new use for neglected materials, *Chem. Commun.* 57 (2021) 2740–2743.
- [194] Y. Zhou, H. Wang, X. Liu, S. Qiao, D. Shao, J. Zhou, L. Zhang, W. Wang, Direct piezocatalytic conversion of methane into alcohols over hydroxyapatite, *Nano Energy* 79 (2021), 105449.

- [195] F. Wang, J. Zhang, C.-C. Jin, X. Ke, F. Wang, D. Liu, Unveiling the effect of crystal facets on piezo-photocatalytic activity of BiVO<sub>4</sub>, *Nano Energy* 101 (2022), 107573.
- [196] M. Kumar, R. Vaish, Z.M. Elqahtani, I. Kebaili, M.S. Al-Buraihi, T.H. Sung, W. Hwang, A. Kumar, Piezo-photocatalytic activity of Bi<sub>2</sub>VO<sub>5.5</sub> for methylene blue dye degradation, *J. Mater. Res. Technol.* 21 (2022) 1998–2012.
- [197] R. Wang, Y. Wang, N. Zhang, S. Lin, Y. He, Y. Yan, K. Hu, H. Sun, X. Liu, Synergetic piezo-photocatalytic effect in SbSI for highly efficient degradation of methyl orange, *Ceram. Int.* 48 (2022) 31818–31826.
- [198] Z. Chen, H. Zhou, F. Kong, M. Wang, Piezocatalytic oxidation of 5-hydroxymethylfurfural to 5-formyl-2-furancarboxylic acid over Pt decorated hydroxyapatite, *Appl. Catal. B Environ.* 309 (2022), 121281.
- [199] G. Yin, C. Fu, F. Zhang, T. Wu, S. Hao, C. Wang, Q. Song, Piezocatalytic degradation of organic dyes and production of H<sub>2</sub>O<sub>2</sub> with hydroxyapatite, *J. Alloy. Compd.* 937 (2023), 168382.
- [200] Y. Miao, W. Tian, J. Han, N. Li, D. Chen, Q. Xu, J. Lu, Oxygen vacancy-induced hydroxyl dipole reorientation in hydroxyapatite for enhanced piezocatalytic activity, *Nano Energy* 100 (2022), 107473.
- [201] S. Zhang, H. Liu, F. Gao, M. Fang, Y. Zhang, Y. Cai, K. Li, M. Kong, X. Tan, The synergistic enhancement of piezo catalytic performance to remove tetracycline by K<sub>2</sub>Ti<sub>6</sub>O<sub>13</sub>/TiO<sub>2</sub> composite, *J. Alloy. Compd.* 900 (2022), 163492.
- [202] Y. Cao, T. He, M. Li, Z. Cao, Y. Gao, J. Liu, G. Li, A novel strategy to enhance the visible light driven photocatalytic activity of CuBi<sub>2</sub>O<sub>4</sub> through its piezoelectric response, *J. Phys. Chem. Solids* 167 (2022), 110732.
- [203] X. Li, H. Zheng, J. Liu, H. Li, J. Wang, K. Yan, J. Liu, F. Dang, K. Zhu, Synthesis and piezocatalytic performance of  $\beta$ -BaTi2O5 nanorods by hydrothermal method from dried gel, *Mater. Technol.* 38 (2023), 2163474.
- [204] X. Ma, Y. Gao, B. Yang, X. Lou, J. Huang, L. Ma, D. Jing, Enhanced charge separation in La2NiO4 nanoplates by coupled piezocatalysis and photocatalysis for efficient H<sub>2</sub> evolution, *Nanoscale* 14 (2022) 7083–7095.
- [205] M. Wang, J. Liu, C. Xu, L. Feng, Sonocatalysis and sono-photocatalysis in CaCu<sub>3</sub>Ti<sub>4</sub>O<sub>12</sub> ceramics, *Ceram. Int.* 48 (2022) 11338–11345.
- [206] X. Liao, H. Xie, B. Liao, S. Hou, Y. Yu, X. Fan, Ball milling induced strong polarization electric fields in Cu<sub>3</sub>B<sub>2</sub>O<sub>6</sub> crystals for high efficiency piezocatalysis, *Nano Energy* 94 (2022), 106890.
- [207] Y. Du, T. Lu, X. Li, Y. Liu, W. Sun, S. Zhang, Z. Cheng, High-efficient piezocatalytic hydrogen evolution by centrosymmetric Bi<sub>2</sub>Fe<sub>4</sub>O<sub>9</sub> nanoplates, *Nano Energy* 104 (2022), 107919.
- [208] J. Guan, Y. Jia, T. Chang, L. Ruan, T. Xu, Z. Zhang, G. Yuan, Z. Wu, G. Zhu, Highly efficient piezo-catalysis of the heat-treated cellulose nanocrystal for dye decomposition driven by ultrasonic vibration, *Sep. Purif. Technol.* 286 (2022), 120450.
- [209] J. Hu, C. Yu, C. Li, S. Lan, L. Zeng, M. Zhu, Thickness-dependent piezo-photo-responsive behavior of ZnAl-layered double hydroxide for wastewater remediation, *Nano Energy* 101 (2022), 107583.
- [210] J. Ma, X. Xiong, D. Wu, Y. Wang, C. Ban, Y. Feng, J. Meng, X. Gao, J.-Y. Dai, G. Han, L.-Y. Gan, X. Zhou, Band position-independent piezo-electrocatalysis for ultrahigh CO<sub>2</sub> conversion, *Adv. Mater.* 35 (2023), 2300027.